CLASSIFICATION OF B-MODE ULTRASOUND KIDNEY AND LIVER IMAGES

Ph.D. THESIS

by

SUBRAMANYA M. B.

DEPARTMENT OF ELECTRICAL ENGINEERING
INDIAN INSTITUTE OF TECHNOLOGY ROORKEE
ROORKEE – 247 667 (INDIA)
JANUARY, 2016

CLASSIFICATION OF B-MODE ULTRASOUND KIDNEY AND LIVER IMAGES

A THESIS

Submitted in partial fulfilment of the Requirements for the award of the degree

of

DOCTOR OF PHILOSOPHY

in

ELECTRICAL ENGINEERING

by

SUBRAMANYA M. B.

DEPARTMENT OF ELECTRICAL ENGINEERING
INDIAN INSTITUTE OF TECHNOLOGY ROORKEE
ROORKEE – 247 667 (INDIA)
JANUARY, 2016

INDIAN INSTITUTE OF TECHNOLOGY ROORKEE
ROORKEE

CANDIDATE'S DECLARATION

I hereby certify that the work which is being presented in this thesis entitled **"CLASSIFICATION OF B-MODE ULTRASOUND KIDNEY AND LIVER IMAGES"** in partial fulfilment of the requirements for the award of the *Degree of Doctor of Philosophy* and submitted in the Department of Electrical Engineering of Indian Institute of Technology Roorkee, Roorkee is an authentic record of my own work carried out during a period from July, 2010 to January, 2016 under the supervision of Dr. Vinod Kumar, Professor, Department of Electrical Engineering, Dr. S Mukherjee, Professor (Retd.), Indian Institute of Technology Roorkee, Roorkee and Dr. Manju Saini, Associate Professor, Department of Radio diagnosis, Himalayan Institute of Medical Sciences, Dehradun.

The matter presented in this thesis has not been submitted by me for the award of any other degree of this or any other Institution.

(SUBRAMANYA M.B.)

This is to certify that the above statement made by the candidate is correct to the best of our knowledge.

(Manju Saini)	(S Mukherjee)	(Vinod Kumar)
Additional Supervisor	Supervisor	Supervisor

Date:

ACKNOWLEDGEMENTS

I would like to express my heartfelt gratitude to my supervisors Dr. Vinod Kumar, Professor, Department of Electrical Engineering, Indian Institute of Technology Roorkee and Dr. Shaktidev Mukherjee, formerly Professor in the Department of Electrical Engineering, Indian Institute of Technology Roorkee, for their guidance, patience, support to go through the course of my research work with difficulties at different levels and for their technical inputs which helped me to do satisfactory research work.

I am very much grateful to my external supervisor Dr. Manju Saini, Professor, Department of Radiology, Himalayan Institute of Hospital and Trust, for making time in her busy schedule for providing medical images and the medical perspectives for the present research work.

I would like to acknowledge my student research committee members Prof. R. S. Anand, Prof. R. P. Maheshwari, Asst. Prof. P. Sumathi, Department of Electrical Engineering and Prof. M. J. Nigam, Department of Electronics and Communication Engineering, for their valuable evaluation at each stage of PhD course.

I would like to thank the faculties of Department of Electrical Engineering, Indian Institute of Technology Roorkee for their co-operation during the course of my research work. I would like to thank Mahatma Gandhi Central Library for providing the facility to access various journals which has been significant in the present research work. I would to like thank Ministry of Human Resources and Development for providing scholarship during the research work. I owe my sincere thanks to the ethical committee of Himalayan Institute of Hospital and Trust for granting permission to utilize the medical images for research purpose.

Without the co-operation of fellow research scholars, it would have been difficult to carry out my research work. I would like to thank my seniors Dr. Jitendra Virmani, Dr. Emjee Puthooran, Dr. Jainy Sachdeva and Dr. Deepti Mittal for sharing their valuable experiences. I would also like to thank H. Nagendra, Padma Ganasala, Nishanth Jain, Ashok Kumar Dohare and M. G. Poddar for their support.

In spite of being away from home, I could stay at ease in the campus with homely environment because of the motivation of Prof. Vasantha, Emeritus Professor, Department of Electrical Engineering. My heartfelt gratitude to Nagashettappa Biradar, Guruswamy, Santhosh Desai, Chandrrasekar and their families for being part of my life in the campus.

Without the convenient and supportive lab environment, it would have not been possible to carry out my research work. I would like to thank Mr. Dinesh Sharma, Biomedical Instrumentation Laboratory, for making timely availability of facilities. I would like to thank Ameer Ahmed and all non-teaching staff of the Department of Electrical Engineering for their co-operation.

I would like to thank my childhood friend Dr. Bharath Kumar, for being the reason behind my initial motive to pursue PhD way back in 2003. In my journey from there on, I came across people time-to-time who inspired me for higher studies and research. I would like to thank D. K. Ravish, faculty, Department of Medical Electronics, Dr. Ambedkar Institute of Technology, Bangalore. I owe my sincere thanks to Dr. G. K. Prabhu, Registrar, Manipal University for guiding me to pursue MTech in Biomedical Engineering. I would like to thank Dr. Ramesh R Galigekere, Head of the Department, Biomedical Engineering, Manipal Institute of Technology who helped me in understanding research perspective and motivated me to pursue PhD.

I am very much grateful to my friends Atul Bansal and Swetanjali Gupta, who motivated me to apply for PhD in IIT Roorkee. I would like to thank Dr. Subrahmanyam Murala for his generous help at the initial stage of my research work. I would like to thank my family friends Vinay Bhardwaj and Dr. Gowri Somanath for being inspirational to me towards research.

I extend my thanks to Dr. Bindu A Thomas, Rohith M N and my other colleagues for their support which helped me in completing the PhD thesis submission.

I am very much humble and grateful to my parents M. S. Bhaskar and T. N. Lalithamba for their patience and support for all the objectives I set for myself. I would like to thank my relatives and friends for their love and encouragement.

I would like to dedicate this work to *the Guru principle* of *the unknown*, the presence and the guidance which I always felt.

Subramanya M. B.

LIST OF ABBREVIATION

AASD	Average Accuracy (Standard Deviation)
aftrs	Additive features set
AGV	Absolute Gradient Value
ANN	Artificial Neural Network
B-mode	Brightness mode
CAC	Computer-Aided Classification
CAD	Computer-Aided Diagnosis
CT	Computed Tomography
DE	Differential Evolution
DEFS	Differential Evolution Feature Selection
DPAD	Detail Preserving Anisotropic Diffusion
DROI	Diaphragm Region Of Interest
enLee	Enhanced Lee filter
FI	Filtered Image
FLD	Focal Liver Disease
FOS	First Order Statistics
Frost	Frost filter
Geo	Geometric filter
GLCM	Gray Level Co-occurrence Matrix
GRA	Gray Relational Analysis
Grad	Gradient
HIHT	Himalayan Institute of Hospital and Trust
IITR	Indian Institute of Technology Roorkee
IRB	Institutional Review Board
irftrs	Inverse Ratio features set
Kaun	Kaun filter
KNN	K-Nearest Neighbour
Lee	Lee's filter
lftrs	Liver features (features extracted from LROIs)
LROI	Liver Region Of Interest
MATLAB	Matrix Laboratory

MI	Moment Invariants
MoU	Memorandum of Understanding
MRD	Medical Renal Disease
MRI	Magnetic Resonance Imaging
NB	Naïve Bayes
OCA	Overall Classification Accuracy
OSRAD	Oriented Speckle Reducing Anisotropic Diffusion
PPNZG	Percentage of Pixels with Non-Zero Gradient
rftrs	Ratio features set
RLM	Run Length Matrix
ROI	Region Of Interest
SLee	Lee's Sigma filter
SRAD	Speckle Reducing Anisotropic Diffusion
SVM	Support Vector Machine
TEM	Texture Energy Measurement
TGC	Time Gain Compensation
TRI	Texture Rotational Invariance
US	Ultrasound

LIST OF FIGURES

LIST OF TABLES

Abstract

Imaging technology revolutionized the area of diagnosis by being complimentary to the clinical diagnosis because of its non-invasive nature. With rapid advancements in imaging modalities, the clarity and the volume of diagnostic information being obtained by radiologists have made the role of medical professionals easier and the patient comfortable. However, the subjective analysis of images takes much time of radiologists and is prone to human error depending upon their expertise and experience. To overcome these limitations, researchers have been involved in developing computer algorithms for extracting diagnostic information from the images based on clinical inputs about the diseases.

The imaging modalities such as computed tomography (CT), magnetic resonance imaging (MRI), ultrasound (US) and others have their advantages and disadvantages in general. Each modality has different perspective of information to offer about a particular disease. B-mode ultrasound imaging is preferred as an initial examination for soft tissue structures like liver, kidney, prostate, uterus etc. Its cost effective and portable nature is more suitable for extensive usage in countries like India. However, the quality of images being obtained by ultrasound is relatively of poor quality, which hinders the interpretation of images. The images obtained from echo based ultrasound imaging, basically have an interference pattern termed as speckle noise. From a radiologist's perspective, though the speckle noise is a hindrance in their subjective analysis of images, it does contain necessary diagnostic information. From a researcher's perspective, one who develop algorithms for objective diagnosis, speckle noise is an interference which is making the task difficult.

The computer-aided diagnosis (CAD) system involve majorly pre-processing followed by analysis and other applications. The present work is about the development of computer-aided classification (CAC) systems for the classification of B-mode ultrasound images. It also includes exploration of possibilities to enhance the efficiency of a CAC system. Considering the significance and frequency of cases of kidney and liver, radiologist suggested to develop CAC systems for both the databases. Thus, the present work primarily comprises of two parts: One is concerned with kidney images and the other involves liver images. In the first part, two CAC systems are proposed for kidney images:

1. a. Classification of normal, medical renal disease (MRD) and cyst classes of kidney using B-mode ultrasound images is carried out. It also includes the possible contribution by the features extracted from the de-speckled images for the classification task.

1. b. The cyst class recognition is comparatively easier among the three classes. So, to improve the classification of normal and MRD classes, a binary CAC system is proposed. To optimize the combination of texture features and the de-speckling methods for the classification, exhaustive experiments have been also carried out.

In second part, two CAC systems for the liver images are proposed:

2. a. First, classification of normal liver and grades of fatty liver (mild, moderate and severe) using B-mode ultrasound images are considered. It is also been highlighted that regions of interest (ROIs) from diaphragm have a contribution to make for the classification task.

2. b. There is an overlap of image characteristics among severe fatty liver and cirrhotic liver. So, a binary CAC system is proposed for the classification of severe fatty liver and cirrhotic liver using B-mode ultrasound images. The impact of a classifier associated with the wrapper method of feature selection on the CAC system has been also evaluated.

A generalized block diagram which can depict the outline of each of the above stated four CAC systems of the present work is shown below.

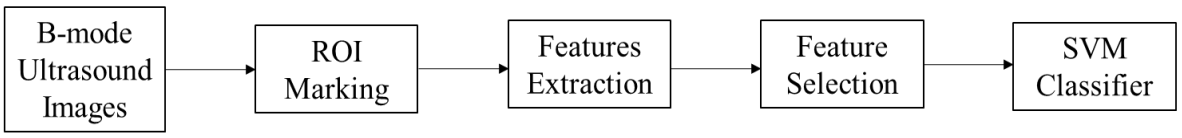

Figure 1: A brief work-flow diagram

The database used in the present work consisted of 35 kidney images comprising of 11 normal, 16 cysts and 8 MRD images and 69 liver images which includes 12 normal, 14 mild fatty liver, 14 moderate fatty liver, 13 severe fatty liver and 16 cirrhotic liver images.

The ROIs are required when sufficient number of images are not available or/and area of interest is confined to a small region. In the present work, sufficient numbers of non-overlapping ROIs of size 32 × 32 pixels are extracted from each image by the experienced radiologist.

From each ROI, various texture features are extracted to represent the ROI image in quantitative form so that it can be used to perform objective classification of ROI images. In the present work, the features used often in classification of ultrasound medical images are considered, namely, first order statistics (FOS) based features, moment invariant (MI) features, run-length matrix (RLM) features, gray-level co-occurrence matrix (GLCM) features and Laws' texture energy (Laws) features. A category of gradient (Grad) based features, which has not been used so frequently, is also considered to evaluate its potential in the present work.

In order to reduce computations in further processes and to remove redundant features without compromising on the efficiency of the CAC system, a feature selection process is considered. Differential evolution feature selection (DEFS), which is a recent wrapper method has been used in the present work. An optimization process has been carried out in prior to find out the values to be assigned to the parameters of DEFS, viz. desired number of features (texture features of ultrasound images), population size (number of ROI patterns) and number of iterations (repetitions required for the algorithm to evolve till a saturation is reached).

Support vector machine (SVM) classifier is often considered in medical applications for the better performance it brings. To perform the last stage of the CAC system i.e. classification, one-against-one multi-class SVM classifier has been considered in the present work.

To evaluate the performances, present work is carried out basically in two stages i.e. without feature selection and with feature selection. Overall classification accuracy (OCA) is considered as a performance measure in the first stage. For feature selection stage, the DEFS process is repeated 30 times to obtain 30 subsets. The subset which produced highest OCA among the 30 subsets is considered as one of the measures to evaluate the performance after feature selection. The OCAs obtained from 30 subsets are used to calculate average accuracy (standard deviation) (AASD), and is considered as another measure to show the reliability of a particular feature set for the classification task.

In the present work, the methodologies employed in different stages of CAC systems (ROI marking, extraction of features, feature selection and classification) are same for the two databases of kidney and liver. Thereby, we could draw conclusions on commonalities and distinguishing characteristics of the stages of CAC system for the two databases.

Brief description of CAC systems:

CAC System 1: The radiologist suggested that the distinguishing characteristics between normal and MRD is constrained in the region of parenchyma of kidney and cysts are local in nature. The significant point being considered is the selection of ROI for the classification of normal, MRD and cyst classes of kidney using B-mode ultrasound images. Generally, the de-speckling methods are used for providing better visualization of images for the radiologists, which in turn help them in making diagnosis easier. To overcome the limitation of subjective diagnosis, computer-aided systems are being proposed by the researchers to provide objective assistance in diagnosis. The changes in the textural information by the de-speckling methods are considered. Texture features are extracted from the de-speckled images and the feature sets are

concatenated in different combinations to enhance the potentiality of the CAC system. The concatenated RLM feature sets extracted from the ROIs of images de-speckled by Lee's sigma and enhanced Lee methods have resulted in an AASD of 86.3(1.6).

CAC System 2: Among the normal, MRD and cyst classes of kidney, distinguishing normal and MRD is more challenging, and hence in the current objective only those two classes are considered. To evaluate the performance of different texture features extracted from the images de-speckled by various methods in the classification task, six categories of texture features and eight de-speckling methods are considered. RLM features from the images de-speckled by Frost method gave an AASD of 87.0(2.9).

CAC System 3: A CAC system is proposed for the classification of normal liver and grades of fatty liver i.e. mild, moderate and severe using B-mode ultrasound images. Radiologists consider the visibility of diaphragm along with the variations in liver texture in their subjective diagnosis. For the CAC system also, ROIs are considered from both within liver and diaphragm areas to obtain higher accuracy of the system. To combine the information of these two regions, ratio features, inverse ratio features and additive features are computed. The Laws ratio features have performed better with an AASD of 84.9(3.2).

CAC system 4: In the line of grades of fatty liver, the advanced stage of severe fatty liver is cirrhotic liver. A CAC system is proposed for the classification of severe fatty liver and cirrhotic liver, wherein ROIs from the diaphragm area are not considered. In the present work, DEFS, a wrapper method is being used for the feature selection. As an another objective, two classifiers i.e. Naïve Bayes (NB) and K-nearest neighbour (KNN) classifiers are used along with DEFS algorithm to obtain different subsets of features. The concatenated set of first-order statistics and Laws feature subsets obtained from KNN-DEFS produced better AASD of 99.5(0.8).

For kidney images, the CAC system 1 can be employed if normal, MRD and cyst classes are considered for classification. If the result of this system is not cyst, the CAC system 2 can be used to enhance the classification accuracy of normal and MRD. Similarly, for liver images, the CAC system 3 can be used for the classification of normal and grades of fatty liver (mild, moderate and severe). If the output of this system is severe fatty liver, then CAC system 4 can be utilized for further clarification among severe fatty liver and cirrhosis.

CONTENTS

Chapter 1

Introduction

1.1 Motivation

The revolutionary advancement of technology has made a mark and come a long way in medical domain. From diagnosis to treatment, modern medicine is relying on technology complimentary to conventional clinical methods. A wide range of medical imaging modalities are available to view the anatomy, physiology and the functionalities of various structures of human body [1]. Each modality offers a unique dimension of information about the area of body under study and also has its own limitations. On one hand, efforts are being made to overcome the limitations and on the other hand, information from different modalities is being combined to have more clarity on the problem at hand.

Ultrasound imaging is often preferred as an initial examination to get the visuals of soft tissue structures like kidney, liver, gallbladder, pancreas, spleen, etc. The portability, cost-effectiveness, safety, convenience are the nature of ultrasonography considered for its preference over other modalities such as computed tomography (CT) and magnetic resonance imaging (MRI)[2]. Thus, it is more suitable to countries like India. However, the subjective interpretation of images is inevitably vulnerable to human error and the experts have to rely on invasive methods for confirming the conditions of patients. Invasive methods are uncomfortable and cause irritation to the patients, because of which people avoid the clinical examinations. It is also prone to biased results due to sampling error, morbidity and mortality. The speckle noise in the ultrasound image is both advantageous as it contains diagnostic information and disadvantageous as it obstructs in making clear diagnostic statements by the radiologists.

Kidneys have a crucial role to play for the mechanism of human body to continue its function. There is a spectrum of pathological conditions of kidney which are not clearly diagnosable by the radiologists. They are collectively termed as medical renal disease (MRD). It is clinically significant to distinguish MRD from other conditions of kidney at the earliest to administer appropriate treatment.

Liver is a metabolic centre of human body, carrying out the vital activities which are directly involved with the survival of an individual. The liver cells have the capacity to rejuvenate itself to some degree with small injuries. However, long-term dysfunction of liver makes it unable to carry out regeneration as it involves major functions in the body. Liver diseases are basically of two types i.e. focal liver diseases and diffuse liver diseases. In focal liver diseases, the

abnormality is confined to a localized area of the liver parenchyma. In diffuse liver diseases, the abnormality is spread all over the liver. The accumulation of excess triglycerides in extra-cellular space called vacuoles of liver cells is called fatty liver or fatty liver disease (FLD). Medical fraternity has defined three stages of FLD i.e. mild, moderate and severe corresponding to increase in severity of the condition. An advanced stage of fibrosis is termed as liver cirrhosis, which is considered to be an irreversible condition. Hence, clinically it is very significant to detect the process of fibrosis at the earlier stage.

1.2 B-Mode Ultrasound Imaging

Ultrasound imaging is a method which basically involves propagating a sound wave into the body and the reflected sound wave (echo) is processed to form an image. Thereby it forms the visuals of internal structures especially soft tissues of the body. There are various modes of ultrasound used in medical imaging. The one which is considered often and used in the present work is brightness-mode or B-mode. To understand few concepts that are dealt with, in the present work, looking at the basics of ultrasound imaging would be necessary.

1.2.1 Generation, propagation and reception of ultrasound waves

The sound waves of frequencies above human hearing threshold are considered as ultrasound waves. To generate these sound waves piezoelectric crystals are used in the transducers of ultrasound probe. The vibrations that are capable of travelling through the tissues in the body are generated by a piezoelectric crystal. The crystal has dual nature, that when a voltage is applied, it expands and relaxes back to its original thickness when the applied voltage is withdrawn. If the voltage is applied and withdrawn repeatedly, the crystal rapidly expands and relaxes, generating ultrasound waves. Another property is, when the ultrasound wave reflects from the object and hit the crystal, it is compressed and equivalent to the intensity of the reflected ultrasound wave a voltage is generated. Ultrasound probes are composed of large number of crystals.

Ultrasound waves are likely to reflect wherever air encounters biological tissue. Even a small bubble between a patient skin and probe is sufficient to reflect the ultrasound waves in lieu of penetrating the skin. Since it can propagate through liquid, thick liquid (jelly) between the probe and the patient skin is applied.

Some of the ultrasound waves are attenuated by the absorption of energy from the body. It is difficult to obtain the images of deeper structures, because the attenuation of the waves is more as the ultrasound waves have to cross more body tissues. Every substance such as muscles, fat, etc. has a property called ‘acoustic impedance’. Acoustic impedance is the degree of resistance

the body structure projects on the acoustic wave when it tries to pass through them. The acoustic impedance depends on the density of the body structure and the speed of ultrasound in it. When an ultrasound wave passes from one structure to another having different acoustic impedance, part of ultrasound wave continues to travel by slightly deviating from its actual direction into the second structure. This is referred as refraction. Another part of ultrasound wave is reflected back to the probe. The volume of ultrasound wave that reflected back and the difference in the acoustic impedance between the structures are directly proportional.

1.2.2 Image formation

Reflected waves are important as they provide information for the computer to further process that aid in the formation of the image. As the ultrasound waves cross from one tissue to the next, each with different acoustic impedance, some of the waves are reflected back at each crossing. Multiple reflected waves returning to the probe and gives information to the computer to display an image showing different tissues. The process of digital image formation from the reflected waves may be understood as below.

A wave of ultrasound is propagated through the probe in a narrow path. When the wave encounters a tissue (or any substance), a part of the wave is reflected back into the probe. The intensity of the reflected wave is indicated by a bright dot. The brightness of the dot and the intensity of the reflected wave are directly proportional. The part of the wave continued is reflected when it encounters another tissue. This reflected wave is registered as a bright dot on the screen. Thus, few dots of different brightness are formed along a line. However, when scanned at different lines of the object, a two dimensional image is formed on the screen. Since the scanning of structures and image redrawing many times a second happens so rapidly, one can see the changes in real-time. Ultrasound machine has few control knobs using which visual can be made better. For example, weakened signal strengths of deeper tissues to the greater attenuation over a long path can be compensated using time gain compensation (TGC) knob.

1.2.3 Speckle noise

Speckle is an inevitable multiplicative noise getting ingrained into the ultrasound images. It is an interference hampering the way of disease diagnosis as well as the algorithm developers of CAD systems. Yet, complete removal of speckle noise is not acceptable by the radiologists as it contains diagnostic information.

Tissues such as liver parenchyma, kidney parenchyma have inhomogeneity in their structures equal to or smaller in size than the wavelength of the ultrasound. These structures, though serve as a sound absorbing medium, scatter the sound waves because of the differing

acoustic impedance at microscopic level that lie closer. The scattered sound waves arrive out of phase at the sensor, causing a granular pattern on the image. This appears as bright specks in the realm of lighter background. This is termed as speckle. Speckle is not an absolutely unwanted interference in ultrasound. The speckle pattern is not completely random, as it contains information about the tissue. Each pathology give rise to a characteristic speckle signal. Speckle is a complex phenomenon in ultrasound image formation, which has the characteristics such as signal dependent, spatially dependent and non-Gaussian.

1.3 Anatomy, physiology and diseases with sonographic characteristics

In the present work, before understanding the implications of information from the ultrasound images, it is beneficial to have basics of anatomy, locality of organs of interest in the body and their normal functions. The nature of diseases that are considered in the current research work and their sonographic aspects are briefly described in this section.

The radiologists use visually recognizable features such as echogenicity and echotexture to distinguish normal condition from that of abnormal. Echotexture is a term used to describe a tissue structure that produces an echo. If the structure has same type of tissues or liquid with negligible or no differences of acoustic impedance, the reflection of ultrasound waves appears to be homogeneous. If the structure has different types of tissues, then the reflection of ultrasound waves shows varying shades, known as heterogeneous. Echogenicity is a relative term used to describe the intensity of echotexture of an area with respect to its vicinity. If the intensity of the area under consideration is more than its vicinity, it is called hyperechoic. If the intensity is less it is hypoechoic and if it is same as that of its vicinity, it is known as isoechoic. If the structure is not reflecting any echoes, then it is termed as anechoic.

1.3.1 Kidney

Kidneys are a pair of bean-shaped organs outwardly having a concave and convex side. Renal hilum is externally attached to the concave surface of the kidney, in which renal artery enter the kidney and the renal vein and the ureter leaves the kidney. The kidney is enclosed in a fibrous renal capsule. The dimensions of kidney are approximately, 11-14 cm in length, 6 cm in width and 4 cm in thickness. In humans, the kidneys are located in retroperitoneum, one on each side of the spine.

The functional unit of kidney is nephron, which is a urine producing structure. The area of an organ where its functional units are spread across is known as parenchyma. The major structures comprised in the kidney parenchyma are, the outer renal cortex and the inner renal medulla. The medulla region comprises of cone shaped renal pyramids with the broader base

being surrounded by the cortex and their apexes are pointing inwards. The cortex region extending in between the renal pyramids are known as renal columns. Renal corpuscle is the first portion of nephron located in renal cortex, where initial filtering takes place. Renal tubule is a passage of nephron extending from cortex into the medullary pyramids. A set of renal tubules drain the urine into a single collecting duct. The collected urine passes to the ureter through the passage of pyramids, minor calyces, major calyces and the renal pelvis. A cross-sectional view of kidney is depicted in Figure 1.1.

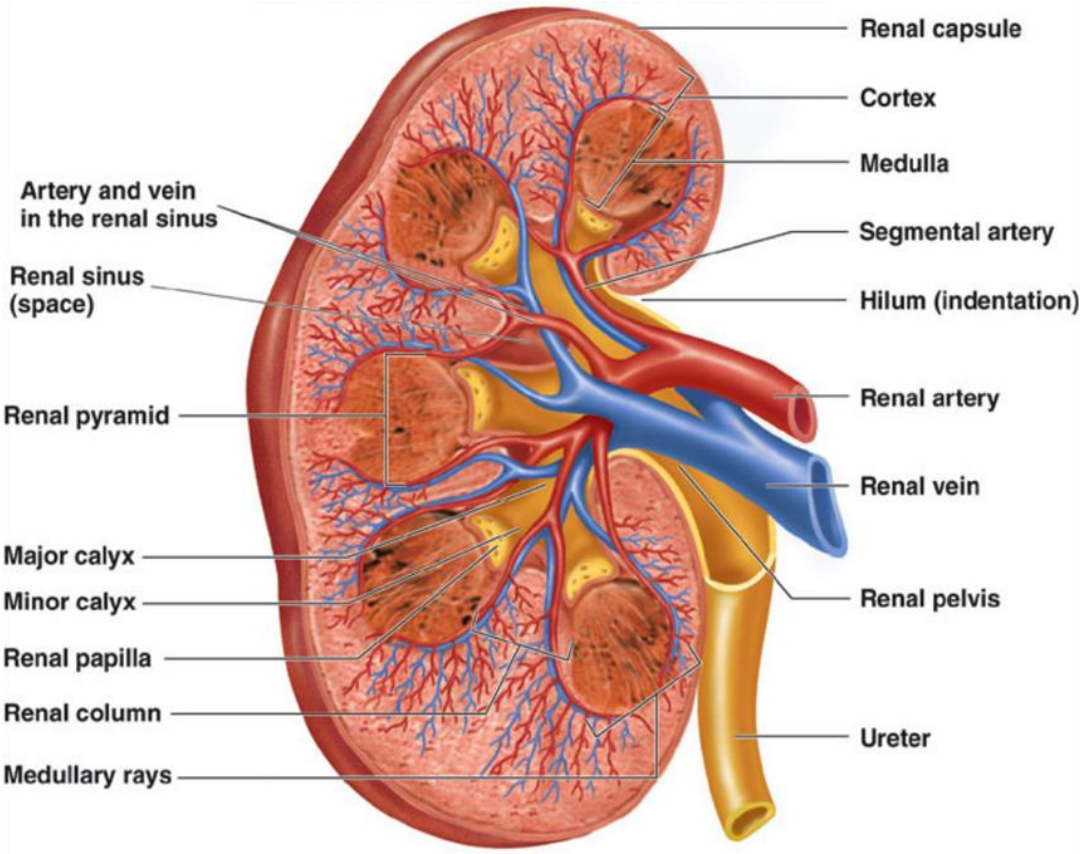

Figure 1.1: Cross-sectional view of kidney
Courtesy: http://healthfavo.com/wp-content/uploads/2013/08/human-anatomy-diagram-kidney.png

The main roles of kidney are serving homeostatic functions such as regulation of electrolytes, maintaining acid-base balance, maintaining water-salt balance thereby regulating blood pressure. They remove urea and ammonium through urine. They are responsible for absorbing water, glucose and amino acids. They produce vital hormones such as erythropoietin and enzymes like renin [3].

1.3.1.1 Normal

The normal condition of an organ cannot be characterized as the conditions of a disease are outlined. However, the sonographic features of a normal organ can be described and the

variation in these features corresponds to the diseased conditions of an organ. A sample of B-mode ultrasound image of normal kidney is shown in Figure 1.2.

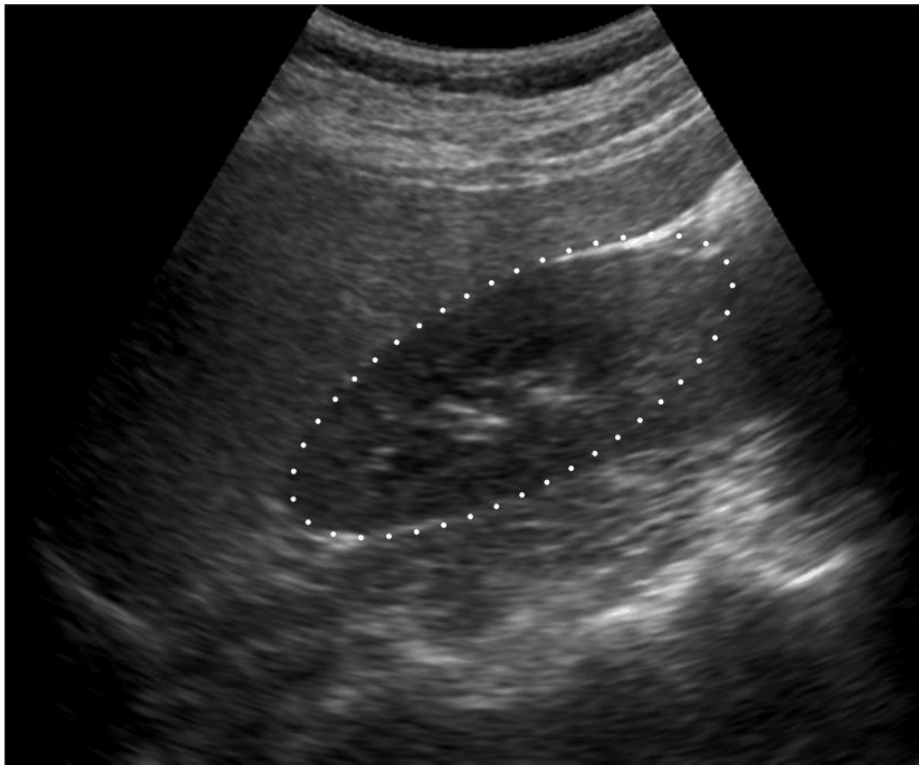

Figure 1.2: B-mode ultrasound image of normal kidney. The dotted ellipse marks the boundary of the kidney

The renal parenchyma is homogenous in textural appearance. It is hypoechoic compared to normal liver parenchyma. The pyramids of renal medulla are rounded triangular structures, evenly arranged in the kidney, appear hypoechoic than the cortex. The central renal complex, comprising the major and minor calyces and the surrounding fat, appears as an echo-rich, white, irregular shape lying centrally [4].

1.3.1.2 Medical renal disease (MRD)

The disorders such as haematuria, proteinuria, pyuria, polyuria, etc. cause the functional unit of kidney i.e. nephrons to be accountably diseased partly or completely. Accordingly, the nephron structures appear hyperechoic and heterogeneous than in normal condition. Since, nephrons are miniature units and are arranged so closely, it becomes difficult for the radiologists to diagnose those diseases. Such diseases are categorized as medical renal disease. Thus the parenchyma of MRD is hyper-echoic than normal and the distinguishing between cortex and medulla becomes hardly possible [5]. An example of B-mode ultrasound image of MRD is shown in Figure 1.3.

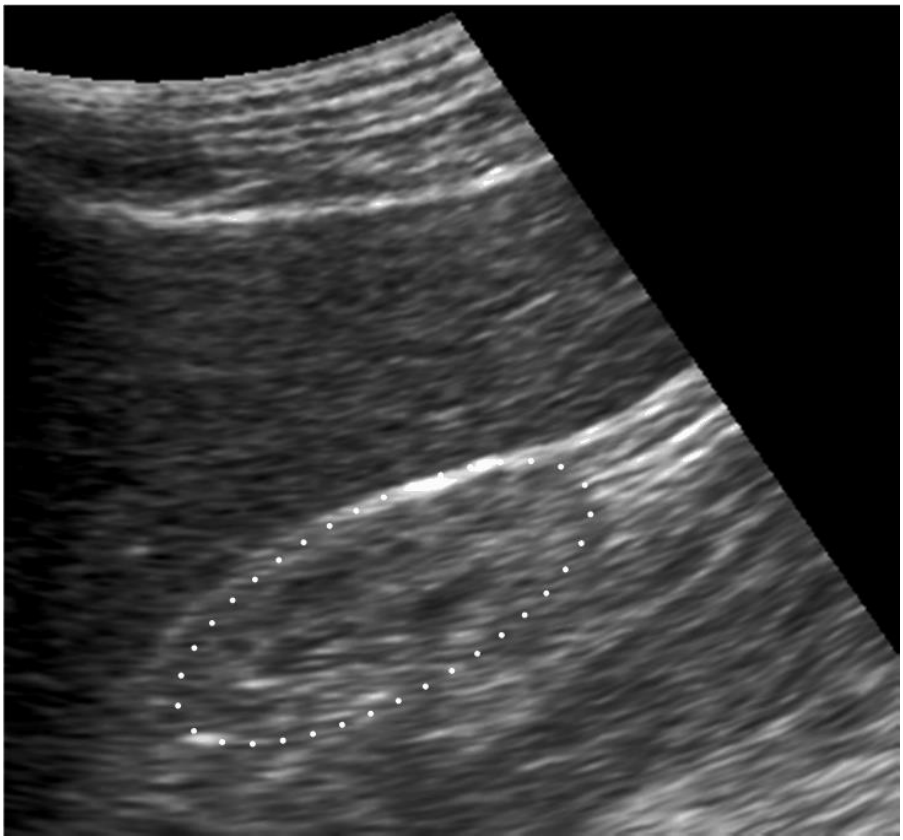

Figure 1.3: An example of MRD image with dotted ellipse representing the boundary of kidney

1.3.1.3 Cysts

A renal cyst is a fluid filled region in the kidney. They usually appear in cortex region, but also possible in medullary and renal sinus regions. Most of the time, they are benign and are monitored without intervention. However, some cysts might be cancerous and are considered to remove in nephrectomy, a surgical procedure. Sometimes, there is a possibility of being confused with renal sinus cyst as hydronephrosis [6].

A sample of cyst condition being displayed in B-mode ultrasound modality is shown in Figure 1.4. On ultrasound images, benign cysts are anechoic with no internal echoes. They have a smooth thin wall with posterior acoustic enhancement [7].

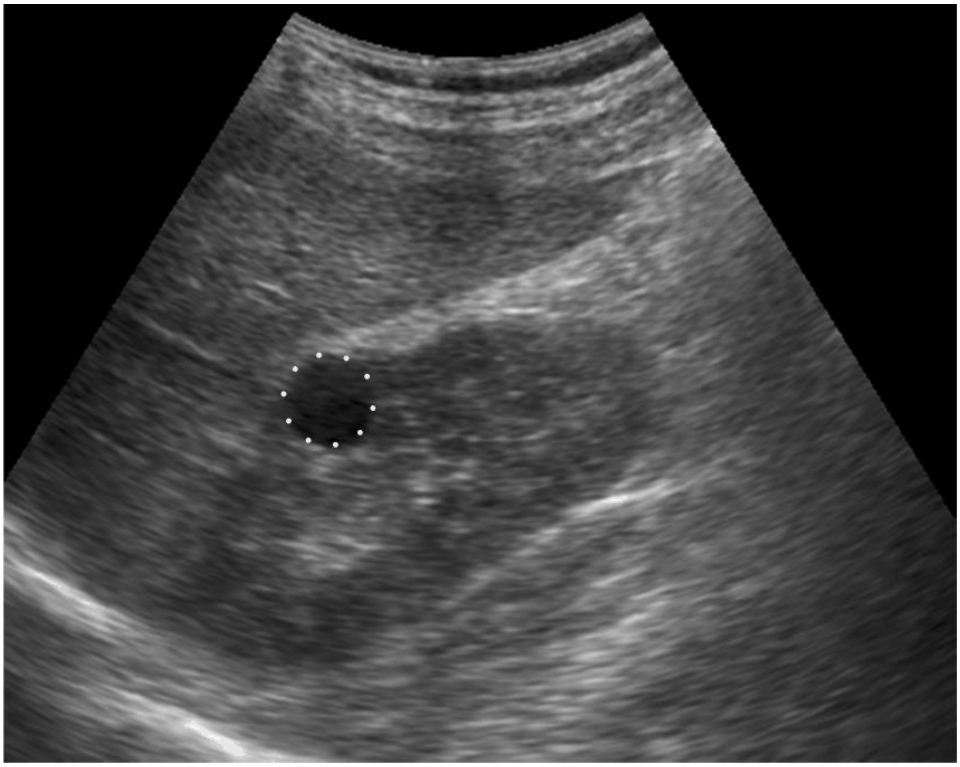

Figure 1.4: B-mode ultrasound image of a cyst with a dotted circle emphasizing the region

1.3.2 Liver

Liver is a largest organ as well as largest gland of the human body. It is considered as a gland, because it synthesizes hormones to be released into the bloodstream. It weighs around 1.5 kg. It is located in upper right quadrant of abdomen below the diaphragm, beside the stomach and under the ribs. It extends a part way into the upper left abdomen. It has four lobes, traditionally which is based on outer appearance of liver, two lobes i.e. right lobe and left lobe are visible from the frontal view and other two lobes are visible from underside view. The right lobe is larger compared to left lobe. The division of liver into independent 8 segments based on functionality is referred as Couinaud classification. The segments are numbered in roman as I to VIII. An illustration of location and lobes of liver is shown in Figure 1.5.

Liver is supplied by hepatic artery and portal vein. Oxygenated blood enters liver by hepatic artery which is a branch of the coeliac trunk that arises from aorta, whereas nutrient rich blood from the gastrointestinal and also from the spleen and pancreas enters liver through portal vein. These blood vessels branches into small capillaries leading to the functional units of liver, lobules. Each lobule is structured with numerous hepatic cells (or hepatocytes), where the metabolic activities take place.

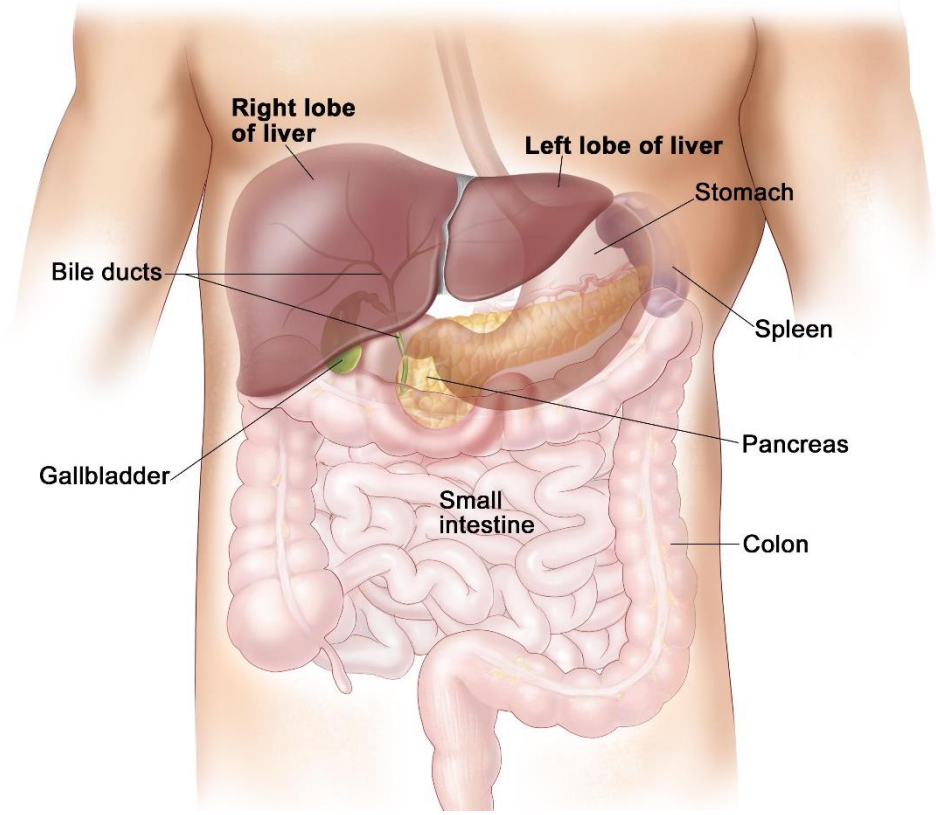

Figure 1.5: Illustration of location and lobes of liver
Courtesy: http://www.cancer.gov/images/cdr/live/CDR658698.jpg

The liver is responsible for carrying out 500 functions in coordination with other organs and systems. Because of such a complex network of functions, currently there is no artificial organ to take over in case of liver malfunction. Some of the major functions of liver include protein synthesis, production of various biochemicals to aid the digestion process and detoxification of intermediate and products of metabolism [8].

1.3.2.1 Normal

The normal liver has homogeneous echotexture and it is isoechoic or slightly hyperechoic in comparison with the renal cortex and hypoechoic with that of spleen [9]. The major structures such as hepatic artery, portal vein, bile duct and other vessels appear anechoic in relation to normal liver texture. The border of liver near to diaphragm and the diaphragm itself is hyperechoic than the liver texture [6].

Liver, because of its multi-functionality, is more prone to become diseased. However, the liver has a potential to continue for a long time with disease. Only when considerable damage has happened that interferes with the normal function of liver, it starts exhibiting symptoms. The major categories of liver disease are focal liver disease and diffuse liver disease. In focal liver diseases, the abnormality of liver parenchyma is confined to a localized area, whereas in diffuse

liver diseases, the abnormality is diverged throughout the liver [10]. The stages of diffuse liver disease, considered in the present work are described below.

1.3.2.2 Fatty liver disease (FLD)

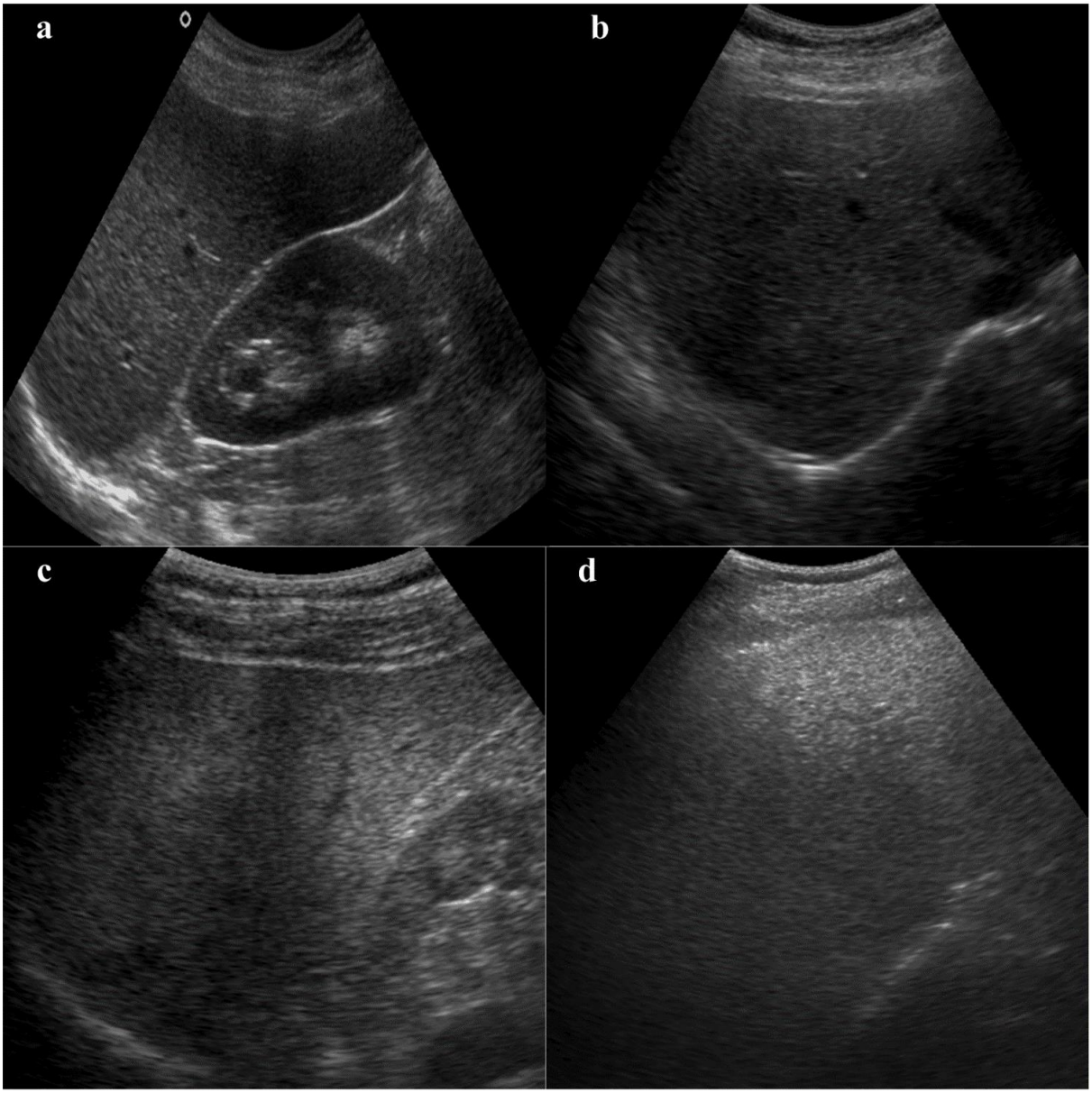

Figure 1.6: Sample images of (a) Normal (b) Mild (c) Moderate and (d) Severe fatty liver

The deposition of triglycerides in hepatocytes initiates the reversible disorder of metabolism, known as fatty liver disease (specifically known as non-alcoholic fatty liver disease). Due to the deposition of fat in liver cells, it becomes unable to retain sufficient blood in them leading to hepatic fibrosis. Depending on whether the fat deposition is diffused or focal, fatty liver is categorized into two major classes [11]. In the present work, diffuse fatty liver condition is considered. The histological and pathological findings have validated the phenomenon that, diffuse liver disease severity increases in accordance with the hepatic fibrosis

advancement [12]. Accordingly, medical fraternity has defined three stages of fatty liver, based on the degree of severity. They are mild, moderate and severe fatty liver. This categorization would be useful for treatment planning and further investigations. Ultrasound imaging is a reliable non-invasive tool for the diagnosis of fatty liver [6]. A sample images of normal and grades of fatty liver are shown in Figure 1.6. Standard sonographic characterizations of mild, moderate and severe fatty liver are as follows:

a. *Mild fatty liver*: with minimum diffuse of fat deposition, there is increase in echogenicity of liver. The visibility of diaphragm and blood vessel borders are normal.

b. *Moderate fatty liver*: diffuse of fat deposition and echogenicity of liver have further increased than in mild fatty liver. The visibility of diaphragm and blood vessel borders has slightly diminished.

c. *Severe fatty liver*: There is an extensive increase in echogenicity. Because of increased attenuation at liver, the part of liver near diaphragm will be hypo-echoic. The diaphragm and blood vessel borders are poorly visible or nonvisible [13].

1.3.2.3 Liver cirrhosis

Cirrhosis is an advanced irreversible stage of diffuse liver disease. Fatty liver disease is one of the possible causes behind cirrhosis. Fatty liver disease is a progressive disease characterized by the inflammation of liver and fibrosis. If the condition is not detected at the initial stages, this will lead to cirrhosis. Up to 20% of fatty liver disease patients develop liver cirrhosis. Only 60% of liver cirrhotic patients show signs and symptoms [11]. Although, biopsy is considered as standard diagnostic tool, it is invasive. Thus, ultrasound is used as a non-invasive screening method for diagnosis. A B-mode ultrasound image example of cirrhotic liver is shown in Figure 1.7.

Figure 1.7: Sample B-mode ultrasound image of cirrhotic liver

Cirrhosis is associated with the replacement of liver tissue by scar tissues and nodules due to attempted repair damage tissues. These associations leads to modifications in normal hepatic appearance such as increased echogenicity, heterogeneity, alteration in liver size, nodular surface and damaged hepatic vessels [14-18]. The increased echogenicity may be emphasized by increased time gain compensation (TGC) settings in obese patients. As in fatty liver disease, radiologists do not consider the visibility of diaphragm as a reliable feature of cirrhosis because of its inconsistence [6].

1.4 Need for CAC system and its enhancement

With the revolutionary advancement of technology, the utilization of imaging and the computer algorithms have increased enormously [19-26]. The idea of CAD system is to provide a computer output as a secondary observer to assist radiologists and other health care professionals in image readings [27-40]. Three main areas of CAD system are:

- General processing – image acquisition and digitization, image quality verification and re-acquisition.
- Pre-processing – segmentation, image rotation, unbounded pixel elimination.
- Analysis – ***feature extraction***, ***classification***, and other applications.

Each of the pixels in a region is similar with respect to some characteristic or computed property, such as colour, intensity, or texture. Adjacent regions are significantly different with respect to

the same characteristic(s). The characterization of tissues using one or combinational property to categorize them into respective classes is termed as classification [41, 42].

The reasons for the need of CAC system pertaining to the current work are:

a. To extract information from the images which normally not able to capture from visual inspection of ultrasound images.

b. To overcome the inter- and intra-observer variability, an inevitable limitation of subjective diagnosis.

c. To increase the potential of CAC system based on B-mode ultrasound images so that diagnostic confidence is elevated, thereby its utilization is extended in countries like India.

The CAC systems are application dependent. Hence, the way images are interpreted by the radiologists needs to be utilized in developing a CAC system. This aids in improving the performance of CAC system from medical perspective [13]. To further improve the performance of CAC system from technical perspective, appropriate modifications and new methods can be annexed at one or more stages of CAC system. In the present work, the CAC systems involved the following stages: ROI marking, feature extraction, feature selection and classification. The same methodologies are employed in these stages of CAC system meant for kidney and liver databases to evaluate their potential. Inputs from medical or/and technical perspective have been proposed for enhancing the performance of CAC systems.

1.5 Literature Survey

1.5.1 Introduction

Medical image analysis is an interesting as well as challenging field of research. It is interesting because of the close association with the human body, health and deeper understanding of mechanisms involved in well-being of an individual. The limitations of medical imaging modalities and the artifacts interfering in developing computer algorithms for image interpretation are the exhibiting challenges in this area of research. Medical image analysis involves meeting of medical experts and algorithm developers. With the intention to provide possible objective aid to assist medical fraternity, contributions from both the medical experts and algorithm developers are necessary.

The significance of literature survey in research has many dimensions. Particularly, in medical image analysis the following factors need to be considered.

a. The problem which essentially requires computer-assistance, as CAC systems are application dependent.
b. The frequency of the cases for the availability of sufficient data for research.
c. The published literatures on the same line to carryout work there upon or to improve upon the existing methods.

The contributions in the present work include the possible input from the medical domain as well as from technical aspect. Accordingly, the literature survey corresponding to kidney image classification, de-speckling of ultrasound for classification, liver image classification, texture features and feature selection are covered in following sections.

1.5.2 Kidney image classification

In literature, few attempts have been made towards the classification of ultrasound kidney images. Bommanna Raja, et.al, have studied the classification of normal, MRD and cyst classes by extracting kidney region [43] and using different features [5]. In [5], authors have extracted 36 features from six categories. The process of ranking the features has been employed to reduce the number of features. The classification efficiency of the hybrid fuzzy system mentioned is 96% for normal, 92% for MRD and 96% for cyst. In [7], authors have obtained 86.6% for normal, 76.6% for MRD and 83.3% for cyst using Gabor wavelet features. There has been an attempt to classify the ultrasound kidney images using content descriptive power spectral features [44] and multi-scale differential features [45]. In [46], authors have used 28 multiple descriptive features with 13 highly significant for the classification. With ANN as a classifier, accuracy of 90.4% for normal, 86.6% for MRD and 85.7% for cyst have been obtained. In their study, the whole kidney area has been considered for extracting features. Whereas, the radiologist opined that the characteristic changes in MRD with respect to normal is in parenchyma of kidney and the cysts are focal in nature.

1.5.3 De-speckling of ultrasound for classification

Speckle noise in B-mode ultrasound images makes visual diagnosis a difficult task, but it also contain diagnostic information which is preferred by the radiologists. Various de-speckling methods have been proposed in literature [47-51]. Recent review [52] on comparison of fifteen de-specking methods on echocardiographic images concludes that oriented speckle reducing anisotropic diffusion (OSRAD) method is best for medical application. In [53], OSRAD has been recommended as a pre-processing step for segmentation task. In [54], speckle reducing anisotropic diffusion (SRAD) has been modified for processing the images before the classification task. Modified SRAD has shown improvement with respect to SRAD.

1.5.4 Liver image classification

In literature, there are many contributions towards classification of normal, fatty liver and cirrhosis using different features [55-59]. Only recently [60], grades of fatty liver along with normal liver are considered for numerical grading. In their study, gray relational analysis (GRA) method has been utilized for numerical grading of fatty liver based on brightness level comparison between liver images and kidney parenchyma as reference from the same subject. But, this factor is not reliable as the echogenicity of kidney parenchyma changes in case of kidney diseases [13]. The most frequently considered factors are increased liver echogenicity, impaired visualization of hepatic vessels and diaphragm [6].

CAC systems have been proposed for normal and cirrhotic liver images [10, 14-18]. Radiologists opined that, differential diagnosis between severe fatty liver and cirrhotic liver images is a challenging task, as the latter may be an advanced stage of former condition. Also the differential diagnosis between severe fatty liver and cirrhotic liver is clinically significant as FLD is reversible, whereas cirrhosis is not.

1.5.5 Texture features

In case of US images, texture features are predominant and have been used for classification tasks [61-63]. From the literature survey pertaining to above sections, different texture features are selected for the present work based on their frequency of usage and performance. The feature categories considered are first order statistics based features, moment invariant features, gray level co-occurrence matrix features, run-length matrix features, Laws texture energy features. In addition to these, gradient based features are considered to explore its potential in the present classification tasks. The detailed descriptions of these features are presented in next chapter on methodology.

1.5.6 Feature selection

The interaction among features in performing the given classification task is another important aspect which should be considered while designing an efficient CAC system. This can be accomplished by removing unnecessary features. Basically feature space dimensionality reduction can be approached either by transformation based feature reduction or by feature selection. In the present work, feature selection approach has been used. Differential evolution feature selection (DEFS) being the recent method, has shown better performance with competitive methods [64] and hence DEFS has been used.

1.6 Objectives

Based on literature survey and the need for enhancing the performance of CAC systems, the objectives for the present work are stated as follows:

1. To research the significance of considering appropriate ROIs for the classification of B-mode ultrasound images.
2. To explore the potentiality of features from de-speckled images for the classification of B-mode ultrasound kidney images.
3. To evaluate the performance of texture features with respect to de-speckling methods for the classification of B-mode ultrasound kidney images.
4. Explore the ways to enhance the performance of classification of fatty liver images.
5. Exploring the optimal texture features for the classification of B-mode ultrasound images.
6. Investigate the ways to improve the potentials of feature selection process.

1.7 Overview of the present work

A radiologist, interprets an image of kidney as well as liver, but consider the distinguishing characteristics of an organ and diseases accordingly. On the same line, to have the CAC systems for different organs and diseases, but common methodologies for the stages of CAC system is the idea behind the present work. It is also possible to know what methodology is suitable for kidney and liver. So, two databases of kidney and liver are considered, but the algorithms used at different stages of CAC systems are maintained the same for both databases. An overall flow of present work is depicted in Figure 1.8.

In first part, CAC systems for kidney images are proposed. In literature, CAC systems have been proposed by considering normal, MRD and cyst classes of kidney using B-mode ultrasound images. Accordingly, a CAC system is developed to make improvement. The opinion of radiologist was that cysts are easily recognizable comparatively. So, another binary CAC system is developed for classifying only normal and MRD for two reasons: to improve classification performance further compared to the previous one and to avoid the biased result of cyst.

In literature, few studies have been proposed which considers classifying grades of fatty liver (mild, moderate and severe). The classification of grades of fatty liver is clinically significant for treatment planning and the severe fatty liver (reversible stage) may develop into liver cirrhosis (irreversible stage). Hence, the early detection of the stage of the disease is of at most important. In second part, a CAC system is developed for normal and fatty liver images. To overcome the

ambiguity between severe fatty liver and liver cirrhosis, a separate binary CAC system is developed.

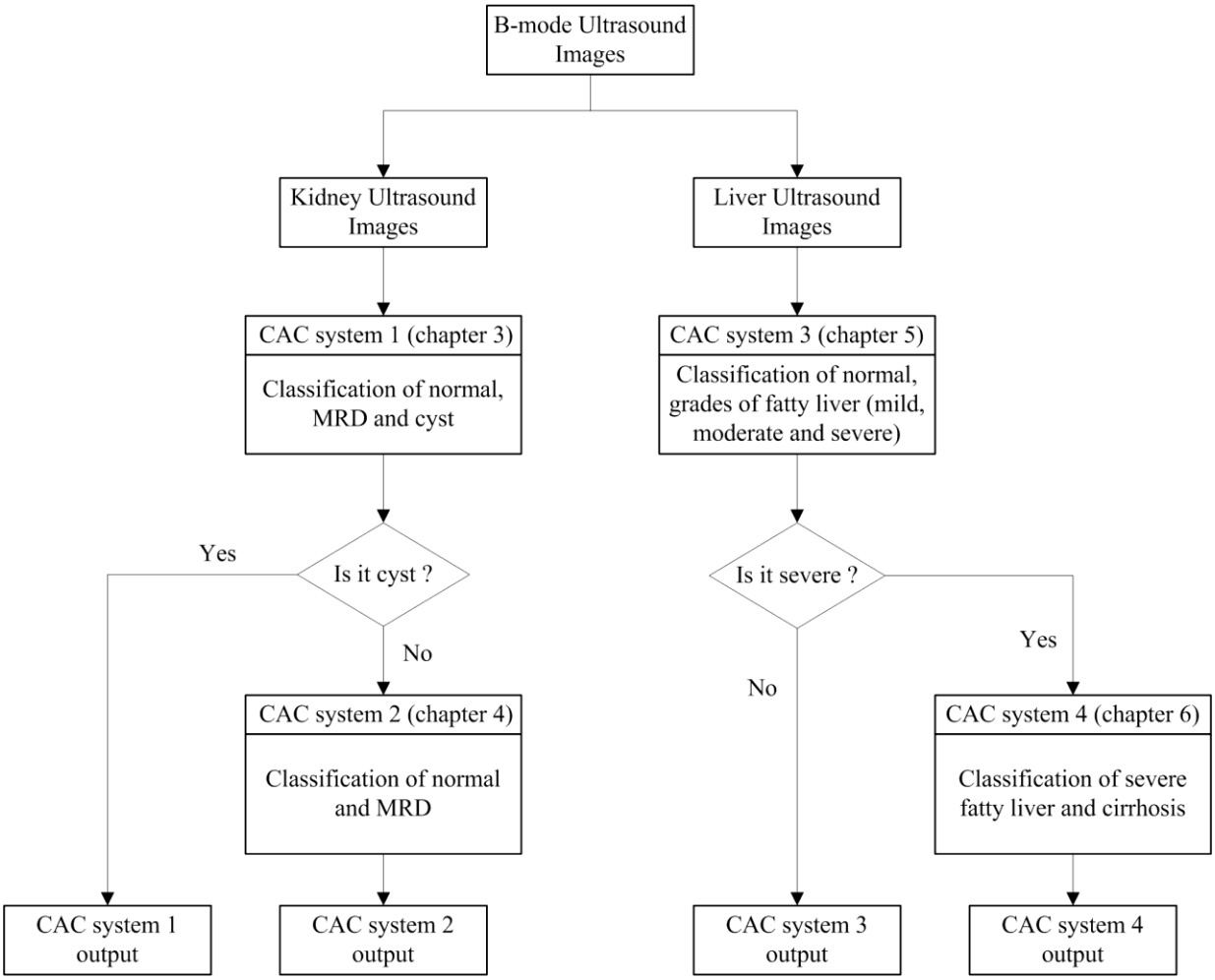

Figure 1.8: Block diagram representation of the present workflow

1.8 Organization of thesis

The thesis of the present work is organized into seven chapters. The brief descriptions are stated below.

Chapter 1: With necessary introduction to medical imaging, image formation and analysis, the attributes of various classes of B-mode ultrasound images considered in the present work are described. The basis of objectives for the present work, literature survey and the need for improving the CAC systems are discussed in this chapter.

Chapter 2: The protocols followed for data acquisition and the ethics involved are being mentioned. Various methods used at different stages of CAC systems such as texture feature extraction, feature selection and classification are described in detail in this chapter.

Chapter 3: With the introduction to the CAC system for the classification of B-mode kidney ultrasound images, data involved in the study, experimental results are described in detail in this chapter.

Chapter 4: The necessary introduction to the extension of work in chapter 3 is presented with the data used for the study. Evaluating the potential of texture features extracted from images de-speckled by various methods for the classification of normal and MRD images is the objective. The purpose of the study has been justified with the exhaustive experiments and their results are presented in this chapter.

Chapter 5: This chapter is on CAC system for the classification of normal and grades of fatty liver using B-mode ultrasound images. The data used for the study and experimental results are presented here.

Chapter 6: With the necessary changes required from that which is discussed in chapter 5 lead to unique CAC system for the classification of severe fatty liver and cirrhosis. The data required for the study and the experimental results are described in this chapter.

Chapter 7: Overall conclusions drawn from all the CAC systems proposed in the present work are mentioned in this chapter. The limitations and the future possibilities pertaining to the present work are also presented here.

1.9 Concluding Remarks

The necessary foundations have been lied out by beginning with the motivation for the present work. Introduction to kidney and liver disease classes under consideration are explained. The need for CAC systems and its further enhancement are discussed. The literature survey which led to the objectives of the present work is described. The organization of different aspects of the thesis is also included in this chapter. The next chapter is focussed on detailed descriptions of methodologies employed in the present work.

Chapter 2

Methodology

2.1 Introduction

The research methodology is a blueprint that represents the intended path to be followed to meet the objectives that have been set. In accordance with the present work, it comprises of crucial steps such as setting the objectives, formulation of possible methods, data collection, extracting relevant information in an appropriate format, exhaustive experimentation to arrive at significant conclusions.

In research area such as medical image analysis, the crucial step is finding objectives based on research gap as well as the requirement of the radiologists and it also necessarily involves the availability of sufficient cases. To meet these conditions, valuable interactions with the radiologists are a pre-requisite. Hence, a memorandum of understanding (MoU) has been signed between the Indian Institute of Technology Roorkee (IITR) and Himalayan Institute of Hospital and Trust (HIHT), to support each other in the research work.

The standard database for ultrasound images of kidney and liver are hardly available. The researchers in this area have to obtain their own database. Thus, quantitative comparison of their results becomes rarely possible. The data collection phase is a time consuming process, because it depends on the patients with a particular disease considered for the research objective, visiting the hospital for diagnosis. In the span of two years from 2012 to 2014, the images of kidney and liver are collected. The medical images of patients are conventionally related to them. Therefore, it is necessary to obtain the acceptance of patients and ethical clearance from the respective committee in prior to the acquisition of images. It is also necessary to ensure that the images are used for research purpose only by maintaining the confidentiality, dignity and anonymity of patients.

The present work has four different CAC systems followed by its own datasets distribution, experimental stages. Thus, the common elements involved in these four CAC systems such as protocols pertaining to data acquisition, regions of interest (ROIs), feature extraction methods, feature selection procedure and the classification system are described in this chapter. The task of data acquisition and the selection of ROIs are mainly performed by the experienced radiologist. A simple MATLAB has been written by the researcher to assist the radiologist in marking the ROIs and to save the respective details. The other modules are designed by the research scholar intending to achieve the objectives.

2.2 Medical ethics and ethical clearance

The medical ethics are basically the values set from humanity perspective which must be followed during clinical practice and medical imaging research. Ethical guidelines indicate the mutual coordination principles on researchers, radiologists as well as the patients/subjects involved in the research activity. The recognized institutions and hospitals across the world have an Institutional Review Board (IRB) to review the submitted research proposals in terms of the ethical issues involved in undertaking a research activity. The IRB generally involves health care professionals and the philosophers to ensure that the researcher has considered all the significant ethical issues while formulating the research procedures, so that there is no ethical conflict by undertaking the research activity. After a thorough investigation of the submitted research proposal the IRB may impose certain additional guidelines to make sure the safety and rights of the patients/subjects. The crucial review of research proposals by the IRB in turn helps the researcher as well as the organization against possible legal actions of ignoring to address important ethical issues concerning patients/subjects.

The aim of the present research work is to do value addition in the diagnostic performance obtained by most commonly available conventional gray scale B-Mode US imaging modality for diagnosis of kidney and liver diseases. The present research work is related to human healthcare and the collection of database of B-Mode kidney and liver US images with representative images of respective sub classes under study from various patients is absolutely necessary. Therefore for the present research work the author was required to obtain the ethical clearance from the medical ethics committee of the associated medical education and research institute, i.e., Himalayan Institute of Hospital and Trust (HIHT), Dehradun. The medical ethics committee of HIHT approved the research proposal submitted by the author after examining the research problem, and imposed the following research ethics for the researcher to follow:

i. The researcher will not involve in any procedure which may infringe or interfere with the medical ethics.

ii. The researcher will not provide any input to the participating radiologists, as it may bias their opinion regarding the medical management.

iii. The researcher would be required to obtain consent from the patients before collecting the data.

iv. There should be no disclosure of personal information of the patients in any of the publication by the researcher.

v. The data collected by the researcher would be used for academic purposes only.

2.3 Data acquisition, assessment and description

The database required for the present work was unique and the author had to request the radiologist for acquisition of images of respective classes corresponding to the objectives. The data acquisition period was from 2012 to 2014. The images of required classes are collected from patients with their consent in prior. The B-mode ultrasound images are collected from Siemens ACUSON X300 ultrasound machine. All images had their own clinical settings such as time gain compensation, magnification, dynamic range, focal lengths for obtaining best view.

The experienced participating radiologist confirmed the presence of diseases by assessment criteria, including (i) visual inspection of sonographic features according to their expertise, (ii) follow-up of clinical history of the patient and other associated findings, and (iii) imaging appearance on dynamic helical computed tomography (CT)/ magnetic resonance imaging (MRI) / pathological examinations and biopsy.

The database used in the present work consisted of 35 kidney images comprising of 11 normal, 16 cysts and 8 MRD images and 69 liver images which includes 12 normal, 14 mild fatty liver, 14 moderate fatty liver, 13 severe fatty liver and 16 cirrhotic liver images. The images are of size 800×600 pixels with 256 gray levels and 96-dpi resolution.

2.4 Region of interest (ROI)

The region of an ultrasound image that has pixels of interest to provide diagnostically relevant information is region of interest (ROI). The selection of ROI is a vital step, which decides the performance of a CAC system in characterizing the tissues of ultrasound images. The ROIs are required when sufficient number of images are not available or/and area of interest is confined to a small region. The use of ROI as an input image for feature extraction reduces the complexity of the process and hence the time involved. But, the selection of ROI size is significant as texture measurements are sensitive to ROI size. From other studies [56, 65-68], it has been noted that the ROI size must be of at least 800 pixels to provide good sampling distribution for estimating reliable statistics. At the same time, the ROI size must fit within the area of relevant information. After the trail with the classes of images in the present work and interaction with the radiologist, ROI window size of 32 × 32 pixels has been selected. The automatic selection of ROI has both limitations and complications involved in the process. Hence, in the present work ROIs are selected manually by the experienced participating radiologist. To ease the process, a MATLAB program has been provided by the researcher which involved loading an image, selecting a point to place the ROI window and save the respective

details after confirming the ROI's location. The protocols used in selecting ROIs from different classes of images for each CAC systems have been described in respective chapters.

2.5 Feature extraction

The primary requirement for quantitative analysis of images in CAC systems is the numerical or quantitative representation of characteristics of images, which are termed as features. The process wherein mathematical methods are used to obtain the relevant features for the task at hand is known as feature extraction [69, 70]. Ultrasonic images exhibit texture as one of its characteristics attribute and the approach to characterize tissues using texture is called texture analysis.

Texture of an image can be defined as a descriptor of local intensity variations in the neighbourhood. The texture depends on the number of pixels considered. The basic pattern and repetition frequency of a texture sample could be invisible to the naked eye, although quantitatively detectable. The texture descriptor provides the measure of characteristics such as smoothness, coarseness and regularity. Ultrasound images also have textural surface generated by the echoes of ultrasound waves from soft tissue structures. It is difficult to standardize the terms used to describe the texture in ultrasound images because of subjective interpretation. Ultrasonic texture is characterized by sonographic features. These features are basically based on echotexture and echogenicity appearances of tissues under consideration. The radiologists differentiate tissues by visualizing various sonographic features. The studies [71-75] have shown the correlation between quantitative analysis of ultrasound texture features and radiologists subjective interpretation of images. Thus, in the present work, texture features are considered to meet the set objectives.

The aim of feature extraction module is to extract features which bring forth most of the discriminatory information from the images and contribute in the better performance of CAC systems. In the present work, feature extraction methods are selected majorly based on literature survey and also on possible potentiality of the method. The selected feature extraction methods and their features are described as follows.

2.5.1 First Order Statistics (FOS) features

The parameters that measure the possibility of a particular gray value within selected region of an image are categorized as first order statistics [76, 77]. The digital image is a two dimensional array of pixels and the intensity gray-level values of pixels vary from 0 to 2^b-1, where b is the number of bits of that image. The ultrasound images used in the present work have 8-bits representation. Thus, the intensity gray-level values of pixels vary from 0 to 255. The gray-

level values of the pixels in the region of interest can be characterized by the histogram, which is a frequency distribution function that shows the number of pixels for each intensity level in the whole range.

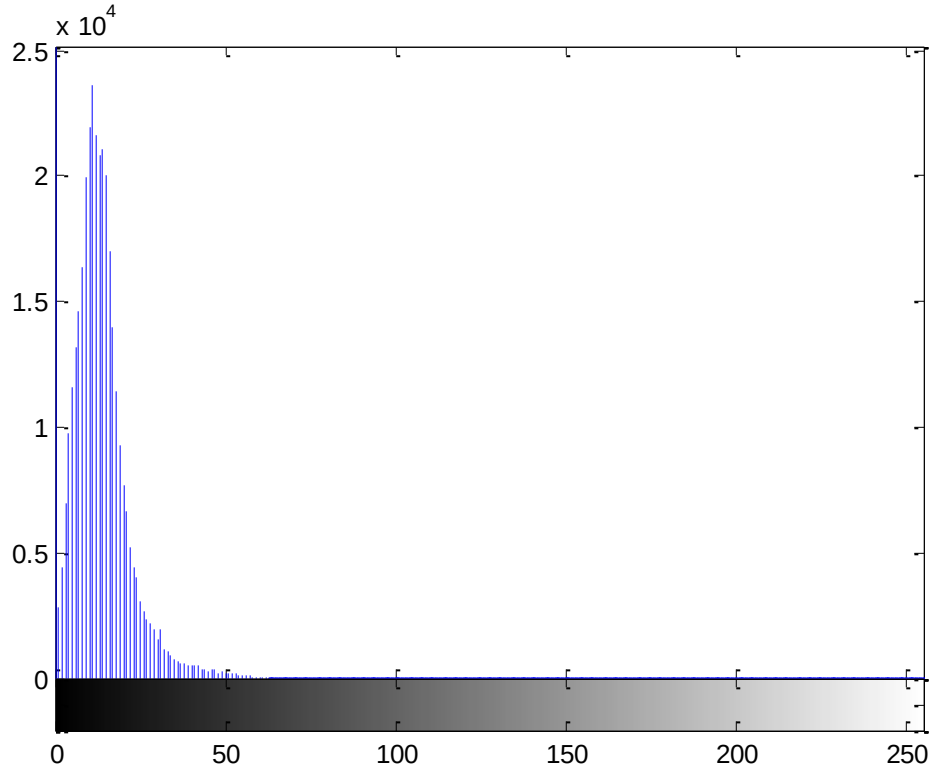

Figure 2.1: Histogram of an image representing the number of pixels (along y-axis) of each intensity gray-level value (along x-axis)

Figure 2.1 is a concise and simple summary of the statistical information contained in the image (histogram of image shown in Figure 1.6 (a)) of size 800 × 600. Each intensity gray-level value is represented along x-axis and the number of pixels having a particular gray-level value is represented along y-axis. A gray-shade bar along x-axis also shows that the gray-level value 0 corresponds to black colour and 255 corresponds to white colour in the image. First order statistics can be computed from the histogram, as they are dependent on individual pixel values rather than the interaction of neighbouring pixel values.

First order statistical measures are calculated based on central tendency, diversity, shape and entropy of the distribution of pixel intensities of region of interest. The features considered in the present work are: Mean, Variance, Skewness, Kurtosis, Energy[5, 17], and Percentile (1, 10, 50, 90 & 99) [78, 79]. Totally, 10 FOS features are estimated.

Mean is the sum of intensity gray-level values of pixels over number of pixels under consideration. Mean is the first central moment and represents the average gray-level value of the region considered. As mean is the numerical value of central tendency, it is often used. An exceptionally large or small gray-level values of few pixels can significantly vary the mean value, hence it is sensitive to extreme values of the pixels. Thus, it more appropriate for symmetrical distributions. The formula for calculating the mean is

$$Mean = \frac{1}{MN}\sum_{i=1}^{M}\sum_{j=1}^{N} I(i,j)$$

Where *I(i,j)* represents a two dimensional image intensity function.

I,j are variables varying from 1 to M and 1 to N respectively.

Variance is an average of the squared deviations from the mean of intensity gray-level distribution in an image. It is the second central moment and calculated using the formula

$$Variance = \frac{1}{MN-1}\sum_{i=1}^{M}\sum_{j=1}^{N} (I(i,j) - \bar{x})^2$$

Where $\bar{x}$ represents the mean of gray-level distribution in an image.

Skewness is the third central moment and gives the measure of symmetry and asymmetry of the gray-level values around the mean. Asymmetry of histogram to the left is given by negative value of skewness and to the right is given by positive value of skewness. Thus, the skewness of normal (or symmetric) distribution, which has a 'bell shape' is zero. The formula for calculating skewness value is

$$Skewness = \frac{1}{MN}\sum_{i=1}^{M}\sum_{j=1}^{N} \left(\frac{I(i,j) - \bar{x}}{\sigma}\right)^3$$

Where σ is standard deviation (square-root of variance), which is the spread of gray level distribution around the mean.

Kurtosis is the fourth central moment, measures how close an intensity distribution is to the normal distribution. Thus, it is the degree of peakedness if a distribution. For a balanced normal distribution w.r.t peakedness, kurtosis value is 3. Distribution that are more prone to outliers than normal distribution have heavy tails and peakedness with kurtosis value greater than

3. Distribution with light tails and flatness are less prone to outliers and the kurtosis value will be less than 3. It is calculated by the formula

$$Kurtosis = \frac{1}{MN}\sum_{i=1}^{M}\sum_{j=1}^{N}\left(\frac{I(i,j)-\bar{x}}{\sigma}\right)^4$$

Energy of the pixels of region can be a distinguishing measure. It is the squared sum of gray-level values of pixels over number of pixels. More the energy implies that much of the pixels have higher gray-level values and vice-versa.

$$Energy = \frac{1}{MN}\sum_{i=1}^{M}\sum_{j=1}^{N}\left(I(i,j)\right)^2$$

Percentile indicates a value below which given percentage of gray-level values may be found in the region of interest. For example, percentile of 1% = 75, means 1% pixels of the region are having gray-level value less than 75. In the present work, percentile of 1%, 10%, 50%, 90% and 99% are considered as features.

2.5.2 Gradient (Grad) based features

To calculate gradient features, the following steps are followed [78, 80].

i. The neighbourhood of an image pixel has to be considered. The neighbourhood of a pixel is as shown below.

ii. From this neighbourhood pixels, the absolute gradient value (AGV) is calculated for the pixel *x(i,j)*. AGV can be calculated either by considering 5×5 or 3×3 neighbourhood [29]. In the present work, the latter one is used. The formula used is,

$$AGV_3(i,j) = \sqrt{(R-H)^2 + (N-L)^2}$$

A	*B*	*C*	*D*	*E*
F	*G*	*H*	*I*	*J*
K	*L*	*x(i,j)*	*N*	*O*
P	*Q*	*R*	*S*	*T*
U	*V*	*W*	*Y*	*Z*

Figure 2.2: Neighbourhood of a pixel *x(i,j)*

iii. For the region of interest of size M×N, AGV is calculated at each pixel forming a two-dimensional array, may be termed as gradient image (GI) of size m×n.

iv. Five gradient features namely, Mean, Variance, Kurtosis, Skewness and percentage of pixels with non-zero gradient (PPNZG) are estimated. Formulas for these features are as follows

$$Grad\_Mean = \frac{1}{mn}\sum_{i=1}^{m}\sum_{j=1}^{n} GI(i,j)$$

$$Grad\_Variance = \frac{1}{mn-1}\sum_{i=1}^{m}\sum_{j=1}^{n}(GI(i,j) - Grad\_Mean)^2$$

$$Grad\_Skewness = \frac{1}{mn}\sum_{i=1}^{m}\sum_{j=1}^{n}\left(\frac{GI(i,j) - Grad\_Mean}{\sqrt{Grad\_Variance}}\right)^3$$

$$Grad\_Kurtosis = \frac{1}{mn}\sum_{i=1}^{m}\sum_{j=1}^{n}\left(\frac{I(i,j) - Grad\_Mean}{\sqrt{Grad\_Variance}}\right)^4$$

$$PPNZG = \frac{Number\ of\ non-zero\ pixels\ in\ GI}{Number\ of\ pixels\ in\ GI}$$

2.5.3 Moments Invariant (MI) features

Moments invariant are characteristics of closed region that are invariant of translation, rotation and scaling [81-83]. Moment invariants are simple mathematically calculated properties that are often used for classification, recognition applications. The traditional technique of generating invariants in terms of algebraic moments was proposed by Hu [84]. For an input image *f(x,y)*, the algebraic moments is given by

$$m_{pq} = \sum_{x}\sum_{y} x^p y^q f(x,y)$$

Often, moment invariants are represented in terms of normalized central moments, η_{pq} which is given by

$$\eta_{pq} = \frac{\mu_{pq}}{\mu_{00}^{\gamma}}$$

where,

$$\mu_{pq} = \sum_{x}\sum_{y}(x-\bar{x})^p(y-\bar{y})^q f(x,y)$$

$$\bar{x} = \frac{x_{10}}{x_{00}}$$

and

$$\bar{y} = \frac{x_{01}}{x_{00}}$$

$$\gamma = \frac{p+q}{2} + 1$$

for $p+q = 2,3,\ldots$.

μ_{pq} Central moments of order up to 3 are

$\mu_{00} = m_{00}, \mu_{10} = 0, \mu_{01} = 0, \mu_{11} = m_{11} - \bar{y}m_{10}, \mu_{20} = m_{20} - \bar{x}m_{10}, \mu_{02} = m_{02} - \bar{y}m_{01},$

$\mu_{30} = m_{30} - 3\bar{x}m_{20} + 2\bar{x}^2 m_{10}\,, \mu_{03} = m_{03} - 3\bar{y}m_{02} + 2\bar{y}^2 m_{01},$

$\mu_{21} = m_{21} - 2\bar{x}m_{11} - \bar{y}m_{20} + 2\bar{x}^2 m_{01}, \mu_{12} = m_{12} - 2\bar{y}m_{11} - \bar{x}m_{02} + 2\bar{y}^2 m_{10}$

A set of seven invariant moments can be derived from the second and third normalized central moments.

$$\emptyset_1 = \eta_{20} + \eta_{02}$$

$$\emptyset_2 = (\eta_{20} - \eta_{02})^2 + 4\eta_{11}^2$$

$$\emptyset_3 = (\eta_{30} - 3\eta_{12})^2 + (3\eta_{21} - \eta_{03})^2$$

$$\emptyset_4 = (\eta_{30} + \eta_{12})^2 + (\eta_{21} + \eta_{03})^2$$

$$\emptyset_5 = (\eta_{30} - 3\eta_{12})(\eta_{30} + \eta_{12})[(\eta_{30} + \eta_{12})^2 - 3(\eta_{21} + \eta_{03})^2] + (3\eta_{21} - \eta_{03})(\eta_{21} + \eta_{03})[3(\eta_{30} + \eta_{12})^2 - (\eta_{21} + \eta_{03})^2]$$

$$\emptyset_6 = (\eta_{20} - \eta_{02})[(\eta_{30} + \eta_{12})^2 - (\eta_{21} + \eta_{03})^2] + 4\eta_{11}(\eta_{30} + \eta_{12})(\eta_{21} + \eta_{03})$$

$$\emptyset_7 = (3\eta_{21} - \eta_{03})(\eta_{30} + \eta_{12})[(\eta_{30} + \eta_{12})^2 - 3(\eta_{21} + \eta_{03})^2] + (3\eta_{12} - \eta_{03})(\eta_{21} + \eta_{03})[3(\eta_{30} + \eta_{12})^2 - (\eta_{21} + \eta_{03})^2]$$

2.5.4 Gray-level co-occurrence matrix (GLCM) features

Gray-level co-occurrence matrix is a second-order statistical method. Hence, it considers the spatial relationship of pixels in the image. GLCM proposed by Haralick [85] is one of the most frequently used texture features. To understand the way GLCM is computed, consider a matrix of 5×5, an image *f(x, y)* in numerical representation, i.e. gray-levels are in numerical values.

0	0	1	3	1
3	1	1	3	1
3	1	3	0	3
3	2	1	0	3
3	3	2	1	2

Figure 2.3: An image *f(x, y)* with numerical representation of pixels

GLCM is defined based on two elements; inter pixel distance *d* and direction θ. If the centre pixel of above matrix is considered, whose value is 3, the pixel towards the right having value 0 is at $\theta = 0^o$ and $d = 1$. Similarly, w.r.t to this centre pixel, top-right pixel with value 3, top pixel with value 1 and top-left pixel with value 1 are at $d = 1$ and $\theta = 45^o$, $\theta = 90^o$ and $\theta = 135^o$ respectively. GLCM of the above matrix for $d = 1$ and $\theta = 0^o$ is computed as follows. First, note the number of gray-levels in the matrix are 4 i.e. 0, 1, 2, 3. The GLCM is as shown below. For i = 0, j = 0, number of times pixels having (0, 0) with $d = 1$ in 0^o orientation have occurred i.e. 1 is noted in GLCM. For i = 0, j = 3, number of times pixels having (0, 3) have occurred is 2, entered in GLCM. Similarly, GLCM is computed for i = 0, 1, 2, 3 and j = 0, 1, 2, 3. For above matrix of 5×5 image *f(x, y)*, GLCMs with varying *d* and θ can be computed. Normalized GLCMs are obtained by computing the sum of all the values in each GLCM (number of total gray-level transitions in the GLCM) and dividing each element by the sum.

j / i	0	1	2	3
0	1	1	0	2
1	1	1	1	3
2	0	3	0	0
3	1	3	2	1

Figure 2.4: GLCM matrix of *f(x, y)* for $d = 1$ and $\theta = 0^o$

The following notations are used to mathematically express the features extracted from GLCM.

$P(i, j)$ = $(i, j)^{th}$ element in normalized GLCM

$p_x(i)$ = i^{th} element in the marginal-probability matrix obtained summing the rows of $p(i, j)$

$p_y(i)$ = j^{th} element in the marginal-probability matrix obtained summing the rows of $p(i, j)$

The mean and standard deviations for the rows and columns of matrix are expressed as

$$\mu_x = \sum_{i=1}^{N_g}\sum_{j=1}^{N_g} i.p(i,j)$$

$$\mu_y = \sum_{i=1}^{N_g}\sum_{j=1}^{N_g} j.p(i,j)$$

$$\sigma_x = \sum_{i=1}^{N_g}\sum_{j=1}^{N_g} (i-\mu_x)^2.p(i,j)$$

$$\sigma_y = \sum_{i=1}^{N_g}\sum_{j=1}^{N_g} (j-\mu_y)^2.p(i,j)$$

where μ_x and μ_y are the mean of p_x and p_y respectively. σ_x and σ_y are the mean of p_x and p_y respectively. N_g represents number of gray levels.

Probabilities p_{x+y} and p_{x-y} that are related to specified intensity sums or differences, are defined as follows

$$p_{x+y}(k) = \sum_{i=1}^{N_g}\sum_{\substack{j=1 \\ i+j=k}}^{N_g} p(i,j) \quad k = 2,3,\dots 2N_g$$

$$p_{x-y}(k) = \sum_{i=1}^{N_g}\sum_{\substack{j=1 \\ |i-j|=k}}^{N_g} p(i,j) \quad k = 0,1,\dots N_g - 1$$

Twenty one GLCM features [86-89] used in present work are defined as follows.

$$Energy = \sum_{i=1}^{N_g}\sum_{j=1}^{N_g} \{p(i,j)\}^2$$

$$Entropy = -\sum_{i=0}^{N_g-1}\sum_{j=0}^{N_g-1} p(i,j)\log(p(i,j))$$

$$Dissimilarity = \sum_{i=1}^{N_g}\sum_{j=1}^{N_g} |i-j|\, p(i,j)$$

$$Contrast = \sum_{n=0}^{N_g-1} n^2 \left\{ \sum_{i=1}^{N_g} \sum_{\substack{j=1 \\ |i-j|=n}}^{N_g} p(i,j) \right\}$$

$$Inverse\ difference = \sum_{i=0}^{N_g-1} \sum_{j=0}^{N_g-1} \frac{1}{1+|i-j|} p(i,j)$$

$$Correlation = \sum_{i=0}^{N_g-1} \sum_{j=0}^{N_g-1} \frac{(i-\mu_x)(j-\mu_y)p(i,j)}{\sigma_x \sigma_y}$$

$$Inverse\ difference\ moment/Homogeneity = \sum_{i=0}^{N_g-1} \sum_{j=0}^{N_g-1} \frac{1}{1+(i-j)^2} p(i,j)$$

$$Autocorrelation = \sum_{i=1}^{N_g} \sum_{j=1}^{N_g} (ij)p(i,j)$$

$$Cluster\ Shade = \sum_{i=1}^{N_g} \sum_{j=1}^{N_g} (i-\mu_x+j-\mu_y)^3 p(i,j)$$

$$Cluster\ Prominence = \sum_{i=1}^{N_g} \sum_{j=1}^{N_g} (i-\mu_x+j-\mu_y)^4 p(i,j)$$

$$Maximum\ Probability = \max(p(i,j))$$

$$Sum\ of\ Squares/Variance = \sum_{i=1}^{N_g} \sum_{j=1}^{N_g} (i-\mu)^2\ p(i,j)$$

$$Sum\ Average = \sum_{i=2}^{2N_g} i p_{x+y}(i)$$

$$Sum\ Variance = \sum_{i=2}^{2N_g} (i - Sum\ Entropy)^2 p_{x+y}(i)$$

$$Sum\ Entropy = -\sum_{i=2}^{2N_g} p_{x+y}(i) log\{p_{x+y}(i)\}$$

$$Difference\ Variance = Variance\ of\ p_{x-y}$$

$$Difference\ Entropy = -\sum_{i=0}^{N_g-1} p_{x-y}(i) log\{p_{x-y}(i)\}$$

$Information\ Measure\ of\ Correlation\ (IMC)$

$$IMC1 = \frac{HXY - HXY1}{max\{HX, HY\}}$$

$$IMC2 = (1 - \exp[-2.0(HXY2 - HXY)])^{1/2}$$

$$HXY = -\sum_i \sum_j p(i,j)\log(p(i,j))$$

where *HX* and *HY* are entropies of p_x and p_y

$$HXY1 = -\sum_i \sum_j p(i,j)\log\{p_x(i)p_y(j)\}$$

$$HXY2 = -\sum_i \sum_j p_x(i)p_y(j)\log\{p_x(i)p_y(j)\}$$

$$Maximum\ Correlation\ Coefficient = (Second\ largest\ eigenvalue\ of\ Q)^{1/2}$$

where

$$Q(i,j) = \sum_k \frac{p(i,k)p(j,k)}{p_x(i)p_y(k)}$$

$$Inverse\ Difference\ Normalized = \sum_{i=1}^{N_g} \sum_{j=1}^{N_g} \frac{1}{1 + (|i-j|/N)} p(i,j)$$

$$Inverse\ Difference\ Moment\ Normalized = \sum_{i=1}^{N_g} \sum_{j=1}^{N_g} \frac{1}{1 + (|i-j|/N)^2} p(i,j)$$

GLCM features defined above, Energy, Entropy, Dissimilarity, Contrast, Inverse difference, Correlation, Homogeneity, Autocorrelation, Cluster shade, Cluster prominence, Maximum probability, Sum of squares, Sum average, Sum variance, Sum entropy, Difference variance, Difference entropy, Information measures of correlation, Maximum correlation coefficient, Inverse difference normalized and Inverse difference moment normalized [5, 14, 18] along 4 orientations (0^o, 45^o, 90^o and 135^o) for 5 values of inter pixel distance i.e., d=1, 2, 3, 4 and 5 results in a feature set of 420 features.

2.5.5 Run-length matrix (RLM) features

Galloway [90] proposed the Gray level run length matrix method for extracting texture features from the images. The run length is the number of consecutive pixels in the run and the value gives the number of times such a run occurs in the image. Gray level run length matrix is a set of values that are the number of times consecutive and collinear pixels having same gray level in the image. It represents the coarseness of the texture in the image in a particular

orientation. The example below describes the construction of gray level run length matrix. An image of size 6×6 represented with pixel values is shown below.

1	1	2	2	1	1
3	3	1	1	2	2
1	1	2	3	1	1
3	1	2	2	1	1
1	1	3	2	2	2
2	3	1	1	2	2

Figure 2.5: An image *g(x, y)* with gray level values of pixels

The gray level run length matrix of *g(x, y)* for $\theta = 0^o$ is shown in Figure. From the image, for consecutive pixels of length 2 having gray level value 1 occurred 8 times. Hence (*i*=1, *j*=2) in Figure, the value is 8. Similarly, for consecutive pixels of length 1 having gray level value 3 occurred 4 times and hence (*i*=3, *j*=1) is 4.

Gray level *i*	Run length *j*		
	1	2	3
1	1	8	0
2	2	4	1
3	4	1	0

Figure 2.6: Gray level run length matrix of *g(x,y)* for $\theta = 0^o$

In the same way matrix can be constructed for $\theta = 45^o$, 90^o, and 135^o. From each of these matrices, eleven features i.e., Short run emphasis (SRE), Long run emphasis (LRE), Gray-level non-uniformity (GLN), Run-length non-uniformity (RLN), Run percentage (RP), Low gray-level run emphasis (LGRE), High gray-level rum emphasis (HGRE), Short run low gray-level emphasis (SRLGE), Short run high gray-level emphasis (SRHGE), Long run low gray-level emphasis (LRLGE) and Long run high gray-level emphasis (LRHGE) [30, 91] can be computed. Eleven RLM features considered along 4 orientations (0^o, 45^o, 90^o and 135^o), results in a set of 44 RLM features. They are defined as below.

$$SRE = \frac{1}{n_r}\sum_{i=1}^{M}\sum_{j=1}^{N}\frac{P(i,j)}{j^2}$$

$$LRE = \frac{1}{n_r}\sum_{i=1}^{M}\sum_{j=1}^{N} P(i,j).j^2$$

$$GLN = \frac{1}{n_r}\sum_{i=1}^{M}\left(\sum_{j=1}^{N} P(i,j)\right)^2$$

$$RLN = \frac{1}{n_r}\sum_{j=1}^{N}\left(\sum_{i=1}^{M} P(i,j)\right)^2$$

$$RP = \frac{n_r}{n_p}$$

$$LGRE = \frac{1}{n_r}\sum_{i=1}^{M}\sum_{j=1}^{N} \frac{P(i,j)}{i^2}$$

$$HGRE = \frac{1}{n_r}\sum_{i=1}^{M}\sum_{j=1}^{N} P(i,j).i^2$$

$$SRLGE = \frac{1}{n_r}\sum_{i=1}^{M}\sum_{j=1}^{N} \frac{P(i,j)}{i^2.j^2}$$

$$SRHGE = \frac{1}{n_r}\sum_{i=1}^{M}\sum_{j=1}^{N} \frac{P(i,j).i^2}{j^2}$$

$$LRLGE = \frac{1}{n_r}\sum_{i=1}^{M}\sum_{j=1}^{N} \frac{P(i,j).j^2}{i^2}$$

$$LRHGE = \frac{1}{n_r}\sum_{i=1}^{M}\sum_{j=1}^{N} P(i,j).i^2.j^2$$

where *P(i, j)* is (i, j)th entry in gray level run length matrix, n_r is the total number of runs and n_p is the total number of pixels in the image *g(x, y)*.

2.5.6 Laws texture energy (Laws) features

The spatial filters proposed by Laws [92] are applied to the images in order to get their filtered counterpart. The texture features are computed from the filtered images. The kernels are

designed in such a way which will help in extracting different local property. The initial three 1D kernel connected with underlying microstructures are:

Gaussian (Local averaging) L3 = [1 2 1]

Edge detector (First difference) E3 = [-1 0 1]

Laplacian (Second difference) S3 = [-1 2 -1]

L, E and S represent Level, Edge and Spot detector respectively. The number followed by them represents length of the kernel. 1D kernels of length 5 can be generated by convolving pairs of above kernels. Out of nine pairs, five pairs which are used often are:

Level detector L5 = L3*L3 = [1 4 6 4 1]

Edge detector E5 = L3*E3 = [-1 -2 0 2 1]

Spot detector S5 = L3*S3 = [-1 0 2 0 -1]

Wave detector W5 = E3*S3 = [-1 2 0 -2 1]

Ripple detector R5 = S3*S3 = [1 -4 6 -4 1]

2D kernels of size 5×5 are generated by convolving vertical and horizontal 1D kernels. 25 2D kernels obtained from above five kernels are:

L5L5	E5L5	S5L5	W5L5	R5L5
L5E5	E5E5	S5E5	W5E5	R5E5
L5S5	E5S5	S5S5	W5S5	R5S5
L5W5	E5W5	S5W5	W5W5	R5W5
L5R5	E5R5	S5R5	W5R5	R5R5

Kernels of different sizes such as 3×3, 5×5, 7×7 and 9×9 which represents different resolutions can be used. For extracting texture energy features, kernel of size 5×5 is used often in literature [29, 91]. Thus, in present work, 5×5 kernels have been used. Each of the filtered images (FI) is further processed by texture energy measurement (TEM) filter, which is a moving average non-linear filter. Laws proposed to use window size of 15×15 for its optimality in terms of classification accuracy and computational cost.

$$I_{TEM}(x,y) = \sum_{i=-7}^{7} \sum_{j=-7}^{7} |FI(x+i, y+j)|$$

From above 25 kernels, TEM images obtained from FI of diagonally opposite kernels such as L5E5 and E5L5, etc. are averaged to obtain totally 15 rotational invariant images. Ten first order

statistics features (see Section 2.5.1) from 15 rotational invariance images (give 150 features in total) have been used in the present work.

2.6 Differential Evolution Feature Selection (DEFS)

Feature selection is an essential step towards efficient performance of a classifier as it excludes irrelevant and redundant features while forming a subset. Thereby, it also reduces calculations and time of processing. Differential evolution (DE) has its advantages over other population based strategy in optimality and convergence speed. The algorithm of DEFS is as follows:

Step 1: Initial points are chosen randomly to form initial population of size *NP* × *DNF*, where *NP* are randomly chosen initial vectors, x_i, $i = 0, 1, 2, \ldots, NP\text{-}1$ and *DNF* are desired number of features.

Step 2: Mutant population is generated by adding a vector to the scaled version of difference of two vectors which are chosen randomly.

$$v_{j,i,g} = x_{j,r0,g} + F.(x_{j,r1,g} - x_{j,r2,g})$$

where x_{r0}, x_{r1} and x_{r2} are randomly chosen vectors, *v* is the mutant vector and *F* is a scale factor that controls the rate at which the population evolves. *I* is the population index runs from 0 to *NP*-1, *j* is the feature index runs from 0 to *DNF*-1 and g represents generation or iteration of algorithm which runs from 1 to GEN (number of generations/iterations). In DEFS, *F* changes dynamically as follows:

$$F = \frac{c_1 \times rand}{\max(x_{j,r1,g}, x_{j,r2,g})}$$

where c_1 is a constant smaller than 1.

Step 3: A trail vector is generated by crossover between mutant vector and the population vector of the same index.

$$u_{j,i,g} = \begin{cases} v_{j,i,g} \; if \; rand(0,1) \leq C_r \\ x_{j,i,g} \qquad\qquad otherwise \end{cases}$$

where u is the trial vector and C_r is the crossover probability that controls the fraction of parameter values that are copied from the mutant vector.

Step 4: Trail vector competes with the population vector of same index. One with lower classification error rate is selected in the population matrix. Since, DEFS depends on feedback

from a classifier in selecting optimum feature subsets, it is a wrapper method. In the present work, k-NN classifier has been used for obtaining classification error rates.

Step 5: Procedure repeats until each of the vectors in the population matrix have competed with a trial vector.

Step 6: Vectors selected out of these competitions form the population matrix for the next iteration.

Step 7: Algorithm stops with the predefined number of iterations completion.

Rami khushaba, et.al., modified DE and utilized roulette wheel supplied with probabilities of relevant features distribution for feature selection [64].

Optimization of parameters: In the present work, for obtaining optimal values to the parameters of feature selection such as desired number of features, population size and the number of iterations, an optimization study has been performed. A 3-D matrix has been formed with population size of 25, 50, 75 and 100, number of iterations of 25, 50, 75 and 100 and desired number of features of 5, 10, 20, 30,…,100. For each position of this matrix, DEFS procedure is executed 30 times to obtain 30 subsets. Average accuracy and standard deviation of these 30 subsets are tabulated. The average time taken to generate a subset is also noted down. This matrix revealed that, for desired number of features equal to 10, population size 50, and the number of iterations equal to 100 are optimal as for overall classification accuracy and computational time is concerned. Hence, these values are utilized in the DEFS procedure.

2.7 Classification

Given a sample, the task of the classifier is to assign it to the correct class. After extracting and selecting appropriate features which represent the classes, the classifier has training and testing phases to go through. For a classification task which involves *d* features, at least ten times of *d* features samples per class for training are required to get reliable statistical measures [93]. This is not practical due to constraints on availability of data which is termed as curse of dimensionality. Support vector machine (SVM) is an appropriate choice for image classification as it is less sensitive to curse of dimensionality. SVM is known for its potential to yield higher accuracy with less number of training samples and comparatively more number of features. SVM classifier separates the classes with minimal error by building optimized hyper plane in the feature space of higher dimensions. It maximizes the margin between the classes under consideration thereby exhibits robustness to the overfitting problem.

Basically, SVM is a binary classifier. The real life applications requirement is mostly of multi-class classification. There are many approaches as to how to perform multi-class classification using binary classifier[94]. One-against-all [95], one-against-one [96], all-and-one [97], direct acyclic graph SVM [98], hierarchical tree structure based methods [48, 99, 100], error correcting output codes [101-103] are a few to mention. From literature[104, 105], it is found that one-against-one multi-class SVM classifier performs better and hence has been used for the present classification task. SVM classifier has also been extensively used for the classification [106] of medical images [9, 10, 16, 107-115].

To ensure generality and robustness for the classifier designs, two sets of images each consisting of representative images from each image classes are created. To avoid any biasing, the ROIs from one image set are used for training and the ROIs from the other image set are used for testing [116]. In the present work, non-linear data mapping from input space to feature space has been performed by using Gaussian radial basis kernel. Min-Max method of normalization has been used to rescale the feature values between 0 and 1 [117, 118]. One-against-one multiclass SVM classifier has been implemented in MATLAB. The SVM kernel parameter γ tunes the curvature of the decision boundary and the soft margin constant C increase the margin with minimum error possible. From the parameter space such as $\gamma \epsilon \{2^{-5}, 2^{-4},\ldots, 2^{5}\}$ and $C \epsilon \{2^{-5}, 2^{-4},\ldots, 2^{5}\}$, the optimal values are obtained by grid search method to train the SVM using 10-fold cross-validation on training data.

Performance Measures: Confusion matrix is the basic structure which presents classification results in tabular form. It tabulates predicted results versus known ground truth classes as reference. A generalized confusion matrix for a binary classification system is as depicted below.

Confusion matrix of a binary classification system		Predicted Class	
		Positive	Negative
Known Class	Positive	True Positive (TP)	False Negative (FN)
	Negative	False Positive (FP)	True Negative (TN)

Various measures are estimated from the confusion matrix to evaluate the performance of a classification system. The most simplified and often considered measured is accuracy. When there are unbalanced data samples among various classes under consideration, accuracy alone is not a reliable measure for evaluation. The frequently estimated parameters are sensitivity and

specificity [119, 120]. Accuracy for multi-class classification system would be estimated in terms of individual class accuracy or/and overall classification accuracy.

$$Accuracy = \frac{TP+TN}{TP+FN+FP+TN} \qquad Sensitivity = \frac{TP}{TP+FN} \qquad Specificity = \frac{TN}{TN+FP}$$

2.8 Concluding remarks

In this chapter, the ethical issues and protocols followed during image acquisition are briefed, which is the initial aspect of the present work. The order in which each component of CAC system exists, details of those components with the methods, algorithms and various parameter values used are discussed in detail. The components such as ROI selection, texture feature extraction, feature selection and classification which are common in all four proposed CAC systems are presented here. Further details which are specific to each CAC systems have been presented in respective chapters. In next chapter, first CAC system of part 1 i.e. of kidney images is described.

Chapter 3

SVM based CAC system for B-mode kidney ultrasound images

3.1 Introduction

Kidney is a bean-shaped soft tissue organ and has a vital role to play in urinary system. Nephrons are the functional unit of kidney and the region where it is spread in kidney are termed as parenchyma. The parenchyma is divided to form the outer renal cortex and inner renal medulla. Renal medulla consists of cone-shaped tissues called pyramids and the projections of renal cortex in between the pyramids are known as renal columns [43].

The normal kidney has cortex, hypoechoic than liver and the demarcation between cortex and medulla is possible. There are disorders like hematuria, proteinuria, pyuria, polyuria, etc. which may involve partly or completely diseased nephrons. Sometimes, those diseases are not diagnosable exactly by the radiologists and are termed as medical renal disease. In MRD, parenchyma is hyper-echoic than normal and the demarcation between cortex and medulla becomes hardly possible [5]. Cysts are regions which appears anechoic because of the fluid filled in them. They are regions with thin wall and also exhibit posterior wall enhancement.

Bommanna Raja, et.al., have studied the classification of above mentioned classes by extracting kidney region [43] and using different features [5]. In their study, the whole kidney area has been considered for extracting features. Whereas, the radiologist opined that the characteristic changes in MRD with respect to normal is in parenchyma of kidney and the cysts are focal in nature. Therefore, in the present work ROIs are obtained from parenchyma region of kidney in case of normal and MRD classes and from within lesion in case of cyst class.

Speckle noise in B-mode ultrasound images makes visual diagnosis a difficult task, but it also contain diagnostic information which is preferred by the radiologists. Various de-speckling methods have been proposed in literature [121]. From the studies [52, 54], it has been noted that the de-speckling methods can be oriented towards improving either texture classification or segmentation. Hence, in the present work, few standard de-speckling methods have been utilized before feature extraction to evaluate the contribution of these methods towards improving the performance of classification [122].

3.2 Dataset Description

In the present work, data set consisting of 35 B-mode ultrasound kidney images i.e., 11 normal, 8 MRD and 16 cyst images are used. These direct digital images are recorded from 35 patients. Either left or right kidney from longitudinal plane is considered. As advised by experienced radiologist that the distinguishing characteristics of MRD and normal are prominent in parenchyma region of kidney, ROIs are obtained from parenchyma region in case of these. In case of cysts, ROIs within lesions are selected. The data consisted of 49 normal ROIs from 11 normal images, 62 MRD ROIs from 8 MRD images and 62 cyst ROIs from 16 cyst images. The bifurcation of data set into training dataset and testing dataset is shown in Figure 3.1.

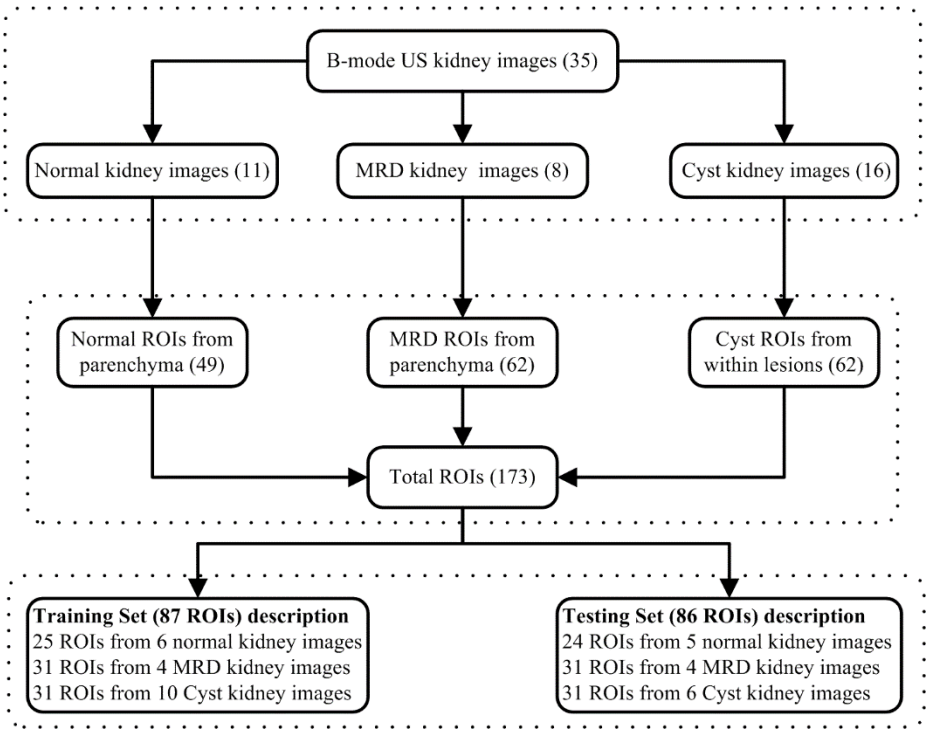

Figure 3.1: Dataset Distribution

3.3 Experimental Results

The block diagram representation indicating workflow of the present work is as illustrated in Figure 3.2.

Three experiments are conducted with two cases in each i.e., without feature selection (C1) and with feature selection (C2). In experiment 1 (E1), ROIs are marked and extracted from original (without de-speckling) US images followed by feature extraction. E1C1 represents features from experiment 1 without feature selection, similarly E1C2, represents features from experiment 1 with feature selection. These features are used for designing separate SVM classifiers.

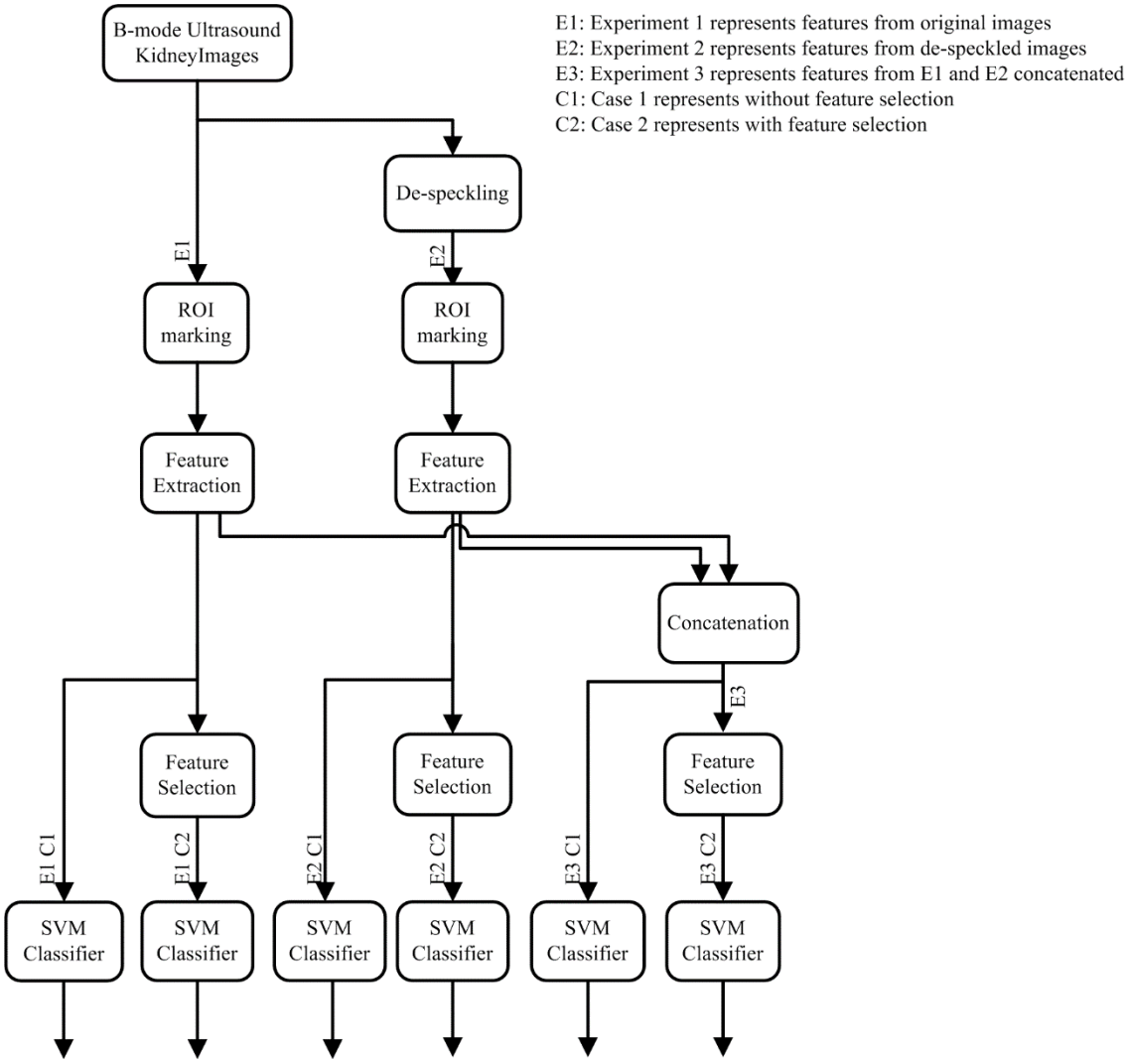

Figure 3.2: Block diagram of CAC system for kidney ultrasound images

Experiment 2 starts with de-speckling the US images, ROIs are extracted from the same locations (markings) which are saved in experiment 1. This is followed by feature extraction. E2C1 and E2C2 represent features from experiment 2 without and with feature selection respectively. Again, classification is carried out by different SVM classifiers. In experiment 3, features from E1 and E2 are concatenated forming larger feature set. E2 has features from ROIs of images de-speckled by eight methods, giving rise to that many features sets. The combinations considered for concatenation are mentioned in the subsection Experiment 3. E3C1 represents concatenated features set, is passed through SVM classifier. E3C2 represents concatenated features from experiment 3 after feature selection and is passed through SVM classifier which is shown separately.

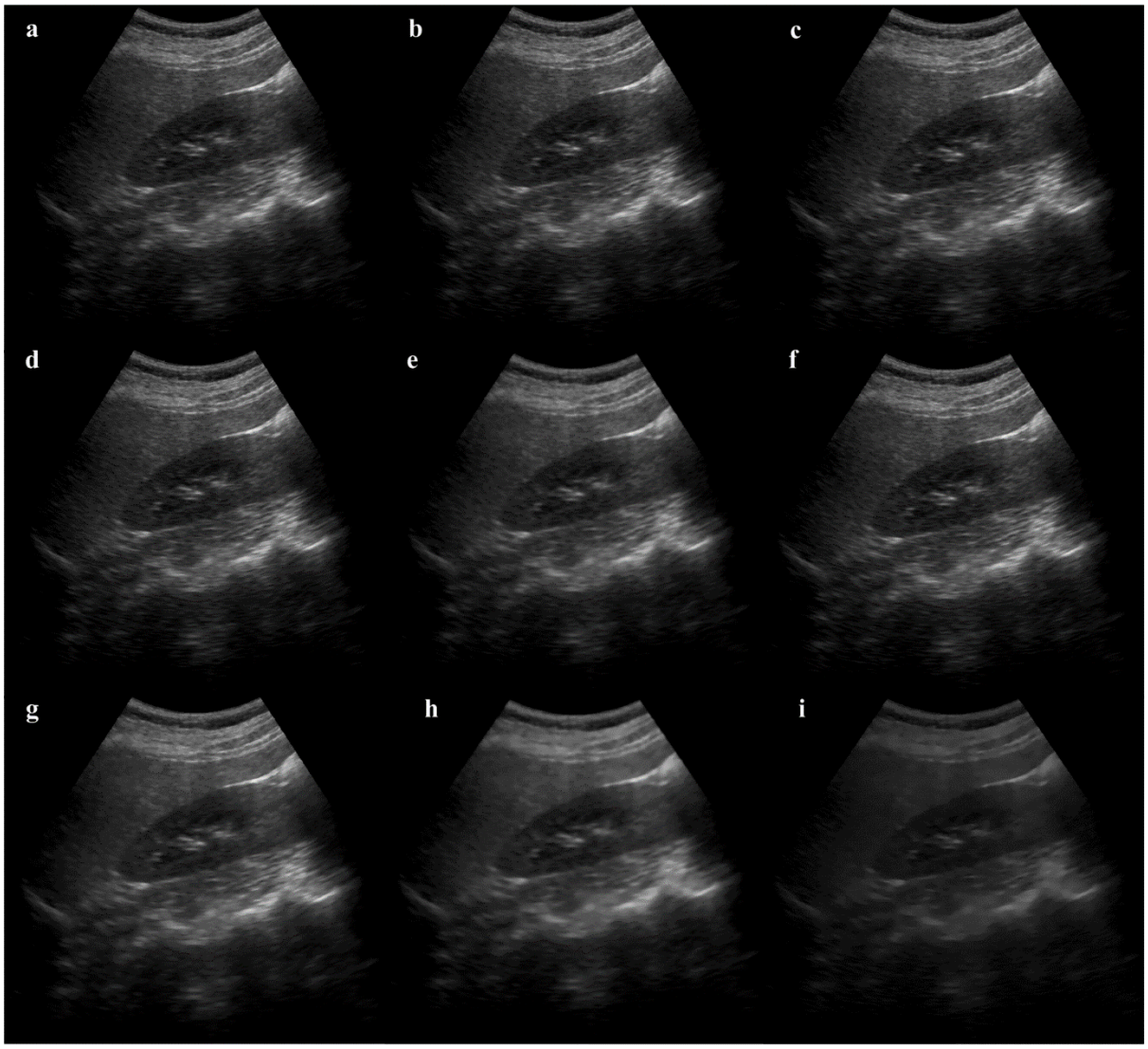

Figure 3.3: Sample of a original and de-speckled images of kidney (a) Original (b) Lee (c) Lee's sigma (d) enhanced Lee I Frost (f) Kaun (g) Geometric (h) SRAD (i) DPAD

A sample of an original kidney image and corresponding de-speckled images are shown in Figure 3.3. The de-speckling filter parameters and their values used in the present work are tabulated in Table 3.1. The qualitative opinion of radiologist is that, relatively the images de-speckled by Lee's sigma, enhanced Lee, Frost and Kaun filter outputs are reliable and that of Lee, geometric filters, SRAD and DPAD filters are not. The parameters which are frequently used for accessing the potentiality of de-speckling methods quantitatively such as beta (β), correlation coefficient (CC), edge region mean square error (eMSE), root mean square error (RMSE), structural similarity (SSIM) index, peak signal-to-noise ratio (PSNR), figure of merit (FOM), image quality index (IMQI) are computed. The average (standard deviation) of the parameter values are tabulated in Table 3.2. The β values indicate Lee's sigma filter 0.95(0.007) is better, whereas CC, eMSE, RMSE and PSNR point geometric filter to be best with their values

Table 3.1: De-speckling filters parameters

Method	Abbreviation	Filter Parameters
Lee filter [123]	Lee	z=5
Lee's sigma filter [124]	Slee	z=5
Enhanced Lee filter [47]	EnLee	z=5
Frost filter [125]	Frost	z=5
Kaun filter [126]	Kaun	z=5
Geometric filter [49]	Geo	n=3
Speckle reducing anisotropic diffusion [51]	SRAD	s = 0.2, n = 100, z=5
Detail preserving anisotropic diffusion [50]	DPAD	s = 0.2, n = 100, z=5

Note: z: mask size; n: number of iterations; s: step size

Table 3.2: Performance measures of de-speckling filters.

De-speckling filters	B	CC	eMSE	RMSE	SSIM	PSNR	FOM	IMQI
Lee	0.93(0.05)	0.94(0.009)	13.03(1.8)	3.6(0.2)	0.96(0.008)	27.7(0.5)	0.96(0.01)	0.96(0.001)
Lee's sigma	0.95(0.007)	0.94(0.009)	12.3(0.4)	3.5(0.06)	0.96(0.002)	27.9(0.5)	0.97(0.01)	0.96(0.001)
Enhanced Lee	0.21(0.01)	0.95(0.008)	23.5(4.5)	4.8(0.4)	0.68(0.004)	18.5(0.4)	0.79(0.02)	0.89(0.04)
Frost	0.63(0.03)	0.92(0.01)	22.4(1.6)	4.7(0.1)	0.93(0.006)	24.6(0.6)	0.93(0.01)	0.92(0.01)
Kaun	0.93(0.04)	0.94(0.009)	13.02(1.8)	3.6(0.2)	0.96(0.008)	27.7(0.5)	0.96(0.01)	0.96(0.001)
Geometric	0.87(0.02)	0.99(0.001)	1.8(0.2)	1.3(0.08)	0.96(0.003)	37.6(0.8)	0.86(0.04)	0.69(0.07)
SRAD	0.24(0.02)	0.94(0.007)	8.3(2.3)	2.8(0.3)	0.79(0.02)	21.7(0.5)	0.47(0.04)	0.88(0.06)
DPAD	0.32(0.01)	0.7(0.04)	11(5.1)	3.2(0.7)	0.16(0.03)	10.3(1.0)	0.57(0.06)	0.29(0.06)

0.99(0.001), 1.8(0.2), 1.3(0.08) and 37.6(0.8) respectively. SSIM indicates the performance of Lee 0.96(0.008), Kaun 0.96(0.008), geometric 0.96(0.003) are more or less same with Lee's sigma 0.96(0.002) being better. According to FOM, Lee's sigma 0.97(0.01) is better. IMQI shows better performance 0.96(0.001) for Lee, Lee's sigma and Kaun filters. These parameters are computed to find the possible correlation with the classification results from the features of de-speckled images.

The classification results without feature selection are tabulated in Table 3.3. For feature selection, DEFS process is repeated 30 times to obtain 30 subsets [16] and the subset with best classification result has been shown in Table 3.4. Average accuracy and standard deviation values of 30 subsets are shown in Table 3.5.

*In Table 3.3, 3.4 and 3.5, the second column i.e., Features/De-speckle/Set represents features from a particular feature's category of which the name is mentioned. Similarly for features from De-speckling method and sets (sets are defined in subsection experiment 3). The feature category 'All' represents features from all categories concatenated together and 'Grad + RLM' indicates that features from those two categories are concatenated.

Combinatorial representations like 'All Enhanced Lee' denote features from all categories extracted from the ROIs of images de-speckled by Enhanced Lee method. 'All set 1-4' means 'All set 1', 'All set 2', 'All set 3' and 'All set 4'.

Experiment 1 (E1): Features from all texture features' categories are extracted from the ROIs of original B-mode kidney ultrasound images.

Case 1 (C1): Results obtained for individual and all features together without feature selection.

Table 3.3 (refer E1C1) shows that, the overall classification accuracy (OCA) obtained from All features is 81.3%. Among individual feature categories, gradient (5 features) has performed well with 86% OCA value.

When best two feature categories (gradient-86% and RLM-82.5%) are concatenated, it gave an OCA of 89.5% showing an increase in the performance without feature selection.

Case 2 (C2): Feature categories having more than 10 features (i.e., RLM, GLCM, Laws, All, Grad + RLM) are subjected to feature selection before classification.

Table 3.3: Classification results without feature selection

Experiment-Case Number	Features/ De-speckle/ Set*	Accuracy (%)			Sensitivity (%)			Specificity (%)			Overall accuracy (%)
		Cyst	MRD	Normal	Cyst	MRD	Normal	Cyst	MRD	Normal	
E1C1	All	93	86	83.7	96.7	87	54.1	90.9	85.4	95.1	**81.3**
	FOS	100	77	77.9	100	77.4	50	100	78.1	88.7	77.9
	Grad	98.8	86	87.2	96	80.6	79.1	100	89	90.3	**86**
	MI	95.3	75.5	70.9	87	80	37.5	100	72.7	83.8	70.9
	RLM	93	87.2	84.8	93.5	80.5	70.8	92.7	90.9	90.3	82.5
	GLCM	93	82.5	82	90.3	83.8	58.3	94.5	81.8	91.9	79
	Laws	96.5	82	79	97	77	58	96.3	85	87	79
	Grad+RLM	97.6	90.6	90	93.4	83.9	91.6	100	94.4	90.2	**89.5**
E2C1	All Lee	95.3	82.5	80.2	96.7	87.1	45.8	94.5	80	93.5	79
	All Lee's sigma	93	86	83.7	96.7	87.1	54.1	90.9	85.5	95.1	**81.3**
	All Enhanced Lee	98.8	82.5	83.7	96.7	83.8	62.5	100	81.8	91.9	**82.5**
	All Frost	90.6	82.5	84.8	96.7	80.6	54.1	87.2	83.6	96.7	79
	All Kaun	95.3	83.7	81.3	96.7	90.3	45.8	94.5	80	95.1	80.2
	All Geometric	89.5	82.5	81.3	90.3	90.3	41.6	89	78.1	96.7	76.7
	All SRAD	90.6	75.5	73.2	100	64.5	37.5	85.4	81.8	87	69.7
	All DPAD	97.6	80.2	80.2	100	77.4	54.1	96.3	81.8	90.3	79
	Grad+RLM Enhanced Lee	98.8	90.6	91.8	96.7	83.8	91.6	100	94.5	91.9	**90.6**

Note: * Please refer result section for the description of representations used in second column

Table 3.4: Best classification results with feature selection

Experiment-Case Number	Features/ De-speckle/ Set*	Accuracy (%)			Sensitivity (%)			Specificity (%)			Overall accuracy (%)
		Cyst	MRD	Normal	Cyst	MRD	Normal	Cyst	MRD	Normal	
E1C2	All	96	90.7	91.8	93	90.3	83.3	98.1	90.9	95.2	89.5
	RLM	97.7	89	87.1	96.8	80.7	83.2	98	94.5	88.6	88.3
	GLCM	94.1	87	90.7	87.1	83.7	87.5	98.2	94.6	88.7	86
	Laws	100	90.7	90.6	100	87.1	83.3	100	92.7	93.5	**90.6**
	Grad+RLM	97.6	91.8	89.5	93.5	87	87.5	100	94.5	90.3	**89.5**
E2C2	Grad+RLM Enhanced Lee	100	90.6	90.6	100	77.4	95.8	100	98.1	88.7	**90.6**
	All Lee's sigma	100	90.6	90.6	100	83.8	87.5	100	94.5	91.9	**90.6**
	All Enhanced Lee	100	90.6	90.6	100	80.6	91.6	100	96.3	90.3	**90.6**
E3C2	RLM set 1	97.6	88.3	88.3	96.7	77.4	87.5	98.1	94.5	88.7	87.2
	RLM set 2	98.8	89.5	90.6	96.7	83.8	87.5	100	92.7	91.9	89.5
	RLM set 3	98.8	90.6	91.6	96.7	87.1	87.5	100	92.7	93.5	**90.6**
	RLM set 4	98.8	90.6	91.8	96.7	77.4	100	100	98.1	88.7	**90.6**
	GLCM set 1	97.6	86	88.3	93.5	80.6	83.3	100	89	90.3	86
	GLCM set 2	95.3	91.8	91.8	93.5	87	87.5	96.3	94.5	93.5	**89.5**
	GLCM set 3	96.5	90.6	91.8	90.3	90.3	87.5	100	90.9	93.5	**89.5**
	GLCM set 4	94.1	89.5	90.6	83.8	83.8	95.8	100	92.7	88.7	87.2
	Laws set 1	100	88.3	88.3	100	90.3	70.8	100	87.2	95.1	88.3
	Laws set 2	100	91.8	91.8	100	93.5	79.1	100	90.9	96.7	91.8
	Laws set 3	100	94.1	94.1	100	90.3	91.6	100	96.3	95.1	**94.1**
	Laws set 4	97.6	90.6	93.3	96.7	93.5	79.1	98.1	89	98.3	90.6
	Grad+RLM set 1	97.6	87.2	87.2	93.5	77.4	87.5	100	92.7	87	86
	Grad+RLM set 2	100	91.8	91.8	100	80.6	95.8	100	98.1	90.3	**91.8**
	Grad+RLM set 3	97.6	89.5	91.8	93.5	80.6	95.8	100	94.5	90.3	89.5
	Grad+RLM set 4	96.5	91.8	93	93.5	83.8	95.8	98.1	96.3	91.9	90.6
	All set 1-4	100	100	100	100	100	100	100	100	100	**100**

Note: * Please refer result section for the description of representations used in second column

Table 3.5: Classification results from 30 subsets

Experiment-Case Number	Features/ De-speckle/ Set*	Average accuracy (%) (standard deviation)
E1C2	All	84.0(3.4)
	RLM	**84.0(1.7)**
	GLCM	82.4(3.1)
	Laws	83.1(3.7)
	Grad+RLM	84.7(2.4)
E2C2	Grad+RLM Enhanced Lee	**86.4(2.5)**
	All Lee's sigma	84.5(3.4)
	All Enhanced Lee	84.7(3.0)
E3C2	RLM set 1	83.5(1.5)
	RLM set 2	**86.3(1.6)**
	RLM set 3	86.2(2.7)
	RLM set 4	84.6(2.9)
	GLCM set 1	82.2(2.2)
	GLCM set 2	**85.3(3.0)**
	GLCM set 3	84.2(2.7)
	GLCM set 4	83.6(2.7)
	Laws set 1	**84.0(2.6)**
	Laws set 2	82.4(4.1)
	Laws set 3	82.2(3.8)
	Laws set 4	82.8(4.1)
	Grad+RLM set 1	83.9(1.4)
	Grad+RLM set 2	**86.2(1.6)**
	Grad+RLM set 3	86.2(2.2)
	Grad+RLM set 4	85.9(2.2)
	All set 1	85.8(5.4)
	All set 2	84.7(5.0)
	All set 3	**84.9(3.4)**
	All set 4	86.7(5.9)

Note: * Please refer result section for the description of representations used in second column

With feature selection (refer Table 3.4, E1C2), the performance of All features increased from 81.3% to 89.5% OCA, RLM features increased from 82.5% to 88.3% OCA and that of GLCM features increased from 79% to 86% OCA. Laws' features out performed with an OCA of 90.6%. These results show the significance of feature selection and Laws features.

Experiment 2 (E2): Texture features are extracted from the ROIs of de-speckled ultrasound images.

Case 1 (C1): Classification results are obtained for ROIs of images de-speckled by different methods, considering all the features (refer Table 3.3, E2C1). Lee's sigma features resulted in an OCA of 81.3% same as that of original images and enhanced Lee filter features has shown an increase in an OCA of 82.5%. Hence these two are considered for case 2 study.

Case 2 (C2): Subsets obtained from feature selection by considering all features in case of Lee's sigma have increased performance from 81.3% to 90.6% OCA and that of enhanced Lee filter is from 82.5% to 90.6% OCA. Concatenation of gradient and RLM features from enhanced Lee filter also gave an OCA of 90.6% (refer Table 3.4, E2C2).

Experiment 3 (E3): Here, all features of ROIs from original image, images de-speckled by Lee's sigma and enhanced Lee filter are concatenated to form 4 sets.

Set 1: Original image features and Lee's sigma filter features are concatenated.

Set 2: Lee's sigma filter features and enhanced Lee filter features are concatenated.

Set 3: Original image features and enhanced Lee filter features are concatenated.

Set 4: Original images features, Lee's sigma filter features and enhanced Lee filter features are concatenated.

From Table 3.4, comparing the results of experiment 1 (E1C2) and experiment 3 (E3C2), RLM features have an increased OCA from 88.3% to 90.6% (both set 3 and set 4). GLCM features have shown better improvement in OCA from 86% to 89.5% (both set 2 and set 3). Similarly, Laws' features have shown an increase from 90.6% to 94.1% OCA. All features together from set 1, set 2, set 3 and set 4 have shown an OCA of 100% in E3C2, whereas it is 89.5% OCA in E1C2. These results show the significance of combining features from ROIs of original image with that of de-speckled images.

Classification results from 30 subsets:

The features that are passed through feature selection process have been repeated 30 times to obtain 30 subsets as mentioned earlier. The average accuracies with standard deviation are tabulated in Table 3.5. A feature set could be considered better for classification task if the standard deviation is less and the average accuracy is more. In other words, that feature set would result with better accuracy with most of the subsets. In that respect, experiment 1 (refer Table 3.5, E1C2) shows that RLM features from the ROIs of original images perform better with

average accuracy (in %) and standard deviation (AASD) of 84.0(1.7). Grad + RLM features from the ROIs of original images (in E1C2) and from the ROIs of images de-speckled by enhanced Lee method (in E2C2) showed an AASD of 84.7(2.4) and 86.4(2.5) respectively. This indicates the contribution of features from de-speckled images.

From Table 3.5, comparing the results of E1C2 and E3C2, RLM features have shown an increased AASD from 84(1.7) to 86.3(1.6) (set 2). GLCM features have performed better with AASD from 82.4(3.1) to 85.3(3.0) (set 2). Similarly, Laws features with AASD from 83.1(3.7) to 84(2.6) (set 1). Grad + RLM features are also on the same line with AASD from 84.7(2.4) to 86.2(1.6) (set 2). These results indicate the positive influence on classification by concatenating features from the ROIs of original images with that of de-speckled images in different combinations (as set1, set2, etc.).

3.4 Additional Observations from the present work

The contribution of individual texture feature category for classification of normal, MRD and cyst US images has been obtained. This has helped in reconsidering significant features in further processes. Concatenation of features like gradient (5 features-86% OCA) and RLM (44 features-82.5% OCA) have shown notable performance of 89.5% OCA (in original image) and 90.6 % OCA (in enhanced Lee image). The subsets (10 features) obtained from Grad + RLM (49 features) have 2 to 3 features of gradient. This shows the significance of gradient features in classification of kidney images.

From Table 3.3, though FOS features set is 100% accurate in classifying cyst, performed poor with MRD and normal. Gradient features showed promising improvement with accuracy of 98.8% for cyst, 86% for MRD and 87.2% for normal. Grad + RLM features from images de-speckled by enhanced Lee method showed improved performance than from that of original images. Accuracy has increased for cyst from 97.6% to 98.8% and for normal from 90% to 91.8%. The feature selection subsets of experiment 3 that gave best results, have 3 to 6 (out of 10) de-speckled image features. This indicates that features extracted from ROIs of de-speckled images have an additional contribution to make for objective classification. Thus, it is advantageous to concatenate features from ROIs of original image with that of de-speckled images.

From Table 3.4, comparing E1C2 and E3C2, RLM features have shown improvement in accuracy for cyst from 97.7% to 98.8%, for MRD from 89% to 90.6 and for normal from 87.1% to 91.8% with set 4. GLCM features have shown increased accuracy for cyst from 94.1% to 97.6% (set 1), for MRD from 87% to 91.8% (set 2) and for normal from 90.7% to 91.8% (set 2

and set 3). Similarly, Laws features have significant improvement in accuracy for MRD from 90.7% to 94.1% and for normal from 90.6% to 94.1% with set 3. All features sets i.e., All set 1, All set 2, All set 3 and All set 4 have exhibited prominent increase in accuracy for cyst from 96% to 100%, for MRD from 90.7% to 100 and for normal from 91.8% to 100%.

From Table 3.5, in E1C2, RLM features showed better performance with ASSD of 84(1.7). In E3C2, RLM, GLCM and Grad + RLM features performed better with set 2 compared to other sets. GLCM features of set 2 performed better (85.3(3.0)) than Laws features of set 1 (84.0(2.6)). But, Laws features consisted of less number of features and thus computations involved is less. RLM features of set 2 (88 features) performed better with ASSD of 86.3(1.6) with less computations involved. Thus, RLM features of set 2 are comparatively more promising with better accuracy for most of the subsets in the classification of kidney ultrasound images.

From Table 3.2, it is observed that the parameter β and FOM indicate Lee's sigma filter is better as mentioned earlier. From Table 3.5, it is reflecting from the contributions of Lee's sigma filter features. Enhanced Lee filter features have also performed well in classification, but no parameter of performance of de-speckling filter indicated about the same. Hence, there are no consistent correlation between the parameters signifying the performance of de-speckling methods and the classification results obtained from the features of de-speckled images.

3.5 Concluding Remarks

A classification study of three classes of kidney ultrasound images has been performed. ROIs from parenchyma region is considered for normal and MRD images and for cysts, ROIs are taken from within lesions as they are focal in nature. Among individual feature categories, gradient features and Grad + RLM features gave an OCA of 86% and 89.5% respectively, without feature selection. The maximum OCA of 90.6% is obtained from Laws' features after feature selection. The Laws' features of ROIs from original image concatenated with that of images de-speckled by Enhanced Lee method gave maximum OCA of 94.1% after feature selection. Thus, feature selection module is necessary to reduce the number of features without compromising on the OCA.

By considering all features from the ROIs of original as well as de-speckled images followed by feature selection gave maximum OCA of 100%. But, the idea of CAC system is to be interactive in real-time for the radiologists and extracting all features would take time comparatively. So, the most reliable features for the classification of ultrasound kidney images have been RLM and Grad features. RLM features from original images gave an AASD of 84.0(1.7). RLM features from set 2 gave an AASD of 86.3(1.6). Grad + RLM features from images

de-speckled by enhanced Lee filter gave an AASD of 86.4(2.5)**.** The promising results obtained from the present work indicate the usefulness of the proposed CAC system to aid radiologists in objective classification. Thus, the study concludes with the recommendation to consider texture features from the ROIs of de-speckled images and concatenating with that of original images for elevating the performance of classification.

The radiologist is of the opinion that the cyst is easily recognizable compared to the ambiguity between normal and MRD classes of kidney. In this chapter, the feature categories which performed better in case 1 of experiment 2 are only considered to carry out feature selection process i.e. case 2 of experiment 2. But, the possibility is that other feature categories may perform better when extracted from different de-speckling method. Hence, an exhaustive study is carried out considering normal and MRD classes of kidney and the results are presented in next chapter.

Chapter 4

Performance evaluation of texture features and de-speckling on the classification of B-mode kidney ultrasound images

4.1 Introduction

The chapter is an extended study on classification of kidney images in with continuation of previous chapter. Among the three classes of kidney, normal, MRD and cyst, cysts are easily distinguishable. Hence, in the present work, only normal and MRD classes are considered to evaluate the performance of classification without the bias of cyst class.

The distinct characteristics which contribute for the classification of normal and MRD lies in parenchyma of kidney and hence is the region of interest in the present work. A sample of normal kidney and MRD images with ROIs marked are shown in Figure 4.1. From Figure 4.1, it can be noted that, marking ROIs in the medullary region which has pyramids and renal columns is difficult. Hence, in the present work, ROIs are considered from the outer renal cortex region only.

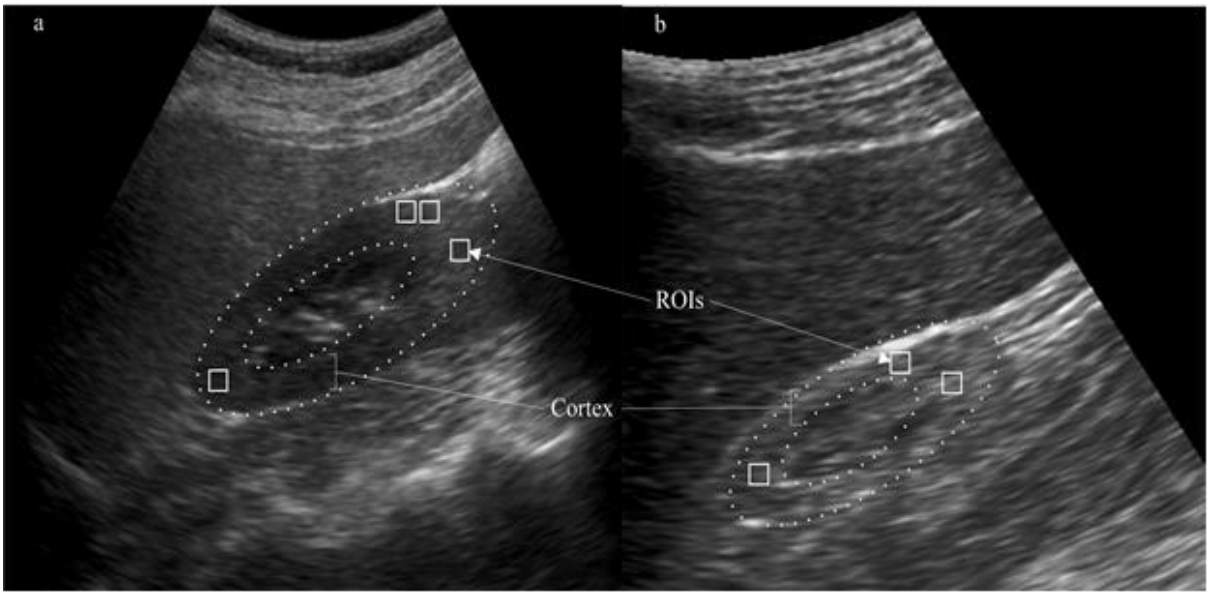

Figure 4.1: Example of B-mode Ultrasound kidney images with ROIs marked. A Normal and b MRD. The dots forming outer ellipse highlights the kidney and the area between the two ellipses represents cortex.

Speckle noise ingrained in B-mode ultrasound images is one of the factors restraining the radiologists in subjective diagnosis. At the same time, it also contains relevant information for the diagnosis. On one hand, as a part of computer-aided diagnosis, numerous de-speckling

methods have been proposed to facilitate better visualization to the radiologists. On other hand, de-speckling methods could be used as a pre-processing step to enhance the performance of objective classification.

The conclusion of Chapter 3 is that the features extracted from the de-speckled images increase the performance of classification [127]. In the present work, the extended objective is to evaluate the performance of a particular texture feature category with respect to different de-speckling methods on the classification of normal and MRD B-mode kidney ultrasound images. For that purpose, the same six texture feature categories and eight de-speckling methods considered in the previous chapter have been used.

4.2 Dataset Description

In the present work, clinically acquired data set used comprises of 19 B-mode kidney ultrasound images, i.e. 11 normal and 8 MRD images, collected from 19 patients. The details of database dispersal for training and testing phases of CAC system is depicted in Figure 4.2.

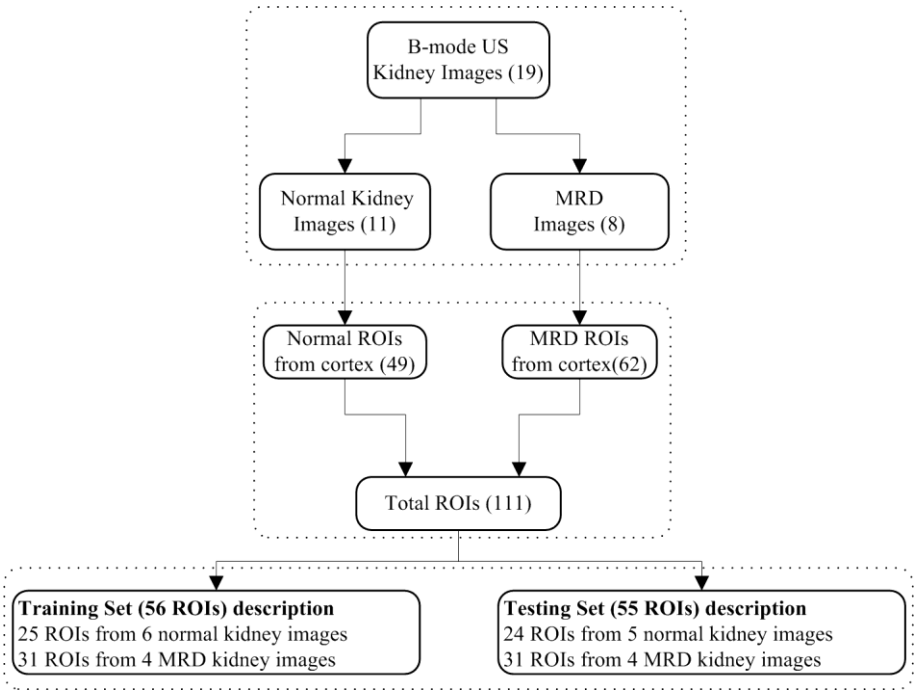

Figure 4.2: Dataset Description

4.3 Experimental Results

The proposed CAC system for the classification of normal kidney and MRD is as shown in Figure 4.3.

In the present work, four experiments are performed with two cases in each i.e. without feature selection and with feature selection. In experiment 1 (Exp 1), features extracted using six

texture feature categories from original images are considered for the classification. In experiment 2 (Exp 2), features from Exp 1 concatenated in different combinations are used for the classification task. In experiment 3 (Exp 3), features extracted from images de-speckled by eight methods are used for the classification task. In experiment 4 (Exp 4), the features used in Exp 3 are concatenated in combinations same as that of Exp 2 and are provided to the classification task.

The performance of classification is evaluated using overall classification accuracy (OCA), best OCA of a subset (out of 30 subsets) and average accuracy (standard deviation) (AASD). Accordingly, OCA, best OCA and AASD of all the four experiments are tabulated in Table 4.1, Table 4.2 and Table 4.3 respectively. In Table 4.1, Table 4.2 and Table 4.3, each row corresponds to particular features set, mentioned in the first column. Along columns, features from original images and de-speckled images are represented. For example, FOS features from original images (Exp 1) resulted in an OCA of 67.2 % (refer Table 4.1). 'All ftrs' represents concatenation of features from all the categories.

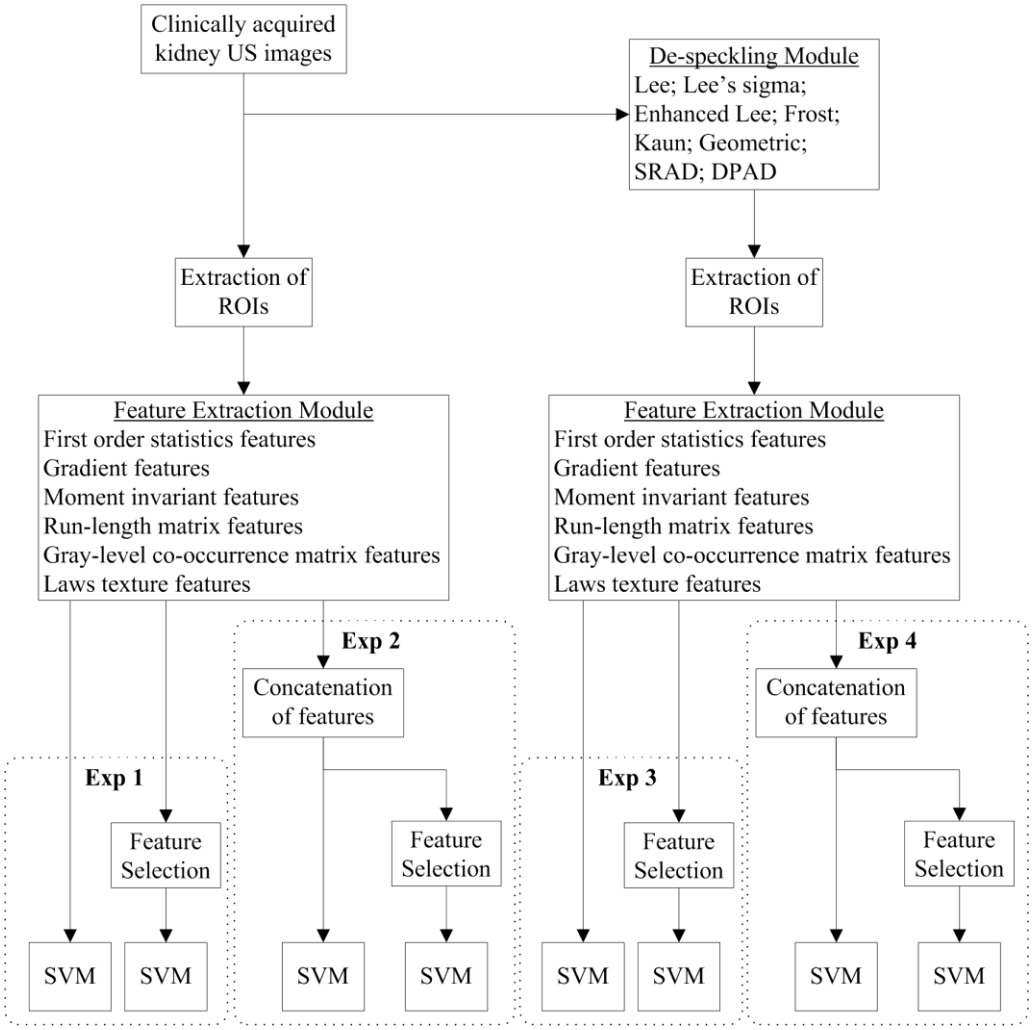

Figure 4.3: Proposed CAC system

OCAs obtained before feature selection (refer Table 4.1)

Among the individual feature categories of original images (Exp 1) and de-speckled images (Exp 3), RLM features from the images de-speckled by Frost method resulted with a highest OCA of 87.2 %. Grad features from the images de-speckled by enLee method and GLCM features from the images de-speckled by Frost method gave an OCA of 81.8 %. But, number of features involved with Grad category is only five. Laws features from images de-speckled by enLee and Frost methods exhibited same performance with an OCA of 80 %.

Out of six, four categories of texture features i.e. Grad, RLM, GLCM and Laws, performed better and hence are considered for concatenation. Among the concatenated feature sets of original images (Exp 2) and de-speckled images (Exp 4), concatenation of Grad (81.8 %) and RLM (83.6 %) features of images de-speckled by enLee method resulted in an enhanced outcome with an OCA of 87.2 %. Similarly, concatenation of Grad (78.1 %) and GLCM (81.8 %) features of images de-speckled by Frost method gave an OCA of 85.4%. All ftrs from enLee method gave an improved OCA of 85.4 %, compared to that of individual sets.

Best OCAs obtained after feature selection (refer Table 4.2)

Individual feature categories and concatenated feature sets having more than 10 features are considered for feature selection process. Each feature set has been through the feature selection process 30 times to obtain 30 optimal subsets. The best OCA obtained for a subset among the 30 subsets has been mentioned in Table 4.2.

Among the individual feature categories, RLM features from the images de-speckled by Frost method have shown an increase in OCA from 87.2 % (Table 4.1) to 92.7 % (Table 4.2). Similarly, GLCM features from images de-speckled by Lee's sigma (Lee 2) and enLee methods have resulted in an enhanced OCA from 76.3 % (Table 4.1) to 92.7 % (Table 4.2) and 80 % (Table 4.1) to 92.7 % (Table 4.2) respectively. Among concatenated feature sets, Grad + GLCM and RLM + GLCM feature sets from the images de-speckled by enLee method have shown improved OCA from 80 % (Table 4.1) to 92.7 % (Table 4.2). On the same line, RLM + Laws features set from the images de-speckled by Frost and Kaun methods have boosted the OCA from 87.2 % (Table 4.1) to 92.7 % (Table 4.2) and 78.1 % (Table 4.1) to 92.7 % (Table 4.2) respectively.

AASD of 30 subsets (refer Table 4.3)

From the 30 optimal subsets obtained for each feature set, average accuracy (standard deviation) is computed and tabulated in Table 4.3. Feature set having higher average accuracy and less standard deviation implies that the most of the subsets of that feature set are resulting in higher OCAs. Hence, the feature set is able to provide optimal subsets.

Table 4.1: OCAs without feature selection

Features	Exp No.	Original image	Exp No.	De-speckling methods							
				Lee 1	Lee 2	enLee	Frost	Kaun	Geo	SRAD	DPAD
FOS	Exp 1	67.2	Exp 3	69	67.2	65.4	67.2	69	67.2	67.2	***76.3***
Grad		78.1		65.4	78.1	**81.8**	78.1	65.4	78.1	*76.3*	61.8
MI		63.6		63.6	63.6	58.1	63.6	63.6	61.8	**67.2**	**67.2**
RLM		81.8		83.6	81.8	83.6	***87.2***	83.6	76.3	74.5	56.3
GLCM		76.3		76.3	76.3	80	**81.8**	78.1	80	72.7	61.8
Laws		72.7		70.9	72.7	**80**	**80**	70.9	74.5	72.7	65.4
Grad + RLM	Exp 2	*85.4*	Exp 4	*85.4*	*85.4*	***87.2***	***87.2***	*85.4*	80	74.5	69
Grad + GLCM		76.3		80	76.3	80	**85.4**	80	*81.8*	72.7	72.7
RLM+GLCM		76.3		80	76.3	80	**83.6**	80	80	72.7	58.1
Grad + Laws		74.5		67.2	74.5	**81.8**	78.1	67.2	80	74.5	65.4
RLM + Laws		78.1		78.1	78.1	85.4	***87.2***	78.1	78.1	*76.3*	69
GLCM + Laws		74.5		78.1	74.5	83.6	***87.2***	80	70.9	74.5	69
All ftrs		76.3		81.8	76.3	**85.4**	**85.4**	80	74.5	72.7	67.2

Note: OCA: Overall classification accuracy; Exp No: Experiment number
The values in **bold** represents the best along the row and the values in *italics* represents the best along the column

Table 4.2: Best OCA of a subset (out of 30 subsets) obtained after feature selection

Features	Exp No.	Original image	Exp No.	De-speckling methods							
				Lee 1	Lee 2	enLee	Frost	Kaun	Geo	SRAD	DPAD
RLM		87.2		89	90.9	89	***92.7***	85.4	85.4	76.3	61.8
GLCM	Exp 1	89	Exp 3	*90.9*	***92.7***	***92.7***	90.9	90.9	87.2	78.1	69
Laws		81.8		81.8	80	**83.6**	**83.6**	81.8	**83.6**	78.1	76.3
Grad + RLM		89		85.4	89	**90.9**	**90.9**	87.2	*89*	78.1	70.9
Grad + GLCM		89		89	90.9	***92.7***	***92.7***	90.9	87.2	78.1	65.4
RLM + GLCM		*90.9*		*90.9*	90.9	***92.7***	***92.7***	90.9	87.2	*81.8*	67.2
Grad + Laws	Exp 2	83.6	Exp 4	80	81.8	83.6	83.6	83.6	**85.4**	*81.8*	*78.1*
RLM + Laws		89		89	87.2	90.9	***92.7***	***92.7***	*89*	80	74.5
GLCM + Laws		87.2		81.8	87.2	85.4	**89**	83.6	85.4	80	76.3
All ftrs		89		89.6	89	**90.9**	89	85.4	*89*	*81.8*	76.3

Note: OCA: Overall classification accuracy; Exp No: Experiment number
The values in **bold** represents the best along the row and the values in *italics* represents the best along the column

Table 4.3: AASD of 30 subsets obtained after feature selection

Features	Exp No.	Original image	Exp No.	De-speckling methods							
				Lee 1	Lee 2	enLee	Frost	Kaun	Geo	SRAD	DPAD
RLM		81.3(2.8)		79.9(3.9)	81.6(3.3)	82.2(2.8)	***87(2.9)***	78.8(3.8)	78.0(3.6)	72.2(2.6)	57.3(1.7)
GLCM	Exp 1	85.3(3.7)	Exp 3	86.7(2.2)	*85.7(4.4)*	***86.9(2.8)***	86.9(3.6)	86.3(2.5)	74.5(7.1)	74.6(2.7)	58.7(3.0)
Laws		74.4(3.5)		71.8(12.8)	73.9(3.8)	75.6(3.5)	**77.4(3.0)**	74.5(4.4)	76.1(3.6)	71.1(3.6)	67.0(3.5)
Grad + RLM		82.0(3.8)		80.6(3.0)	82.6(3.2)	84.0(2.4)	**86.9(2.2)**	80.5(4.3)	79.1(5.0)	73.1(2.7)	61.5(4.2)
Grad + GLCM		*85.8(3.1)*		***86.7(1.6)***	84.6(4.4)	86.5(3.6)	86.0(4.9)	*86.5(2.2)*	79.1(7.7)	*74.9(1.8)*	59.3(3.1)
RLM + GLCM		84.4(2.9)		84.0(4.4)	84.6(3.3)	85.8(4.0)	**85.8(2.7)**	83.5(5.5)	75.7(5.1)	74.7(2.9)	60.0(3.3)
Grad + Laws	Exp 2	75.2(4.3)	Exp 4	75.5(4.1)	73.8(4.2)	76.8(3.7)	**78.2(2.7)**	75.8(4.9)	76.9(4.2)	73.1(5.6)	67.1(3.2)
RLM + Laws		79.4(4.1)		78.5(4.0)	79.9(4.4)	82.4(4.8)	**86.0(5.0)**	79.5(4.9)	*80.7(4.3)*	70.8(4.2)	69.4(3.3)
GLCM + Laws		77.4(3.8)		76.3(4.2)	78.1(4.7)	77.8(4.5)	**79.9(5.0)**	76.9(4.7)	78.2(4.3)	74.2(3.0)	*70.6(3.7)*
All ftrs		80.3(4.3)		77.3(5.5)	79.8(5.1)	79.8(5.2)	**83.1(4.3)**	78.1(4.7)	79.4(5.1)	73.9(3.3)	70.1(3.7)

Note: AASD: Average accuracy (standard deviation); Exp No: Experiment number

The values in **bold** represents the best along the row and the values in *italics* represents the best along the column

Among the individual feature sets, RLM features from the images de-speckled by Frost method have performed better with an AASD of 87(2.9). GLCM features from the images de-speckled by enLee method also performed quite near with an AASD of 86.9(2.8). Among concatenated feature sets, Grad + RLM feature set from the images de-speckled by Frost method performed better with decreased SD i.e. AASD of 86.9(2.2). Grad + GLCM features from the images de-speckled by Lee method (Lee 1) have shown promising result with an AASD of 86.7(1.6). For most of the feature sets, features from the images de-speckled by Frost method have performed better compared to features from the images de-speckled by other methods.

4.4 Additional observations from the present work

Features perspective

Among the six categories of texture features, FOS and MI have not shown satisfactory performance compared to other categories. Grad features from the images de-speckled by enLee method have shown improved performance with an OCA of 81.8 % whereas that of original images was 78.1 %. Similarly, RLM features from original images and the images de-speckled by Frost method gave an OCA of 81.8 % and 87.2 % respectively. GLCM features from the images de-speckled by Frost method have shown increased OCA of 81.8 % compared to that of original images was 76.3 % OCA. Laws' features from the images de-speckled by enLee and Frost methods have shown same response with an OCA of 80 %, whereas that of original images was 72.7% (refer Table 4.1). Similarly, for concatenated feature sets, features from the images de-speckled by enLee and Frost methods have enhanced performance compared to that of original images.

De-speckling methods perspective

For original images and the images de-speckled by Lee 1, Lee 2 and Kaun methods, Grad + RLM features performed better with an OCA of 85.4 %. For images de-speckled by enLee and Frost methods, Grad + RLM features outperformed with an OCA of 87.2 %. Among the features from the images de-speckled by Geometric (Geo) method, Grad + GLCM features have shown better performance with an OCA of 81.8 % (refer Table 4.1).

After feature selection, Grad + GLCM features from the original images performed better with an AASD of 85.8(3.1) (refer Table 4.3). Similarly, for the images de-speckled by Lee 1 and Kaun methods, Grad + GLCM features outperformed with an AASD of 86.7(1.6) and 86.5(2.2) respectively. In case of images de-speckled by Lee 2 and enLee methods, GLCM features stands first with an AASD of 85.7(4.4) and 86.9(2.8) respectively. For the images de-speckled by Frost method, RLM features have shown better results with an AASD of 87(2.9).

Results are indicating that the features of each category obtained from images de-speckled by various methods perform differently. Selection of appropriate combination of texture feature category and the method used to de-speckle the images is a vital step in enhancing the performance of a CAC system.

4.5 Concluding Remarks

In the present work, a CAC system is proposed for the classification of normal and MRD classes of kidney using B-mode ultrasound images. To evaluate the performance of texture features and de-speckling on the classification task, six categories of texture features and eight de-speckling methods are used. Both individual feature sets and concatenated feature sets have been considered for the evaluation. Grad features set having five features from the images de-speckled by enLee method have shown promising OCA of 81.8 % without feature selection.

RLM features from the images de-speckled by Frost method which involved 44 features resulted in a best performance with an AASD of 87(2.9) for the classification of normal and MRD classes of kidney using B-mode ultrasound images. The promising results suggests that the proposed CAC system can be used by the radiologists in their regular clinical diagnosis of normal and MRD classes using B-mode kidney ultrasound images. From the exhaustive experiments carried out on the proposed CAC system, it is recommended to consider an appropriate combination of texture feature category and the de-speckle method as a pre-processing step to improve the performance of a CAC system. The comparative discussions on the performance of CAC systems in chapter 3 and chapter 4 are given in the conclusion chapter (chapter 7).

With next chapter (chapter 5), the CAC systems involving liver images are discussed in detail.

Chapter 5
CAC system for B-mode fatty liver ultrasound images using texture features

5.1 Introduction

Liver is considered as a vital organ because of its functions such as detoxification, protein synthesis and aiding in digestion by the production of necessary bio-chemicals. Hence, survival of a person is at risk in case of liver diseases [8]. Though the diagnosis of liver diseases is carried through liver function tests which include clinical biochemistry and blood tests, radiological study is also required in most of the cases [11]. Ultrasonography is preferred over computed tomography (CT) because of its non-radiation and inexpensive nature. It is also non-invasive and conducive for real-time applications.

Fatty liver or fatty liver disease (FLD) occurs because of accumulation of triglyceride fat in liver cells creating large vacuoles. Though it is a reversible condition, if not treated in time it may lead to inflammation of liver, which in turn can cause fibrosis and hardening of liver. When fibrosis condition becomes extensive, the condition is termed as cirrhosis which often results in liver failure [60]. Hence, it is very important to detect the grades of fatty liver at an earlier stage. Based on visual characteristics of B-mode ultrasound images, medical fraternity characterise fatty liver disease as mild, moderate and severe fatty liver according to degree of severity, which in turn help clinicians in treatment planning and further investigations.

A CAC system provides the objective aid to the domain experts in their diagnosis. This is required because of inter and intra-observer variability in subjective perception and its implications on the diagnosis, which is critical [13].

In the present work, a CAC system is proposed for the diagnosis of grades of fatty liver disease along with normal liver tissue by using B-mode ultrasound images. In literature, there are many contributions towards classification of normal, fatty liver and cirrhosis using different features [55-59]. Only recently [60], grades of fatty liver along with normal liver are considered for numerical grading. In their study, gray relational analysis (GRA) method has been utilized for numerical grading of fatty liver based on brightness level comparison between liver images and kidney parenchyma as reference from the same subject. But, this factor is not reliable as the echogenicity of kidney parenchyma changes in case of kidney diseases [13]. The most frequently

considered factors are increased liver echogenicity, impaired visualization of hepatic vessels and diaphragm [6].

The echo-textural characteristics of liver images considered in this study are outlined in the sequence of their developmental stage in Table 5.1.

Table 5.1: Echo-textural characteristics of liver images

Echo-textural characteristics	Normal	Fatty liver		
		Mild	Moderate	Severe
Liver echo-texture	Homogeneous Medium echogenicity	Increased echogenicity	Increased than mild	Increased than moderate
Diaphragm visibility	Normal	Normal	Less than mild	Poor or no visibility

The echo-textural characteristics and diaphragm visibility of normal liver tissue is considered as reference. The degree of variation from normal liver tissue is the basis for defining the echo-textural characteristics and diaphragm visibility of grades of fatty liver. As the degree of severity increases from mild-moderate-severe fatty liver, echogenicity of liver increases and diaphragm visibility degrades [13].

5.2 Dataset Description

For the present work, fifty three B-mode ultrasound images consisting of 12 normal, 14 mild, 14 moderate and 13 severe fatty liver images of 53 patients are used. In the present work, liver ROIs (LROIs) are considered to represent the echogenicity of liver parenchyma and one diaphragm ROI (DROI) is considered to represent its visibility in each image. As fatty liver is diffused liver disease, the echogenic characteristics spread all over the liver parenchyma. For each image, an adequate number of LROIs are extracted excluding hepatic ducts and blood vessels. As suggested by the participating radiologist, one DROI for each image is also extracted. Totally, 60 LROIs for each class (normal, mild, moderate and severe fatty liver) and 53 DROIs i.e., one DROI from each image of normal, mild, moderate and severe fatty liver classes are extracted. Detailed dataset descriptions used for training and testing phases of CAC system are illustrated in Figure 5.1. An image with ROIs marked is shown in Figure 5.2.

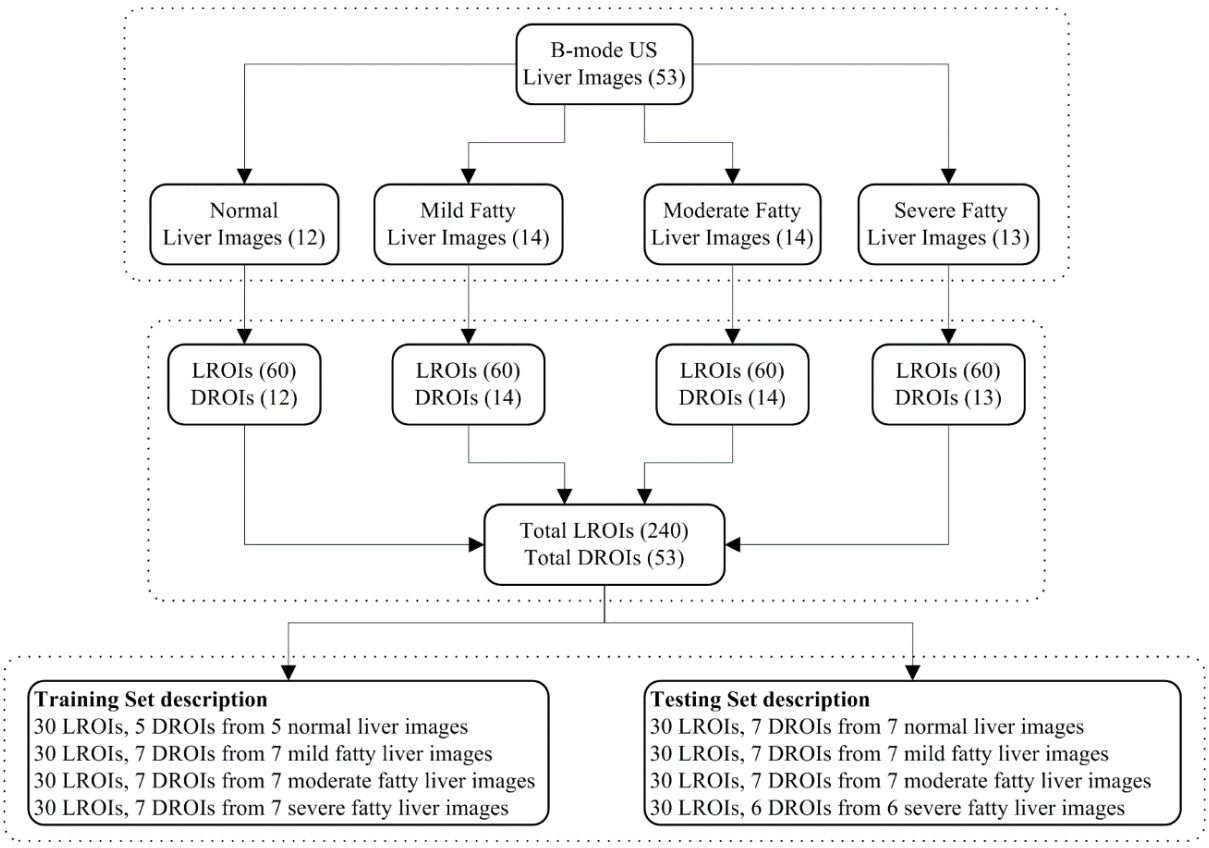

Figure 5.1: Dataset Description

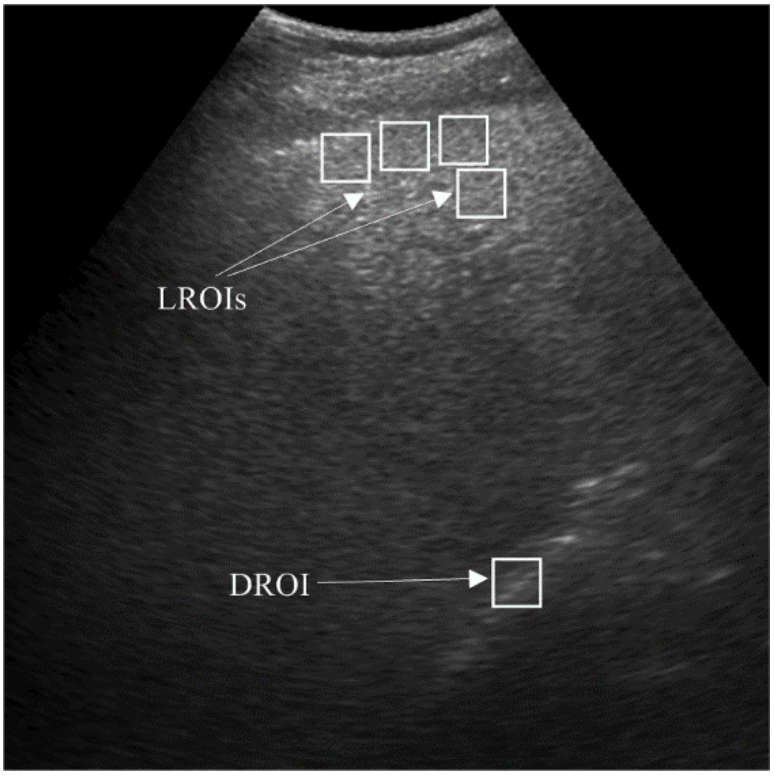

Figure 5.2: An example showing LROIs and DROI marked on severe fatty liver image

5.3 Feature sets

Texture features are extracted from LROIs to form one feature set to perform the classification task. To improve the accuracy, features are also extracted from considering DROI for each image. The features from LROIs and corresponding DROI are combined in three ways to form (i) ratio features set, (ii) inverse ratio features set and (iii) additive features set. Each LROI feature value is divided by corresponding DROI feature value of that image to obtain ratio feature value (equation 1) [107], its reciprocal gives inverse ratio feature value (equation 2) and their addition gives additive feature value (equation 3).

$$ratio\ feature\ value = \frac{LROI\ feature\ value}{DROI\ feature\ value} \quad (1)$$

$$inverse\ ratio\ feature\ value = \frac{DROI\ feature\ value}{LROI\ feature\ value} \quad (2)$$

$$additive\ feature\ value = LROI\ feature\ value + DROI\ feature\ value \quad (3)$$

5.4 Experimental Results

The block diagram of proposed CAC system for the classification of normal and grades of fatty liver images is shown in Figure 5.3.

Three experiments are carried out in the present work with two cases i.e., with and without feature selection, in each.

In *experiment 1*(**Exp 1**), features extracted from LROIs (**lftrs**) are considered for the classification task.

In *experiment 2*(**Exp 2**), DROIs are also considered along with LROIs and combined as described earlier to obtain ratio features set (**rftrs**), inverse ratio features set (**irftrs**) and additive features set (**aftrs**). These feature sets are fed separately for the individual classifiers.

In *experiment 3*(**Exp 3**), **lftrs**, **rftrs**, **irftrs** and **aftrs** are concatenated in different combinations to obtain the classification accuracy.

Experiment 1: The results of **Exp 1** are tabulated in Table 5.2. It shows very poor performance, with the highest overall classification accuracy (OCA) being 44.1% for **MI** features **(lftrs)**. Hence, **lftrs** are not considered for feature selection process.

Experiment 2: With **All** features **(rftrs)** taken together, have shown better performance with an OCA of 76.6%. But, from Table 5.3 it is clear that the major contribution is of **FOS** features **(rftrs)** and **Laws** features **(rftrs)** which individually outperformed with an OCA of 79.1% and

80% respectively. **FOS+Laws** features **(rftrs**) have shown degraded OCA of 78.3%. FOS+Laws features (irftrs and aftrs) are not considered as their OCAs are not good enough individually.

Irftrs have shown considerable OCAs. With **All** features **(irftrs)** taken together, have been able to perform with an OCA of 73.3%, whereas the major contribution comes from the **Laws** features **(irftrs)** which resulted with an OCA of 70.8%. **aftrs** have resulted in lower OCAs.

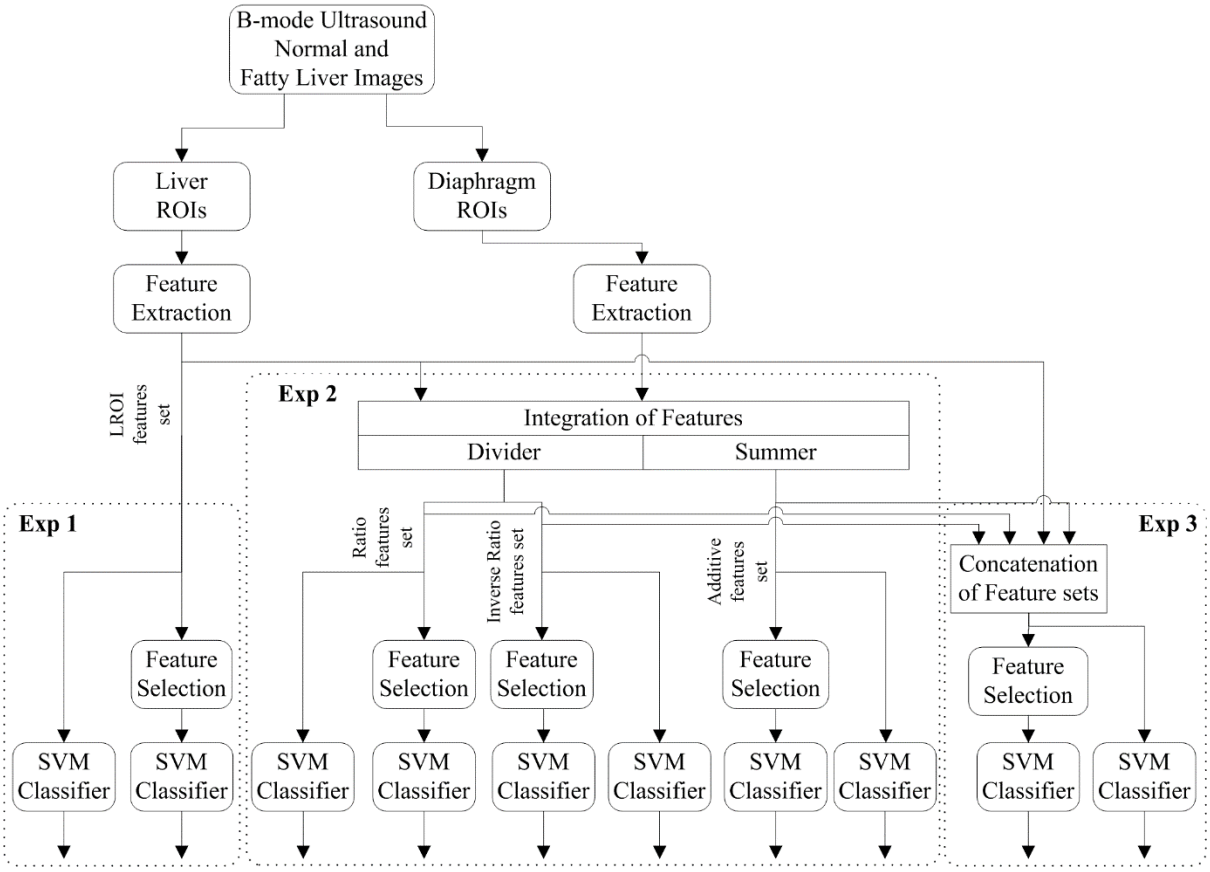

Figure 5.3: Proposed CAC system

Table 5.2: Classification results of **Experiment 1** without feature selection

Texture features	Lftrs
All ftrs	34.1
FOS	35.8
Grad	34.1
MI	44.1
RLM	43.3
GLCM	40
Laws	37.5

Table 5.3: Classification results (OCAs in %) of **Experiment 2** without feature selection

Texture features	rftrs	irftrs	aftrs
All ftrs	**76.6**	**73.3**	51.6
FOS	79.1	65	55.8
Grad	65	58.3	40.8
MI	68.3	66.6	34.1
RLM	51.6	52.5	50
GLCM	60	60.8	46.6
Laws	**80**	**70.8**	56.6
FOS+Laws	**78.3**		

Table 5.4: Classification results: average accuracy (standard deviation) of **Experiment 2** with feature selection

Texture features	rftrs	irftrs	aftrs
All ftrs	85.2(2.9)	82.0(2.7)	70.7(3.0)
RLM	56.3(3.1)	59.4(1.5)	57.6(2.7)
GLCM	66.8(3.3)	67.3(2.6)	62.4(4.1)
Laws	**84.9(3.2)**	79.1(2.8)	66.6(3.0)
FOS+Laws	**85.4(3.6)**		

The number of features in **Grad**, **MI** and **FOS** feature categories, are less than or equal to 10. So, except **Grad**, **MI** and **FOS** features, the rest of the feature categories are presented for feature selection. For each feature set, DEFS process is repeated 30 times to obtain 30 subsets. The average accuracies and standard deviations are tabulated in Table 5.4. **FOS+Laws** features **(rftrs)** have shown increased accuracy of 85.4(3.6). Whereas, **Laws** features **(rftrs)** have resulted with an average accuracy (standard deviation) of 84.9(3.2) with less computations involved. Compared to **rftrs, irftrs** and **aftrs** have no promising results to offer here.

Experiment 3: **rftrs+irftrs** have produced OCAs of 76.6%, 75.8%, 77.5% and 71.6% for **all** features taken together, **FOS** features, **Laws** features and **FOS+Laws** features respectively (refer Table 5.5). Because of less number of features in **Grad** and **MI** feature categories, except **Grad**, **MI** features, other features are fed through feature selection process. After feature selection, **FOS+Laws** features **(rftrs+irftrs)** have outperformed with an average accuracy (standard deviation) of 85.4(2.7) (refer Table 5.6).

Table 5.5: Classification results (OCAs in %) of **Experiment 3** without feature selection

Texture features	**rftrs + irftrs**	**rftrs + aftrs**	**irftrs + aftrs**	**lftrs + rftrs**	**lftrs + irftrs**	**lftrs + aftrs**
All ftrs	**76.6**	61.6	63.3	61.6	59.1	45
FOS	75.8	55.8	63.3	38.3	59.1	50.8
Grad	60.8	44.1	48.3	53.3	53.3	40.8
MI	67.5	60.8	52.5	63.3	45.8	48.3
RLM	50.8	50.8	53.3	45.8	51.6	46.6
GLCM	57.5	54.1	50	53.3	42.5	41.6
Laws	**77.5**	60.8	64.1	60.8	61.6	56.6
FOS+Laws	**71.6**					

Table 5.6: Classification results: average accuracy (standard deviation) of **Experiment 3** with feature selection

Texture features	**rftrs + irftrs**	**rftrs + aftrs**	**irftrs + aftrs**	**lftrs + rftrs**	**lftrs + irftrs**	**lftrs + aftrs**
All ftrs	85.0(2.1)	81.0(3.3)	79.9(3.2)	83.5(3.3)	80.9(2.4)	72.4(2.7)
FOS	73.1(1.2)	61.8(2.7)	65.0(2.5)	58.6(2.3)	67.6(3.8)	61.1(1.6)
RLM	59.2(3.1)	59.4(3.9)	59.6(4.1)	59.2(2.9)	60.7(2.7)	56.5(3.4)
GLCM	66.6(2.5)	66.9(3.4)	69.1(3.0)	65.3(3.0)	66.3(2.7)	60.7(4.0)
Laws	85(4.0)	81.4(2.6)	79.6(2.7)	82.4(5.7)	79.4(2.5)	69.4(2.8)
FOS+Laws	**85.4(2.7)**					

Discussion on experiment 2 and 3: From Table 5.3 and 5.5, features of **RLM (rftrs)** and **RLM (lftrs+irftrs)** obtained an OCA of 51.6%. After feature selection, an average accuracy and standard deviation of **RLM** features **(rftrs)** is 56.3(3.1) (refer Table 5.4) and that of **RLM** features **(lftrs+irftrs)** is 60.7(2.7) (refer Table 5.6). It is also noted that **RLM** features **(lftrs+irftrs)** obtained best average accuracy and standard deviation of 60.7(2.7) among other combinations. From Table 5.6, **GLCM** features **(aftrs+irftrs)** obtained best average accuracy and standard deviation of 69.1(3.0) among other combinations. These results indicate the significance of **irftrs** in combination with **lftrs** and **aftrs** for **RLM** and **GLCM** feature categories respectively.

Features of **Laws (rftrs+aftrs)** and **Laws (lftrs+rftrs)** obtained an OCA of 60.8% (refer Table 5.5). After feature selection, an average accuracy (standard deviation) obtained by **Laws** features **(rftrs+aftrs)** is 81.4(2.6) and that of **Laws** features **(lftrs+rftrs)** is 82.4(5.7) (refer Table 5.6). These results are projected on **All** features taken together obtaining 61.6% of OCA for **All**

features **(rftrs+aftrs)** and **All** features **(lftrs+rftrs)** (refer Table 5.5). After feature selection, an average accuracy (standard deviation) of 81.0(3.3) and 83.5(3.3) obtained respectively (refer Table 5.6). These results indicate the significance of **lftrs** over **aftrs**, when concatenated with **rftrs**.

5.5 Additional observations from the present work

This study revealed that texture features considered are not efficient in distinguishing the normal and grades of fatty liver images if features from only LROIs extracted are used (refer Table 5.2). Features extracted from DROI combined with features extracted from LROIs have shown increased OCA (refer Table 5.4), thereby indicating the presence of relevant information in features extracted from DROI for the task. The present work also shows that when features of two ROIs are to be combined to represent a class of image, the way chosen to combine has a significant role to play.

In [107], only ratio features have been considered for the study and there is no reason mentioned for the same. Hence, in the present work, in addition to ratio features other potential possibilities such as inverse ratio features and additive features are also explored for the classification of normal and grades of fatty liver images. The **lftrs**, **rftrs**, **irftrs** and **aftrs** are concatenated in different combinations. There is increased average accuracy (standard deviation) in **RLM** features **(lftrs+irftrs)** and **GLCM** features **(irftrs+aftrs)** (refer Table 5.6). These findings reveal that, concatenation of feature sets may increase the classification accuracy for particular feature category such as **RLM.** The combination for which better classification accuracy is obtained, may be different for different feature category as shown in above example.

5.6 Concluding Remarks

Medical domain knowledge for the diagnosis of severity of fatty liver images has been utilized in objectifying the task of classification of normal, mild, moderate and severe fatty liver images. The results have proved that the features extracted from only LROIs are not sufficient enough for the classification of normal and grades of fatty liver images e.g. **Laws** features OCA is 37.5%. Features extracted from DROI combined with features extracted from LROIs obtained an increase in OCA, e.g. **Laws feature (rftrs)** OCA is 80%. After feature selection, **Laws** features **(rftrs)** obtained an average accuracy (standard deviation) of 84.9(3.2). The promising results obtained by the present work indicate that the proposed CAC system is of significant utility in objective assistance for the radiologists in routine clinical diagnosis of fatty liver disease.

The radiologist is of the opinion that, there is an ambiguity often faced in distinguishing severe fatty liver and cirrhosis which is an advanced stage of the former. From the present work, if the result of an image given to the CAC system is recognised as a severe fatty liver, then to overcome the ambiguity, a separate binary CAC system would be necessary. This is of the reason that, in case of cirrhosis, visibility of diaphragm is not a consistent reliable feature according to the radiologist. The same has been observed in the database of cirrhosis images. Thus, a separate CAC system has been proposed for the classification of severe fatty liver and cirrhosis. The details of second CAC system for liver images are presented in next chapter.

Chapter 6
CAC system for severe fatty liver and cirrhosis using B-mode ultrasound images

6.1 Introduction

Excess accumulation of triglyceride fat in hepatic cells creates large vacuoles. This condition is termed as fatty liver or fatty liver disease (FLD). In case, this condition is not detected and treated at the initial stage, its consecutive developmental stages are fibrosis and hardening of the liver. The condition of too much fibrosis of liver is termed as cirrhosis and often results in liver failure [60]. Hence, detection of fatty liver at the earlier stage becomes clinically significant. Medical fraternity recognize fatty liver disease in three stages such as mild, moderate and severe fatty liver according to degree of severity. Beyond severe fatty liver is the irreversible stage of cirrhosis. This stage-wise characterization of disease helps clinicians in treatment planning.

The presence of inter and intra-observer variations involved in subjective perception and its implications on the diagnosis of fatty liver have been stated in study [13]. Hence, a computer-aided classification (CAC) system is extremely required to provide an objective aid to the medical fraternity for differential diagnosis between severe fatty liver and cirrhosis.

In literature, there are CAC systems proposed for normal and cirrhotic liver images [10, 14-18]. Radiologists opined that, differential diagnosis between severe fatty liver and cirrhotic liver images is a challenging task, as the latter may be an advanced stage of former condition. Also the differential diagnosis between severe fatty liver and cirrhotic liver is clinically significant as FLD is reversible, whereas cirrhosis is not. Accordingly, in the present work a CAC system for differential diagnosis between severe fatty liver disease and cirrhotic liver is proposed.

The factors often considered in characterizing grades of fatty liver are increased liver echogenicity, impaired visualization of hepatic vessels and diaphragm [6]. As participating radiologist opined that the visibility of diaphragm is not considered as a criterion in the diagnosis of cirrhotic liver, regions of interest (ROIs) extracted from liver parenchyma (LROIs) are considered in the present work.

6.2 Dataset Description

Image database used in the present work consists of total twenty-nine B-mode ultrasound images with 13 severe fatty liver images and 16 cirrhotic liver images collected from 29 patients. The echogenic characteristics spread all over the liver parenchyma as severe fatty liver disease

and cirrhosis are diffuse liver diseases. As per the opinion of experienced participating radiologist, sufficient numbers of LROIs are extracted from each image excluding blood vessels and hepatic ducts. For both the classes, 60 LROIs are extracted. The description of distribution of dataset for training and testing phases of CAC system is shown in Figure 6.1.

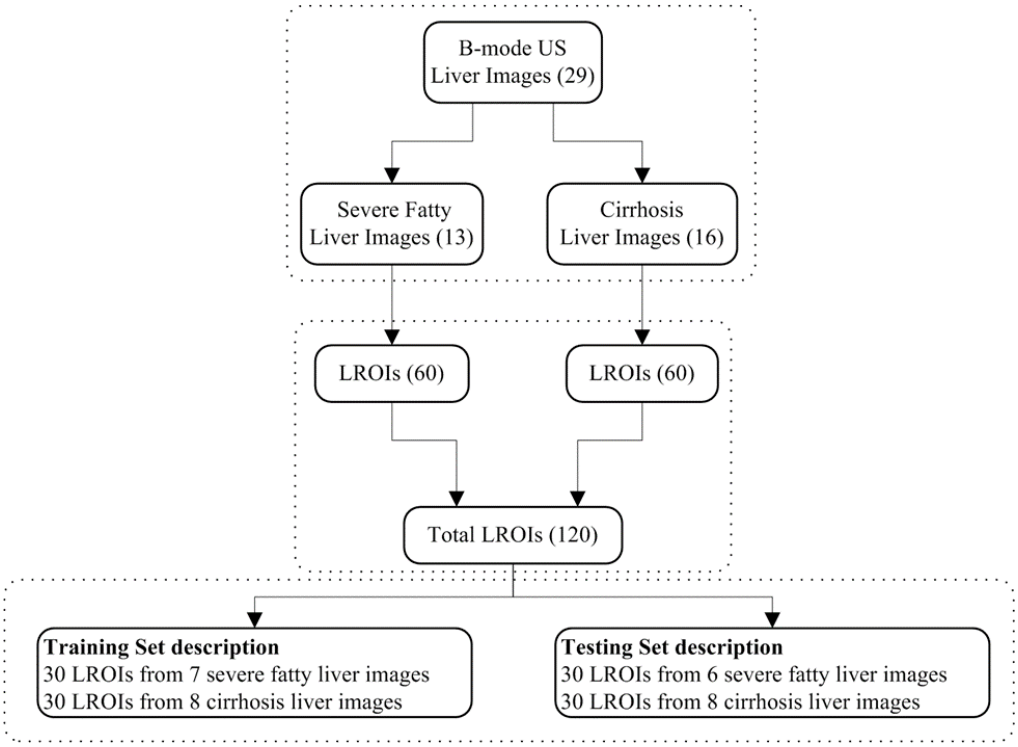

Figure 6.1: Dataset Description

6.3 Experimental Results

The proposed CAC system for the classification of severe fatty liver and cirrhotic liver consists is depicted in the block diagram shown in Figure 6.2.

The proposed CAC system has been designed for differential diagnosis between severe fatty liver and cirrhotic liver images. Radiologists opined that in cases of cirrhosis, visibility of diaphragm is not considered as a criterion. Rather, the coarse texture, nodularity and shrinkage of liver size are considered. Hence, only echo-textural characteristics within liver parenchyma are considered here. Texture features are extracted from the LROIs of severe fatty liver and cirrhotic liver images.

Two experiments are carried out in the present work. In experiment 1, overall classification accuracy (OCA), sensitivity for severe fatty liver and sensitivity for cirrhotic liver are computed from confusion matrix. These results are obtained without feature selection for individual texture feature categories and for concatenated feature sets. Allftrs represents concatenation of features of six categories.

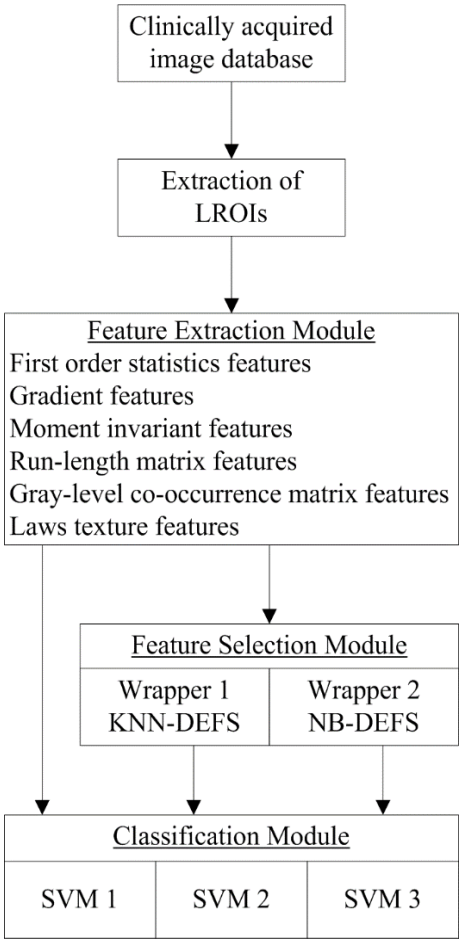

Figure 6.2: Proposed CAC system

In experiment 1, the design of CAC system without feature selection for different texture feature categories is experimented and the results obtained are tabulated in Table 6.1. It can be observed that the MI features set consisting of seven features, yield the sensitivity value of 96.6% for cirrhotic liver, though the OCA is poor. The FOS features set which consists of ten features has been able to classify with an OCA of 98.3 %. The Grad features set which contains only five features has also shown better classification with an OCA of 93.3 %. The Laws features set achieved the OCA value of 91.6 %. Hence, these three categories (FOS, Grad and Laws) are considered in different combinations for concatenation. From Table 6.1, it can be observed that without feature selection concatenated sets have not shown improvement compared to the individual feature sets.

In experiment 2, except FOS, MI and Grad feature sets which consists of less than or equal to 10 features, other feature sets and concatenated feature sets are considered for feature selection. For feature selection, 30 subsets are obtained by repeating DEFS algorithm 30 times. The subsets are obtained separately from KNN-DEFS and NB-DEFS. Experiment 2 consists of two stages. In stage 1, sensitivity for severe fatty liver and sensitivity for cirrhotic liver are computed from

the confusion matrix obtained for a subset (out of 30 subsets) which resulted in highest OCA. In stage 2, classification average accuracy (standard deviation) of the 30 subsets is computed.

Table 6.1: CAC system results without feature selection with SVM classifier (Expt. 1)

Features	Confusion Matrix			Sen.$_{Sev.Fat}$ (%)	Sen.$_{Cir}$ (%)	OCA (%)
		Sev. Fat	**Cir**			
Allftrs	**Sev. Fat**	26	6	86.6	80	83.3
	Cir	4	24			
FOS	**Sev. Fat**	30	1	100	96.6	**98.3**
	Cir	0	29			
Grad	**Sev. Fat**	29	3	96.6	90	**93.3**
	Cir	1	27			
MI	**Sev. Fat**	11	1	36.6	**96.6**	66.6
	Cir	19	29			
RLM	**Sev. Fat**	21	11	70	63.3	66.6
	Cir	9	19			
GLCM	**Sev. Fat**	19	9	63.3	70	66.6
	Cir	11	21			
Laws	**Sev. Fat**	29	4	96.6	86.6	**91.6**
	Cir	1	26			
FOS+Grad+ Laws	**Sev. Fat**	28	1	93.3	96.6	95
	Cir	2	29			
FOS+Grad	**Sev. Fat**	30	3	100	90	95
	Cir	0	27			
FOS+Laws	**Sev. Fat**	29	3	96.6	90	93.3
	Cir	1	27			
Grad+Laws	**Sev. Fat**	29	4	96.6	86.6	91.6
	Cir	1	26			

Note: **Sev. Fat**: Severe fatty liver; **Cir**: Cirrhotic liver; **Sen.$_{Sev.Fat}$**: Sensitivity of severe fatty liver; **Sen.$_{Cir}$**: Sensitivity of cirrhotic liver; **OCA**: overall classification accuracy.

In stage 1 of experiment 2, the classification results are computed for a subset (out of 30 subsets) which resulted in highest OCA. The classification results for subsets obtained using KNN-DEFS and NB-DEFS are tabulated in Table 6.2 and Table 6.3, respectively. Overall, the OCAs of all the feature sets have increased after feature selection. From Table 6.2 and 6.3, it can be observed that the subsets of RLM features set from KNN-DEFS and NB-DEFS have yielded an OCA of 78.3 %, and 75 %, respectively. Similarly, the subsets of Laws features set from KNN-DEFS and NB-DEFS yield an OCA of 100 % and 98.3 %. The concatenated features sets such as Allftrs, FOS + Grad + Laws and FOS + Laws have shown an OCA of 100 % in both feature selection methods. Hence, to strengthen the validation of results, stage 2 has been carried out.

Table 6.2: Best classification results after feature selection using KNN-DEFS with SVM classifier (Expt. 2, Stage 1)

Features	Confusion Matrix			$Sen._{Sev.Fat}$ (%)	$Sen._{Cir}$ (%)	OCA (%)
		Sev. Fat	**Cir**			
Allftrs	**Sev. Fat**	30	0	100	100	100
	Cir	0	30			
RLM	**Sev. Fat**	27	10	90	66.6	**78.3**
	Cir	3	20			
GLCM	**Sev. Fat**	24	6	80	80	80
	Cir	6	24			
Laws	**Sev. Fat**	30	0	100	100	**100**
	Cir	0	30			
FOS+Grad+ Laws	**Sev. Fat**	30	0	100	100	100
	Cir	0	30			
FOS+Grad	**Sev. Fat**	30	2	100	93.3	96.6
	Cir	0	28			
FOS+Laws	**Sev. Fat**	30	0	100	100	100
	Cir	0	30			
Grad+Laws	**Sev. Fat**	30	0	100	100	100
	Cir	0	30			

Note: **Sev. Fat**: Severe fatty liver; **Cir**: Cirrhotic liver; **$Sen._{Sev.Fat}$**: Sensitivity of severe fatty liver; **$Sen._{Cir}$**: Sensitivity of cirrhotic liver; **OCA**: Overall classification accuracy.

In stage 2 of experiment 2, for each features set, classification average accuracy (standard deviation) are estimated from 30 subsets obtained. The results of stage 2 are tabulated in Table 6.4. The subsets of RLM features yielded an average accuracy (standard deviation) value of 70.6 (2.8) and 68.4(3.9) from KNN-DEFS and NB-DEFS, respectively. The subset of FOS + Grad + Laws features set from KNN-DEFS showed better performance by yielding an average accuracy (standard deviation) of 99.2(1.0) in comparison with 97.5(1.2) as yielded by NB-DEFS method. The subsets of FOS + Laws feature set obtained by KNN-DEFS method gave the best performance with average accuracy (standard deviation) value of 99.5(0.8).

6.4 Additional observations from the present work

The results of the exhaustive experimentations carried out in the present work indicates that, amongst the individual feature sets, FOS features set consisting of only ten features outperformed with an OCA value of 98.3 % without feature selection. This is possibly because of increase in intensity of cirrhotic liver images compared to severe fatty liver images. Radiologist opined that, sometimes in obese patients, to have better visualization, the gain parameter in ultrasound machine is increased. This also contributes to the increase in intensity of cirrhotic liver images.

Hence, to rely more on textural characteristics of nodular properties of cirrhotic liver images, FOS + Laws features set is recommended.

Table 6.3: Best classification results after feature selection using NB-DEFS with SVM classifier (Expt. 2, Stage 1)

Features	Confusion Matrix			$Sen._{Sev.Fat}$ (%)	$Sen._{Cir}$ (%)	OCA (%)
		Sev. Fat	**Cir**			
Allftrs	**Sev. Fat**	30	0	100	100	100
	Cir	0	30			
RLM	**Sev. Fat**	23	8	76.6	73.3	**75**
	Cir	7	22			
GLCM	**Sev. Fat**	26	8	86.6	73.3	80
	Cir	4	22			
Laws	**Sev. Fat**	30	1	100	96.6	**98.3**
	Cir	0	29			
FOS+Grad+ Laws	**Sev. Fat**	30	0	100	100	100
	Cir	0	30			
FOS+Grad	**Sev. Fat**	30	2	100	93.3	96.6
	Cir	0	28			
FOS+Laws	**Sev. Fat**	30	0	100	100	100
	Cir	0	30			
Grad+Laws	**Sev. Fat**	30	1	100	96.6	98.3
	Cir	0	29			

Note: **Sev. Fat**: Severe fatty liver; **Cir**: Cirrhotic liver; **$Sen._{Sev.Fat}$**: Sensitivity of severe fatty liver; **$Sen._{cir}$**: Sensitivity of cirrhotic liver; **OCA**: Overall classification accuracy.

Table 6.4: CAC system results: average accuracy (standard deviation) after feature selection with SVM classifier (Expt. 2, Stage 2)

Features	KNN-DEFS (AASD)	NB-DEFS (AASD)
Allftrs	97.4 (1.4)	97.7(1.5)
RLM	70.6(2.8)	68.4(3.9)
GLCM	76.4(2.2)	76.3(2.1)
Laws	98.0(1.8)	97.2(0.9)
FOS+Grad+Laws	99.2 (1.0)	97.5(1.2)
FOS+Grad	96.6	96.3(0.5)
FOS+Laws	**99.5(0.8)**	97.9(1.1)
Grad+Laws	97.1(1.6)	98.0(0.5)

Note: **AASD**: Average Accuracy (in %) (Standard Deviation)

From computations of average accuracy (standard deviation) and the OCA values obtained for 30 subsets during feature selection, it is observed that the FOS + Laws features set gave higher average accuracy and less standard deviation (highlighted with bold numbers in Table 6.4) and thus can be considered as optimal for characterization of severe fatty and cirrhotic liver tissue.

During feature selection process, feature subsets are obtained by two wrapper methods i.e., KNN-DEFS and NB-DEFS. In classification stage, SVM classifier is used in both cases. From the results reported in Table 6.4, it can be observed that the optimal subsets yielded by KNN-

DEFS based wrapper method of feature selection yield better classification accuracy in comparison with the optimal subsets yielded by NB-DEFS based wrapper method of feature selection. Thus it can be concluded that selection of a suitable classifier in wrapper based feature selection algorithms can enhance the performance of the CAC system design.

6.5 Concluding Remarks

The aim of the present work is to enhance the potential of conventional gray scale B-mode ultrasound imaging modality for differential diagnosis between severe fatty liver and cirrhotic liver. Accordingly, medical domain knowledge has been utilized in considering the ROI from the liver parenchyma for the developing the proposed CAC system for characterization of severe fatty and cirrhotic liver tissue. The optimal subsets of FOS + Laws features set yielded by KNN-DEFS wrapper based feature selection algorithm outperformed with an average accuracy (standard deviation) value of 99.5(0.8).

From the exhaustive experiments carried out in the present work, it can be concluded that selection of a suitable classifier in wrapper based feature selection algorithms can enhance the performance of the CAC system design. The study also highlights the significance of concatenation of FOS + Laws features to capture the nodular properties of cirrhotic liver parenchyma yielding better texture discrimination between severe fatty liver and cirrhotic liver disease.

The promising result obtained in the present work, indicate the usefulness of the proposed CAC system for characterization of severe fatty liver and cirrhotic liver images during routine clinical practice by the radiologists.

Chapter 7

Conclusions

The present work proposed four CAC systems, through which the set objectives have been achieved. In this chapter, the description of each objective being achieved are presented in brief. The two databases of kidney and liver B-mode ultrasound images are considered for classification using same methodologies. An overall perspective from the results of these databases are included. The limitations and future possibilities of the present work are also been outlined.

7.1 Concluding Remarks

Objective 1: The significance of considering appropriate ROIs for the classification of B-mode ultrasound images

In case of kidney image classes considered, the distinguishing characteristics among normal and MRD cases are prominent in the region of renal parenchyma. In cysts, the characteristic region is localized to small area. Hence, ROIs are considered corresponding to these regions and the system yielded promising result, an OCA of 89.5 % for Grad+RLM features without feature selection (refer chapter 3).

In case of normal and fatty liver images, the dominant distinguishing features are present in diaphragm region. Hence, inclusion of features from DROIs showed tremendous improvement in the results. For example, OCA of 80 % for Laws ratio features without feature selection (refer chapter 5).

Objective 2: The potentiality of features from de-speckled images for the classification of B-mode ultrasound images

The algorithms used for de-speckling of an ultrasound image bring changes in visual characteristics of an image. Hence, in the present work, features extracted from the de-speckled images are used for classification. From the results presented in chapter 3, it is found that the features from the de-speckled images have the potential to enhance the performance of a CAC system. It is also observed that, by concatenating features from original images and de-speckled images followed by feature selection would further enhance the performance of a CAC system. For example, an OCA of 79 % and 82.5 % for Laws and RLM features without feature selection increased to an OCA of 90.6% and 88.3 % respectively after feature selection. The results further

increased to an OCA of 94.1 % and 90.6% for set 3 (features from original images and images de-speckled by enhanced Lee method concatenated) after feature selection.

Objective 3: Evaluating the performance of texture features w.r.t. de-speckling methods for the classification of B-mode ultrasound images.

From the results of chapter 3, it has been observed that, each feature category's classification performance is different when the features are extracted from images de-speckled by various methods. Hence, the work has been extended with only two classes of kidney (normal and MRD) in chapter 4 to explore the right combination of feature category and de-speckling method, which would result in best performance. For example, after feature selection, RLM features obtained an OCA of 87.2 % (features from original images) has increased to an OCA of 89 % (features from images de-speckled by Lee1/enLee method) and 92.7 % (features from images des-speckled by Frost method). It is concluded that, an appropriate combination of feature category and de-speckling method would contribute greatly in improving the accuracy of the CAC system.

Objective 4: A way to enhance the performance of classification of fatty liver images

To distinguish grades of fatty liver from normal liver images, radiologists consider diaphragm visibility along with the texture of liver parenchyma. Hence, in the work presented in chapter 5, ROIs from these regions are considered and combined to represent the characteristics of a particular image. ROIs are combined in three ways forming ratio features, inverse ratio features and additive features. Ratio features performed better in the current work. For example, Laws features obtained an OCA of 80 %, 70.8 % and 56.6 % in case of ratio features, inverse ratio features and additive features respectively.

Objective 5: Optimal texture features for the classification of B-mode ultrasound images

Six texture feature categories such as first order statistics, gradient, moment invariant, GLCM, RLM and Laws features are considered. Gradient based features which are five in number have been hardly used in literature. But, in all the CAC systems gradient features performance has been better. In the present work, each feature category's classification performances have been estimated. Features with good performance have been considered in forming concatenated feature sets. Further, to reduce the number of features by excluding irrelevant or redundant features has been carried out using a feature selection process.

Objective 6: A way to improve the potential of feature selection process

In the present work, DEFS algorithm has been used for feature selection. DEFS is a wrapper method, i.e, it involves a classifier within the feature selection process. In the work presented in chapter 6, two classifiers namely, KNN and NB are considered. For KNN-DEFS and NB-DEFS, separate feature subsets are obtained and used for classification. The features subsets from KNN-DEFS performed better. For example, an OCA of 98.3 % for Laws features subsets from NB-DEFS is obtained, whereas for the subsets from KNN-DEFS, OCA of Laws features is 100 %. Thereby, it is concluded that the classifier in wrapper method of feature selection has an impact on the performance of CAC system.

Apart from the objectives, the concluding remark from the present work is that, the methodologies used at various stages of CAC system are same for both kidney and liver database. The ROI size of 32×32 pixels is used in extracting necessary texture information. To have an overview of performance of the texture feature categories in all the CAC systems, few comparative results are tabulated in Table 7.1.

Table 7.1: OCAs of four CAC systems without feature selection

Texture features	Kidney Images (part 1)		Liver Images (part 2)	
	CAC system 1	CAC system 2	CAC system 3	CAC system 4
FOS	77.9	67.2	**79.1**	**98.3**
Grad	**86**	**78.1**	65	**93.3**
MI	70.9	63.6	68.3	66.6
RLM	**82.5**	**81.8**	51.6	66.6
GLCM	79	76.3	60	66.6
Laws	79	72.7	**80**	**91.6**

Note: OCA – Overall classification accuracy (in %)

In Table 7.1, for comparison purpose, the OCAs for six categories of texture features extracted from original images, without feature selection are tabulated. The results under the columns CAC system 1 and CAC system 2 are of features extracted from the original images. CAC system 3 results are of ratio features set of LROI and DROI feature values from original images. CAC system 4 column represents OCAs of features from original images.

FOS features showed 79.1 % OCA in CAC system 3, whereas 98.3 % OCA for CAC system 4 which can be credited to increased intensity in cirrhosis. Grad features (5 features) showed promising performance with 86 %, 78.1 % and 93.3 % OCAs for CAC system 1, CAC system 2 and CAC system 4 respectively. MI features have consistently not performed well in any of the CAC systems. RLM features have a clear indication of good performance for kidney images with 82.5 % and 81.8 % OCAs in case of CAC system 1 and CAC system 2 respectively. To some

extent, the degraded performance of GLCM features may be credited to large number of features (420 features) involved without feature selection. Laws features have low performance in case of CAC system 2, otherwise it yielded good results with 79 %, 80 % and 91.6 % OCAs for CAC system 1, CAC system 3 and CAC system 4 respectively.

DEFS and SVM have shown promising performance in feature selection and classification respectively. The parameter values used with DEFS algorithm such as number of features, population size and the number of iterations remained same for all the CAC systems.

With reference to the present workflow depicted in Figure 1.8, in first part, CAC system 1 can be used when three classes of kidney (normal, MRD and cyst) are considered for the classification. The best result obtained is an AASD of 86.3(1.6) for RLM features extracted from ROIs of images de-speckled by Lee's sigma and enhanced Lee methods. If the output is other than cyst for CAC system 1, CAC system 2 may be used for improving the accuracy of classification between normal and MRD classes. The result observed in the present work is an AASD of 87.0(2.9) for RLM features from the ROIs of images de-speckled by Frost method. There is a little improvement in average accuracy and the standard deviation is increased, but the feature category has changed and number of features utilized is much less.

In second part, CAC system 3 is developed for the classification of normal and grades of fatty liver. The Laws ratio features results have been better with an AASD of 84.9(3.2). If the output of CAC system 3 is a severe fatty liver, it may further led through CAC system 4 for clarification between severe fatty liver and cirrhosis. The results obtained have been an AASD of 99.5(0.8) for the concatenated set of FOS and Laws features subsets from KNN-DEFS. CAC system 3 involved ratio features i.e. features from DROI combined with that of LROI whereas in CAC system 4, Laws features in combination with FOS features have shown much improvement in the average accuracy and standard deviation.

Misclassification Remarks

Misclassification occurs because of existing limitation from radiologist's perspective as well as researcher's perspective. The radiologist's opinion on misclassification results are the non-uniformity in the angle, resolution and imaging device parameter settings considered during image acquisition led the CAC system prediction go wrong in certain cases. The other reason being the demarcation line between classes in terms of texture is overlapping some time. From the observation that, currently used texture feature categories showed varied performances in classification, it can be inferred to have a tailored texture features for the classification of B-

mode ultrasound images. At the same time, the possible limitations of the algorithms used for feature selection and classification cannot be ruled out.

7.2 Limitations

The limitations pertaining to the present work that have been observed are as follows:

The standard benchmark database on ultrasound images is not available for the researchers. Its implications are

i. Researchers have to build their own database which is a time consuming process.

ii. Quantitative comparison of various studies is not possible.

7.3 Future Possibilities

1. The parameter values used for the de-speckling filters are ideal values proposed by respective researchers in their study. Optimization of those values for a particular classification task at hand is an open area of research.

2. In the present work, standard de-speckling methods are used. The authors of OSRAD, claim that the method is suitable as a pre-processing for segmentation. On the similar line, there is a possibility to design de-speckling filters that are tailored for CAC systems.

List of publications from present work

Journal Publications

[1] M. B. Subramanya, V. Kumar, S. Mukherjee, and M. Saini, "SVM-Based CAC System for B-Mode Kidney Ultrasound Images," *Journal of Digital Imaging*, vol. 28, pp. 448-458, 2015/08/01 2015.

[2] M. B. Subramanya, V. Kumar, S. Mukherjee, and M. Saini, "A CAD system for B-mode fatty liver ultrasound images using texture features," *Journal of Medical Engineering & Technology*, vol. 39, pp. 123-130, 2015/02/17 2015.

[3] M. B. Subramanya, V. Kumar, S. Mukherjee, M. Saini and J. Virmani, "A CAD System for Severe Fatty Liver and Cirrhosis using B-Mode Ultrasound Images," *Journal of Medical Imaging and Health Informatics.* [Second revision submitted]

[4] M. B. Subramanya, V. Kumar, S. Mukherjee, and M. Saini, "Performance evaluation of texture features and de-speckling on the classification of B-mode kidney ultrasound images," *Biocybernatics and Biomedical Engineering.* [Under review]

Conference Proceedings

[1] M. B. Subramanya, V. Kumar, S. Mukherjee, and M. Saini, "Classification of normal and medical renal disease using B-mode ultrasound images," in *Computing for Sustainable Global Development (INDIACom), 2015 2nd International Conference on*, pp. 1914-1918, 2015.

References

[1] A. Conci, Á. Sánchez, P. Liatsis, and H. Usuki, "Signal processing techniques for detection of breast diseases," *Signal Processing*, vol. 10, pp. 2783-2784, 2013.

[2] C. S. Anand and J. S. Sahambi, "Wavelet domain non-linear filtering for MRI denoising," *Magnetic Resonance Imaging*, vol. 28, pp. 842-861, 2010.

[3] C. Wikipedia. (2015, Febraury 2015). *Kidney*. Available: https://en.wikipedia.org/wiki/Kidney

[4] H. Lutz and E. Buscarini, "Manual of diagnostic ultrasound," 2011.

[5] K. B. Raja, M. Madheswaran, and K. Thyagarajah, "A hybrid fuzzy-neural system for computer-aided diagnosis of ultrasound kidney images using prominent features," *Journal of medical systems*, vol. 32, pp. 65-83, 2008.

[6] C. M. Rumack, S. R. Wilson, and J. W. Charboneau, *Diagnostic ultrasound vol 1*: London: Mosby, 2005, 2005.

[7] K. B. Raja, M. Madheswaran, and K. Thyagarajah, "Texture pattern analysis of kidney tissues for disorder identification and classification using dominant Gabor wavelet," *Machine Vision and Applications*, vol. 21, pp. 287-300, 2010.

[8] C. Wikipedia. (2014, May 30). *Liver*. Available: http://en.wikipedia.org/wiki/Liver

[9] D. Sabih and M. Hussain, "Automated classification of liver disorders using ultrasound images," *Journal of medical systems*, vol. 36, pp. 3163-3172, 2012.

[10] J. Virmani, V. Kumar, N. Kalra, and N. Khandelwal, "SVM-based characterization of liver ultrasound images using wavelet packet texture descriptors," *Journal of digital imaging*, vol. 26, pp. 530-543, 2013.

[11] C. Wikipedia. (2014, May 30). *Liver disease*. Available: http://en.wikipedia.org/wiki/Liver_disease

[12] W.-C. Yeh, S.-W. Huang, and P.-C. Li, "Liver fibrosis grade classification with B-mode ultrasound," *Ultrasound in medicine & biology*, vol. 29, pp. 1229-1235, 2003.

[13] S. Strauss, E. Gavish, P. Gottlieb, and L. Katsnelson, "Interobserver and intraobserver variability in the sonographic assessment of fatty liver," *American Journal of Roentgenology*, vol. 189, pp. W320-W323, 2007.

[14] J. Virmani, V. Kumar, N. Kalra, and N. Khandelwal, "Prediction of Cirrhosis Based on Singular Value Decomposition of Gray Level Co-occurence Marix and aNneural Network Classifier," in *Developments in E-systems Engineering (DeSE), 2011*, pp. 146-151, 2011.

[15] J. Virmani, V. Kumar, N. Kalra, and N. Khandelwal, "Prediction of cirrhosis from liver ultrasound B-mode images based on Laws' masks analysis," in *Image Information Processing (ICIIP), 2011 International Conference on*, pp. 1-5, 2011.

[16] J. Virmani, V. Kumar, N. Kalra, and N. Khandelwal, "Prediction of liver cirrhosis based on multiresolution texture descriptors from B-mode ultrasound," *International Journal of Convergence Computing*, vol. 1, pp. 19-37, 2013.

[17] J. Virmani, V. Kumar, N. Kalra, and N. Khadelwal, "A rapid approach for prediction of liver cirrhosis based on first order statistics," in *Multimedia, Signal Processing and Communication Technologies (IMPACT), 2011 International Conference on*, pp. 212-215, 2011.

[18] J. Virmani, V. Kumar, N. Kalra, and N. Khandelwal, "SVM-based characterisation of liver cirrhosis by singular value decomposition of GLCM matrix," *International Journal of Artificial Intelligence and Soft Computing*, vol. 3, pp. 276-296, 2013.

[19] P. Deuflhard, O. Dössel, A. K. Louis, and S. Zachow, "More Mathematics into Medicine!," in *Production Factor Mathematics*, ed: Springer, pp. 357-378, 2010.

[20] O. Dössel, D. Farina, M. Mohr, M. Reumann, G. Seemann, and D. L. Weiss, "Modelling and imaging electrophysiology and contraction of the heart," in *Advances in Medical Engineering*, ed: Springer, pp. 3-16, 2007.

[21] S. Nirmala, S. Dandapat, and P. Bora, "Performance evaluation of distortion measures for retinal images," *International Journal of Computer Applications*, vol. 17, 2011.

[22] S. Nirmala, S. Dandapat, and P. Bora, "Wavelet weighted blood vessel distortion measure for retinal images," *Biomedical Signal Processing and Control*, vol. 5, pp. 282-291, 2010.

[23] S. K. Pahuja, S. Anand, and A. Sengupta, "Electrical impedance tomography based image reconstruction and feto-maternal monitoring in pregnancy," *Health*, vol. 3, p. 482, 2011.

[24] G. Reinerth, M. Reumann, G. Seemann, N. Kayhan, J. Albers, O. Doessel, *et al.*, "Three-dimensional electrophysiological and morphological computer models for individualisation of antiarrhythmic cardiac surgery," in *International Congress Series*, pp. 813-818, 2004.

[25] A. Srivastava, J. P. Woodcock, R. E. Mansel, D. J. Webster, P. Laidler, L. E. Hughes, *et al.*, "Doppler ultrasound flowmetry predicts 15 year outcome in patients with skin melanoma," *Indian Journal of Surgery*, vol. 74, pp. 278-283, 2012.

[26] T. Voigt, U. Katscher, and O. Doessel, "Quantitative conductivity and permittivity imaging of the human brain using electric properties tomography," *Magnetic Resonance in Medicine*, vol. 66, pp. 456-466, 2011.

[27] M. B. Subramanya, V. Kumar, S. Mukherjee, and M. Saini, "A CAD system for B-mode fatty liver ultrasound images using texture features," *Journal of Medical Engineering & Technology,* vol. 39, pp. 123-130, 2015/02/17 2015.

[28] M. B. Subramanya, V. Kumar, S. Mukherjee, and M. Saini, "Classification of normal and medical renal disease using B-mode ultrasound images," in *Computing for Sustainable Global Development (INDIACom), 2015 2nd International Conference on*, pp. 1914-1918, 2015.

[29] J. Virmani, V. Kumar, N. Kalra, and N. Khandelwal, "Neural network ensemble based CAD system for focal liver lesions from B-mode ultrasound," *Journal of digital imaging,* vol. 27, pp. 520-537, 2014.

[30] J. Virmani, V. Kumar, N. Kalra, and N. Khandelwa, "PCA-SVM based CAD System for Focal liver lesions using B-mode ultrasound Images," *Defence Science Journal,* vol. 63, pp. 478-486, 2013.

[31] H. Alto, R. M. Rangayyan, R. B. Paranjape, J. L. Desautels, and H. Bryant, "An indexed atlas of digital mammograms for computer-aided diagnosis of breast cancer," in *Annales des télécommunications*, pp. 820-835, 2003.

[32] T. C. André and R. M. Rangayyan, "Classification of breast masses in mammograms using neural networks with shape, edge sharpness, and texture features," *Journal of Electronic Imaging,* vol. 15, pp. 013019-013019-10, 2006.

[33] T. Chaira and S. Anand, "A Novel Intuitionistic Fuzzy Approach for Tumor/Hemorrhage Detection in Medical Images," *Journal of Scientific and Industrial Research,* vol. 70, pp. 427-434, 2011.

[34] M. M. R. Krishnan, P. Shah, A. Choudhary, C. Chakraborty, R. R. Paul, and A. K. Ray, "Textural characterization of histopathological images for oral sub-mucous fibrosis detection," *Tissue and Cell,* vol. 43, pp. 318-330, 2011.

[35] M. M. R. Krishnan, C. Chakraborty, R. R. Paul, and A. K. Ray, "Hybrid segmentation, characterization and classification of basal cell nuclei from histopathological images of normal oral mucosa and oral submucous fibrosis," *Expert Systems with Applications,* vol. 39, pp. 1062-1077, 2012.

[36] M. M. R. Krishnan, P. Shah, C. Chakraborty, and A. K. Ray, "Statistical analysis of textural features for improved classification of oral histopathological images," *Journal of medical systems,* vol. 36, pp. 865-881, 2012.

[37] N. Padhye, A. Brazdeikis, and M. Verklan, "Monitoring fetal development with magnetocardiography," in *Engineering in Medicine and Biology Society, 2004. IEMBS'04. 26th Annual International Conference of the IEEE*, pp. 3609-3610, 2004.

[38] J. J. R. Raj and S. Anand, "Efficient analysis and evaluation of elasticity of breast tumours using ultrasound in Indian women," *International Journal of Biomedical Engineering and Technology*, vol. 18, pp. 227-239, 2015.

[39] Y. Wang and P. Liatsis, "Automatic segmentation of coronary arteries in CT imaging in the presence of kissing vessel artifacts," *Information Technology in Biomedicine, IEEE Transactions on*, vol. 16, pp. 782-788, 2012.

[40] I. A. Wright, N. A. Gough, F. Rakebrandt, M. Wahab, and J. P. Woodcock, "Neural network analysis of Doppler ultrasound blood flow signals: A pilot study," *Ultrasound in medicine & biology*, vol. 23, pp. 683-690, 1997.

[41] A. K. Jain, *Fundamentals of digital image processing*: Prentice-Hall, Inc., 1989.

[42] R. C. Gonzalez, *Digital image processing*: Pearson Education India, 2009.

[43] K. B. Raja, M. Madheswaran, and K. Thyagarajah, "A general segmentation scheme for contouring kidney region in ultrasound kidney images using improved higher order spline interpolation," *J Biol Med Sci*, vol. 2, pp. 81-88, 2007.

[44] K. B. Raja, M. Madheswaran, and K. Thyagarajah, "Ultrasound kidney image analysis for computerized disorder identification and classification using content descriptive power spectral features," *Journal of medical systems*, vol. 31, pp. 307-317, 2007.

[45] K. B. Raja, M. Madheswaran, and K. Thyagarajah, "Quantitative and qualitative evaluation of US kidney images for disorder classification using multi-scale differential features," *ICGST-BIME Journal*, vol. 7, pp. 1-8, 2007.

[46] K. B. Raja, M. Madheswaran, and K. Thyagarajah, "Analysis of ultrasound kidney images using content descriptive multiple features for disorder identification and ANN based classification," in *Computing: Theory and Applications, 2007. ICCTA'07. International Conference on*, pp. 382-388, 2007.

[47] A. Lopes, R. Touzi, and E. Nezry, "Adaptive speckle filters and scene heterogeneity," *Geoscience and Remote Sensing, IEEE Transactions on*, vol. 28, pp. 992-1000, 1990.

[48] Y. Chen, R. Yin, P. Flynn, and S. Broschat, "Aggressive region growing for speckle reduction in ultrasound images," *Pattern Recognition Letters*, vol. 24, pp. 677-691, 2003.

[49] T. R. Crimmins, "Geometric filter for speckle reduction," *Applied optics*, vol. 24, pp. 1438-1443, 1985.

[50] S. Aja-Fernández and C. Alberola-López, "On the estimation of the coefficient of variation for anisotropic diffusion speckle filtering," *Image Processing, IEEE Transactions on,* vol. 15, pp. 2694-2701, 2006.

[51] Y. Yu and S. T. Acton, "Speckle reducing anisotropic diffusion," *Image Processing, IEEE Transactions on,* vol. 11, pp. 1260-1270, 2002.

[52] S. Finn, M. Glavin, and E. Jones, "Echocardiographic speckle reduction comparison," *Ultrasonics, Ferroelectrics, and Frequency Control, IEEE Transactions on,* vol. 58, pp. 82-101, 2011.

[53] K. Krissian, C.-F. Westin, R. Kikinis, and K. G. Vosburgh, "Oriented speckle reducing anisotropic diffusion," *Image Processing, IEEE Transactions on,* vol. 16, pp. 1412-1424, 2007.

[54] D. Mittal, V. Kumar, S. C. Saxena, N. Khandelwal, and N. Kalra, "Enhancement of the ultrasound images by modified anisotropic diffusion method," *Medical & biological engineering & computing,* vol. 48, pp. 1281-1291, 2010.

[55] I. Akiyama, T. Saito, M. Nakamura, N. Taniguchi, and K. Itoh, "Tissue characterization by using fractal dimension of B-scan image," in *Ultrasonics Symposium, 1990. Proceedings., IEEE 1990*, pp. 1353-1355, 1990.

[56] Y. M. Kadah, A. Farag, J. M. Zurada, A. M. Badawi, and A.-B. M. Youssef, "Classification algorithms for quantitative tissue characterization of diffuse liver disease from ultrasound images," *Medical Imaging, IEEE Transactions on,* vol. 15, pp. 466-478, 1996.

[57] J.-W. Jeong, S. Lee, L. J. Won, D.-S. Yoo, and S. Kim, "Computer-assisted Sonographic Analysis of the Hepatorenal and Textural Features for the Diagnosis of the Fatty Liver," in *Conference proceedings:... Annual International Conference of the IEEE Engineering in Medicine and Biology Society. IEEE Engineering in Medicine and Biology Society. Conference*, pp. 3348-3350, 2004.

[58] G. Li, Y. Luo, W. Deng, X. Xu, A. Liu, and E. Song, "Computer aided diagnosis of fatty liver ultrasonic images based on support vector machine," in *Engineering in Medicine and Biology Society, 2008. EMBS 2008. 30th Annual International Conference of the IEEE*, pp. 4768-4771, 2008.

[59] R. Ribeiro and J. Sanches, "Fatty liver characterization and classification by ultrasound," in *Pattern Recognition and Image Analysis*, ed: Springer, pp. 354-361, 2009.

[60] S. İçer, A. Coşkun, and T. İkizceli, "Quantitative grading using grey relational analysis on ultrasonographic images of a fatty liver," *Journal of medical systems,* vol. 36, pp. 2521-2528, 2012.

[61] Y. Chitre, A. P. Dhawan, and M. Moskowitz, "Artificial neural network based classification of mammographic microcalcifications using image structure features," *International Journal of Pattern Recognition and Artificial Intelligence,* vol. 7, pp. 1377-1401, 1993.

[62] A. Gupta, "Statistical Characterisation of Speckle in Clinical Echocardiographic Images with Pearson Family of Distributions," *Defence Science Journal,* vol. 61, pp. 473-478, 2011.

[63] R. Nandi, A. K. Nandi, R. M. Rangayyan, and D. Scutt, "Classification of breast masses in mammograms using genetic programming and feature selection," *Medical and biological engineering and computing,* vol. 44, pp. 683-694, 2006.

[64] R. N. Khushaba, A. Al-Ani, and A. Al-Jumaily, "Feature subset selection using differential evolution and a statistical repair mechanism," *Expert Systems with Applications,* vol. 38, pp. 11515-11526, 2011.

[65] A. M. Badawi, A. S. Derbala, and A.-B. M. Youssef, "Fuzzy logic algorithm for quantitative tissue characterization of diffuse liver diseases from ultrasound images," *International Journal of Medical Informatics,* vol. 55, pp. 135-147, 1999.

[66] K. Fukunaga, *Introduction to statistical pattern recognition*: Academic press, 2013.

[67] M. Singh, S. Singh, and S. Gupta, "A new measure of echogenicity of ultrasound images for liver classification," in *Electrical and Computer Engineering (CCECE), 2011 24th Canadian Conference on*, pp. 000317-000320, 2011.

[68] R. M. Rangayyan, T. M. Nguyen, F. J. Ayres, and A. K. Nandi, "Effect of pixel resolution on texture features of breast masses in mammograms," *Journal of digital imaging,* vol. 23, pp. 547-553, 2010.

[69] R. Agrawal, "Perturbation scheme for online learning of features: Incremental principal component analysis," *Pattern Recognition,* vol. 41, pp. 1452-1460, 2008.

[70] H. Guo, Q. Zhang, and A. K. Nandi, "Feature extraction and dimensionality reduction by genetic programming based on the Fisher criterion," *Expert Systems,* vol. 25, pp. 444-459, 2008.

[71] S. H. Kim, J. M. Lee, K. G. Kim, J. H. Kim, J. Y. Lee, J. K. Han, *et al.*, "Computer-aided image analysis of focal hepatic lesions in ultrasonography: preliminary results," *Abdominal imaging,* vol. 34, pp. 183-191, 2009.

[72] N. R. Mudigonda, R. M. Rangayyan, and J. L. Desautels, "Gradient and texture analysis for the classification of mammographic masses," *Medical Imaging, IEEE Transactions on*, vol. 19, pp. 1032-1043, 2000.

[73] R. Agrawal, "Study of ultrasonic echo envelope based on Nakagami-inverse Gaussian distribution," *Ultrasound in medicine & biology*, vol. 32, pp. 371-376, 2006.

[74] R. Agrawal, "Ultrasonic backscattering in tissue: characterization through Nakagami-generalized inverse Gaussian distribution," *Computers in biology and medicine*, vol. 37, pp. 166-172, 2007.

[75] F. Rakebrandt, D. Crawford, D. Havard, D. Coleman, and J. Woodcock, "Relationship between ultrasound texture classification images and histology of atherosclerotic plaque," *Ultrasound in medicine & biology*, vol. 26, pp. 1393-1402, 2000.

[76] S. Golemati, T. J. Tegos, A. Sassano, K. S. Nikita, and A. N. Nicolaides, "Echogenicity of B-mode sonographic images of the carotid artery work in progress," *Journal of ultrasound in medicine*, vol. 23, pp. 659-669, 2004.

[77] S. S. Sonnad, "Describing Data: Statistical and Graphical Methods 1," *Radiology*, vol. 225, pp. 622-628, 2002.

[78] P. M. Szczypiński, M. Strzelecki, A. Materka, and A. Klepaczko, "MaZda—A software package for image texture analysis," *Computer methods and programs in biomedicine*, vol. 94, pp. 66-76, 2009.

[79] C. Wikipedia. (2013, September 28). *Percentile*. Available: http://en.wikipedia.org/wiki/Percentile

[80] A. Materka and P. Szypinski, "MaZda User's Manual MaZda 4.6. download link; 1999–2006," ed, 2009.

[81] S. A. Dudani, K. J. Breeding, and R. B. McGhee, "Aircraft identification by moment invariants," *Computers, IEEE Transactions on*, vol. 100, pp. 39-46, 1977.

[82] K. B. Raja, M. Madheswaran, and K. Thyagarajah, "Evaluation of tissue characteristics of kidney for diagnosis and classification using first order statistics and RTS invariants," in *Signal Processing, Communications and Networking, 2007. ICSCN'07. International Conference on*, pp. 483-487, 2007.

[83] M. Tuceryan, "Moment-based texture segmentation," *Pattern Recognition Letters*, vol. 15, pp. 659-668, 1994.

[84] M.-K. Hu, "Visual pattern recognition by moment invariants," *Information Theory, IRE Transactions on*, vol. 8, pp. 179-187, 1962.

[85] R. M. Haralick, "Statistical and structural approaches to texture," *Proceedings of the IEEE,* vol. 67, pp. 786-804, 1979.

[86] D. A. Clausi, "An analysis of co-occurrence texture statistics as a function of grey level quantization," *Canadian Journal of remote sensing,* vol. 28, pp. 45-62, 2002.

[87] R. M. Haralick, K. Shanmugam, and I. H. Dinstein, "Textural features for image classification," *Systems, Man and Cybernetics, IEEE Transactions on,* pp. 610-621, 1973.

[88] L.-K. Soh and C. Tsatsoulis, "Texture analysis of SAR sea ice imagery using gray level co-occurrence matrices," *Geoscience and Remote Sensing, IEEE Transactions on,* vol. 37, pp. 780-795, 1999.

[89] A. P. Dhawan, "Analysis of mammographic microcalcifications using gray-level image structure features," *Medical Imaging, IEEE Transactions on,* vol. 15, pp. 246-259, 1996.

[90] M. M. Galloway, "Texture analysis using gray level run lengths," *Computer graphics and image processing,* vol. 4, pp. 172-179, 1975.

[91] D. Mittal, V. Kumar, S. C. Saxena, N. Khandelwal, and N. Kalra, "Neural network based focal liver lesion diagnosis using ultrasound images," *Computerized Medical Imaging and Graphics,* vol. 35, pp. 315-323, 2011.

[92] K. I. Laws, "Rapid texture identification," in *24th annual technical symposium*, pp. 376-381, 1980.

[93] A. K. Jain, R. P. Duin, and J. Mao, "Statistical pattern recognition: A review," *Pattern Analysis and Machine Intelligence, IEEE Transactions on,* vol. 22, pp. 4-37, 2000.

[94] M. S. Khadtare and J. Sahambi, "ECG arrhythmia analysis by multicategory support vector machine," in *Applied Computing*, ed: Springer, pp. 100-107, 2004.

[95] L. Bottou, C. Cortes, J. S. Denker, H. Drucker, I. Guyon, L. D. Jackel, *et al.*, "Comparison of classifier methods: a case study in handwritten digit recognition," in *International Conference on Pattern Recognition*, pp. 77-77, 1994.

[96] J. Friedman, "Another approach to polychotomous classifcation," *Dept. Statist., Stanford Univ., Stanford, CA, USA, Tech. Rep,* 1996.

[97] N. Garcia-Pedrajas and D. Ortiz-Boyer, "Improving multiclass pattern recognition by the combination of two strategies," *Pattern Analysis and Machine Intelligence, IEEE Transactions on,* vol. 28, pp. 1001-1006, 2006.

[98] J. C. Platt, N. Cristianini, and J. Shawe-Taylor, "Large Margin DAGs for Multiclass Classification," in *nips*, pp. 547-553, 1999.

[99] J. Chen, C. Wang, and R. Wang, "Combining support vector machines with a pairwise decision tree," *Geoscience and Remote Sensing Letters, IEEE,* vol. 5, pp. 409-413, 2008.

[100] B. Fei and J. Liu, "Binary tree of SVM: a new fast multiclass training and classification algorithm," *Neural Networks, IEEE Transactions on,* vol. 17, pp. 696-704, 2006.

[101] E. L. Allwein, R. E. Schapire, and Y. Singer, "Reducing multiclass to binary: A unifying approach for margin classifiers," *The Journal of Machine Learning Research,* vol. 1, pp. 113-141, 2001.

[102] T. G. Dietterich and G. Bakiri, "Solving multiclass learning problems via error-correcting output codes," *Journal of artificial intelligence research,* pp. 263-286, 1995.

[103] O. Pujol, P. Radeva, and J. Vitria, "Discriminant ecoc: A heuristic method for application dependent design of error correcting output codes," *Pattern Analysis and Machine Intelligence, IEEE Transactions on,* vol. 28, pp. 1007-1012, 2006.

[104] J. Chen, C. Wang, and R. Wang, "Using stacked generalization to combine SVMs in magnitude and shape feature spaces for classification of hyperspectral data," *Geoscience and Remote Sensing, IEEE Transactions on,* vol. 47, pp. 2193-2205, 2009.

[105] C.-W. Hsu and C.-J. Lin, "A comparison of methods for multiclass support vector machines," *Neural Networks, IEEE Transactions on,* vol. 13, pp. 415-425, 2002.

[106] T. Gandhi, B. K. Panigrahi, and S. Anand, "A comparative study of wavelet families for EEG signal classification," *Neurocomputing,* vol. 74, pp. 3051-3057, 2011.

[107] J. Virmani, V. Kumar, N. Kalra, and N. Khandelwal, "Characterization of primary and secondary malignant liver lesions from B-mode ultrasound," *Journal of digital imaging,* vol. 26, pp. 1058-1070, 2013.

[108] C.-C. Lee and S.-H. Chen, "Gabor Wavelets and SVM Classifier for Liver Diseases Classiflcation from CT Images," in *Systems, Man and Cybernetics, 2006. SMC'06. IEEE International Conference on*, pp. 548-552, 2006.

[109] J. Wan and S. Zhou, "Features extraction based on wavelet packet transform for B-mode ultrasound liver images," in *Image and Signal Processing (CISP), 2010 3rd International Congress on*, pp. 949-955, 2010.

[110] S. Nawaz and A. H. Dar, "Hepatic lesions classification by ensemble of SVMs using statistical features based on co-occurrence matrix," in *Emerging Technologies, 2008. ICET 2008. 4th International Conference on*, pp. 21-26, 2008.

[111] Y. L. Huang, D. R. Chen, Y. R. Jiang, S. J. Kuo, H. K. Wu, and W. Moon, "Computer-aided diagnosis using morphological features for classifying breast lesions on ultrasound," *Ultrasound in Obstetrics & Gynecology,* vol. 32, pp. 565-572, 2008.

[112] F. Moayedi, Z. Azimifar, R. Boostani, and S. Katebi, "Contourlet-based mammography mass classification," in *Image Analysis and Recognition*, ed: Springer, 2007, pp. 923-934.

[113] Y.-L. Huang, K.-L. Wang, and D.-R. Chen, "Diagnosis of breast tumors with ultrasonic texture analysis using support vector machines," *Neural Computing & Applications*, vol. 15, pp. 164-169, 2006.

[114] T. K. Reddy and N. Kumaravel, "A comparison of wavelet, curvelet and contourlet based texture classification algorithms for characterization of bone quality in dental CT," in *Proceedings of International Conference on Environmental, Biomedical and Biotechnology, IPCBEE*, pp. 60-65, 2011.

[115] N. Tsiaparas, S. Golemati, I. Andreadis, J. Stoitsis, and K. S. Nikita, "Multiscale geometric texture analysis of ultrasound images of carotid atherosclerosis," in *Information Technology and Applications in Biomedicine (ITAB), 2010 10th IEEE International Conference on*, pp. 1-4, 2010.

[116] Q. D. Tran and P. Liatsis, "Improving Fusion with One-Class Classification and Boosting in Multimodal Biometric Authentication," in *Intelligent Computing in Bioinformatics*, ed: Springer, pp. 438-444, 2014.

[117] A. Ben-Hur and J. Weston, "A user's guide to support vector machines," in *Data mining techniques for the life sciences*, ed: Springer, pp. 223-239, 2010.

[118] C. J. Burges, "A tutorial on support vector machines for pattern recognition," *Data mining and knowledge discovery*, vol. 2, pp. 121-167, 1998.

[119] M. W. Aslam, Z. Zhu, and A. K. Nandi, "Feature generation using genetic programming with comparative partner selection for diabetes classification," *Expert Systems with Applications*, vol. 40, pp. 5402-5412, 2013.

[120] A. Brazdeikis, A. Guzeldere, N. Padhye, and M. Verklan, "Evaluation of the performance of a QRS detector for extracting the heart interbeat RR time series from fetal magnetocardiography," in *Engineering in Medicine and Biology Society, 2004. IEMBS'04. 26th Annual International Conference of the IEEE*, pp. 369-372, 2004.

[121] R. Mukkavilli, J. Sahambi, and P. Bora, "Modified homomorphic wavelet based despeckling of medical ultrasound images," in *Electrical and Computer Engineering, 2008. CCECE 2008. Canadian Conference on*, pp. 000887-000890, 2008.

[122] A. P. Dhawan and E. Le Royer, "Mammographic feature enhancement by computerized image processing," *Computer Methods and Programs in Biomedicine*, vol. 27, pp. 23-35, 1988.

[123] J.-S. Lee, "Digital image enhancement and noise filtering by use of local statistics," *Pattern Analysis and Machine Intelligence, IEEE Transactions on*, pp. 165-168, 1980.

[124] J.-S. Lee, "Digital image smoothing and the sigma filter," *Computer Vision, Graphics, and Image Processing,* vol. 24, pp. 255-269, 1983.

[125] V. S. Frost, J. A. Stiles, K. S. Shanmugan, and J. C. Holtzman, "A model for radar images and its application to adaptive digital filtering of multiplicative noise," *Pattern Analysis and Machine Intelligence, IEEE Transactions on,* pp. 157-166, 1982.

[126] D. T. Kuan, A. Sawchuk, T. C. Strand, and P. Chavel, "Adaptive restoration of images with speckle," *Acoustics, Speech and Signal Processing, IEEE Transactions on,* vol. 35, pp. 373-383, 1987.

[127] M. B. Subramanya, V. Kumar, S. Mukherjee, and M. Saini, "SVM-Based CAC System for B-Mode Kidney Ultrasound Images," *Journal of Digital Imaging,* vol. 28, pp. 448-458, 2015/08/01 2015.